GEOLOGICAL MAPPING, PETROLOGICAL CHARACTERISATION AND GEOCHEMISTRY OF ROCKS IN THE AUS AREA, SOUTHERN NAMIBIA: IMPLICATIONS FOR POTENTIAL COPPER MINERALIZATION

A MINI THESIS SUBMITTED IN PARTIAL FULFILMENT OF THE REQUIREMENTS FOR THE DEGREE OF MASTER OF SCIENCE IN APPLIED GEOLOGY

GEOLOGY

OF

THE UNIVERSITY OF NAMIBIA

BY

CLAUDIA MUTONGOLUME

200532693

OCTOBER 2020

SUPERVISOR: PROF B.S MAPANI (NAMIBIA UNIVERSITY OF SCIENCE AND TECHNOLOGY, DEPARTMENT OF MINING AND PROCESS ENGINEERING)

Abstract

The study area is located in the southern part of Namibia within the Aus Domain which forms part of the Mesoproterozoic Namaqua Sector of the Namaqua-Natal Metamorphic Province. The sector hosts some significant base metal sulphide deposits that have been mined for the past century. In this study, detailed field mapping, petrography, geochemistry and U-Pb zircon dating were conducted to evaluate the chemical characteristics and tectonic setting of the area with the intent to assess the feasibility and potential of known copper occurrences around Aus area. The Garub Group represents the oldest rocks in the area and comprises marble, calc-silicates, metapelites, garnet biotite quartz gneisses, amphibolites, mafic granulites and serpentinites, which have been intruded by several, variably deformed granites. The Aus, Tsirub and Kubub orthogneisses are the main intrusives in the area. However, field mapping identified a highly fractured and metasomatized K-feldspar plagioclase epidote rock which requires further investigation. Petrographic studies confirm the compositional and deformational variability observed in the field. Geochemistry reveals that all granitoids within the study area are acidic, strongly peraluminous and products of shoshonitic and high-K calc-alkaline magma derived from an A-type source. The A-type granites formed as a result of crustal contamination during the continental extensional phase and have been subjected to compressional deformation. Chondrite-normalised spider diagrams show negative Ta, Nb, P and Ti anomalies, with enrichments in Th and LREE, which suggest that the rocks are derived from an arc environment. Plots of K_2O vs SiO_2 show a considerably greater degree of scatter, which may be attributed to the effects of crustal contamination. Three geotectonic settings are established, i. e. the syn-collisional-Granite (syn-COLG), Volcanic Arc Granites (VAG) and Within Plate Granites (WPG). These inconsistent plots of samples may be attributed to hydrothermal alteration and/or sharing of varying degrees of fractionation within multiple flows, and support a collision of crustal fragments model. Granitoid plutonism for Tsirub augen gneiss and Aus granite gneiss occurred at 1110 ± 7 Ma and 1085 ± 36 Ma respectively. Several granites, which could be responsible for hydrothermal activity, quartz veins, fault structures and occurrence of malachite may bear evidence for copper mineralization in the study area.

Contents

List of Tables

List of Figures

List of Abbreviations

CGS	Council for Geoscience South Africa
CL	Cathodoluminescence
FOV	Field of view
GSN	Geological Survey of Namibia
ICP-MS	Inductively Coupled Plasma Mass Spectrometry
NNMP	Namaqua Natal Metamorphic Province
REE	Rare Earth Element
LREE	Light Rare Earth Element
XPL	Cross polarized light
XRF	X-ray Fluorescence

Acknowledgments

I would like to extend my profound gratitude to my supervisor Prof Ben Mapani for his guidance and support during the course of the project. I would also like to acknowledge Dr Ute Schreiber and Mr Moses Angombe for the valuable comments, remarks and engagement with the thesis. Further, I would like to thank my colleagues at the Geological Survey of Namibia, particularly of the Regional Geoscience Division for their support throughout. I would like to thank Jeremia and Martha Amputu of the Geochemistry Division for helping with the crushing of samples and minerals separation. Equally, I want to extend my gratitude to Simon Jeremia for assistance with the sorting of zircons. Thanks are also due to Dr. Paul Macey for great assistance especially during fieldwork. Martin Harris from the University of Namibia is acknowledged for carrying out age dating analysis in Norway. I am also thankful to the Department of Petroleum Affairs, Ministry of Mines and Energy, for co-funding this study. I do not want to forget my classmates of the 2018/2019 master class for consistent solidarity, fun and the spirit.

Finally, I would like to express my gratitude to my daughter Tangi Ndaifanua and my cousin Ndamononghenda Haukongo for providing me with unfailing support and continuous encouragement throughout the study. Thank you.

Declarations

I, Claudia Mutongolume, hereby declare that this study is my own work and is a true reflection of my research, and that this work, or any part thereof has not been submitted for a degree at any other institution.

I, Claudia Mutongolume, grant The University of Namibia the right to reproduce this thesis in whole or in part, in any manner or format, which The University of Namibia may deem fit.

Claudia Mutongolume	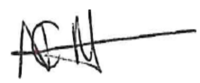	28/10/2020
Name of Student	**Signature**	**Date**

CHAPTER 1: INTRODUCTION

1.1. Background of the study

Geological mapping is a fundamental method in mineral exploration. This method is primarily used to describe the lithology and morphology of the outcrops as well as their relationships. Similarly, mapping collects structural data that can be used to predict the geology laterally or in the subsurface and provide clues to truncate ores. This information allows delineation of ore-bearing host rocks as well as alteration zones (Brimhall et al., 2006). Therefore, geological mapping is one of the methods used to prospect for mineral deposit in the study area, particularly copper.

The study area is located near Aus, southern Namibia, a small town situated about 125 km North-east of Lüderitz and along the main highway between Keetmanshop and Luderitz (Figure 1.1). Geologically, the area lies within the Mesoproterozoic Namaqua Sector of the Namaqua-Natal Metamorphic Province (NNMP). The sector hosts some of the world significant base metal sulphide deposits that have been mined for the past century. In northwestern South Africa, significant producers of Cu-Pb-Zn-Ag are; mines in the Aggeneys-Gamsberg ore district (Ryan et al., 1986; Moore et al., 1990; Bailie et al., 2007a, b), volcanic hosted massive sulphide deposits at the Prieska Copper Mine (Cornell et al., 1986; Cornell et al., 1990a, 1990b, Cornell et al., 1992; Bailie et al., 2010; Bailie et al., 2011) and Okiep Copper District (McIver et al., 1983; Schoch and Conradie, 1990; Cawthorn and Meyer, 1993; Clifford et al., 1995; Maier et al., 2013). In southern Namibia, porphyry type Cu-Mo prospects at Haib and Lorelei are reported to have considerable reserves, but the fall of metal prices have declared them uneconomical for extraction.

Generally, over the last three decades, a decline in the number of operating mines and commodity production, particularly copper, in the Namaqua sector has been recorded, and possibly ascribed due to the poor discovery of new deposits.

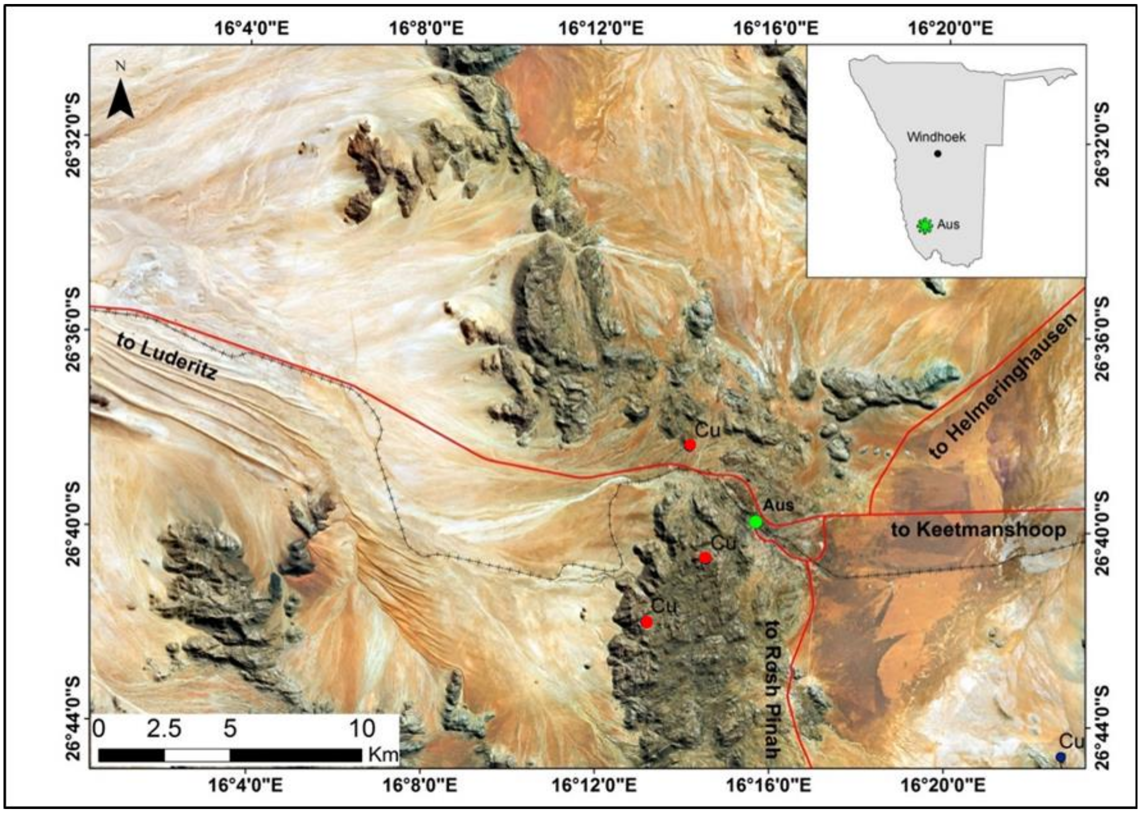

Figure 1. 1: Locality map showing the extent of the study area with copper occurrence (red dots) as reported by Schneider and Seeger (1992).

Copper is one of the most abundant of the metallic elements in the earth's crust and still one of the most sought after metals in modern society (Flanagan, 2018). It is mostly used in the electrical, motor vehicle manufacturing and construction industry (Nujoma, 2009). Copper has been mined for the past century and has contributed to the growth of the Namibian economy (Nujoma, 2009; Namibia National Planning Commission, 2018). Over the past decade new deposits have been discovered; Kunene Copper Project and

Okohongo Project in north-west Namibia, Tschudi Cu-Ag Mine in northern Namibia and Omitiomire Copper Project in central Namibia are some of the examples. This suggests that the country's potential for further new discoveries is high. In order to exploit these potential occurrences extensive geological mapping, research and grassroot exploration have to be carried out. Thus, the progressive search for new deposits and extension of existing ones is essential for the economic benefit of the country.

This project aims to evaluate the feasibility of known copper occurrences around the Aus area (//Karas region, southern Namibia) with the aid of detailed field mapping, petrography, whole rock geochemistry and U-Pb zircon dating. Interest emanates from the poorly documented copper deposits in the region (Schneider and Seeger, 1992). The study covers an area of 625 km^2 in the vicinity of town Aus (Figure 1.1), and the research took advantage of the joint mapping project between the Geological Survey of Namibia (GSN) and Council for Geoscience South Africa (CGS) that took place in the region during 2019. Mineralization found in the vicinity as well as the presence of altered rocks reveal the possibility of copper deposits within the area. A detailed geological map with precise localities of possible host rocks and copper showings in the study area is presented. Additionally, U/Pb age dating reported coincide with the mineralization age of Okiep Copper District located within Namaqua sector in South Africa.

1.2. Statement of the problem

The discovery of mineral deposits depends on the quality and interpretation of baseline geological, geophysical and geochemical data. In developing countries such as Namibia such data are not always available as parts of the country still lack detailed geological maps. Furthermore, the potential of some of the known copper deposits and their precise location remains poorly documented, with a resulting negative effect on the understanding of minerals depositional settings, ore genesis and economic potential. Therefore, this study aims to investigate the geotectonic setting of the area around Aus by conducting detailed geological mapping as well as petrographic and geochemical studies with the intent to characterise the feasibility of copper mineralization in the Aus area.

1.3. Objectives of the study

i. Establish a geological map of the Aus area (2616CA and 2616CB sheets) at 1: 50 000 scale and determine the host rocks for copper mineralization.

ii. Verify the geotectonic setting of the area using geochemistry.

iii. Determine the age of the Aus Domain using U-Pb zircon dating and establish the timing of associated copper mineralization.

1.4. Significance of the study

This study was initiated by the statutory mapping project of Precambrian basement rocks of the Namaqua Metamorphic Province, carried out by GSN and CGS, and aimed at improving the understanding of the regional geology of southern Namibia. As a result, a detailed geological map at 1: 50 000 scale was produced. Additionally, the study provides new data on the potential for copper mineralization in the vicinity of Aus, which could help in making informed decisions regarding mineral exploration in the area.

1.5. Limitation of the study

a) Due to the rugged nature of the terrain, it was not possible to access all of the relevant outcrops which should have been sampled.

b) There are no specialized laboratories in Namibia to carry out geochronology analysis, therefore age dating was carried out in Norway by a lecturer from the University of Namibia.

c) Due to financial constraints, the author could not travel to Norway to carry out geochronological analysis. Additionally, only few though representative and sufficient samples could be collected for analysis due to budget limits.

1.6. Delimitation of the study

This study investigates the occurrence of copper mineralization in accessible outcrops in the Aus area within 2616CA and 2616CB sheets only.

CHAPTER 2: LITERATURE REVIEW AND GEOLOGICAL SETTING

2.1. Regional Geology

2.1.1. The Namaqua-Natal Metamorphic Province

The Namaqua-Natal Metamorphic Province (NNMP) hosts a ~400 km wide Proterozoic metamorphic belt that extends for more than 1500 km (Figure 2.1) from southern Namibia to southeastern South Africa (Blignault, 1977; Blignault et al., 1983; Hartnady et al., 1985; Joubert, 1986; Thomas et al., 1994; Frimmel, 2000; Cornell et al., 2006). The belt is understood to form the southern African portion of the global Mesoproterozoic orogen linked to the assembly of the Rodinia Supercontinent between ca. 1350 and 1050 Ma (Hoffman, 1991, 1992). The amalgamation has traditionally been associated with a series of crustal blocks accreted onto the southern and southwestern margins of the Kaapvaal Craton in southern Namibia and South Africa, (Hartnady, 1985; Joubert, 1986; Humphreys & Van Bever Donker, 1987; Eglington & Armstrong, 2003; Colliston & Schoch, 2013), which led to the establishment of different litho- and tectonostratigraphic subdivisions. However, Macey et al. (2015) hold some rather different views about these “accreted” domains, which they consider to have resulted from reworking rather than accretion (see chapter 2.1.2).

The rocks along the belt were assembled during the Namaqua Orogeny between ca. 1200 and 1000 Ma, and are variably deformed, metamorphosed (Cornell et al. 2006; Miller 2008, 2012). The effects of the Namaqua Orogeny include voluminous intrusions of syn- and post-tectonic granitoids (Cornell et al. 2006; Miller 2008, 2012) and high-grade metamorphism (amphibolite facies and higher; Waters, 1986, 1988, 1989, 1990; Robb et al., 1999; Andreoli et al., 2006; Moen and Toogood, 2007; Macey et al., 2011; Diener et al., 2013). A detailed review on the evolution of the NNMP can be found in Cornell et al (2006) and Macey et al., (2011, 2015), and references therein.

Traditionally, the province is divided into two segments, i. e. the Natal sector in the southeast of South Africa and the Namaqua sector in southern Namibia and northwestern South Africa (Cornell et al., 2006; Frimmel, 2000). The study area is located within the Namaqua sector, southern Namibia.

2.1.2. The Namaqua Sector

Recent work done by Macey et al. (2015) redefined and recognized different crustal blocks within the Namaqua Sector. The major subdivisions of the Namibian part of the Namaqua Sector from north to south are a) Konkiep Domain (formerly known as Konkiep Subprovince), b) Kakamas Domain (formerly known as Gordonia Subprovince, subdivided into Kakamas and Grunau Terranes), c) Aus Domain (formerly known as Aus Terrane) and d) Richtersveld Magmatic Arc formerly known as Richtersveld Subprovince which comprise the Vioolsdrift, Pella and Sperrgebiet Domains (Blignault et al., 1983; Hartnady et al., 1985; Joubert, 1986; Thomas et al., 1994; Colliston and Schoch, 2000; Frimmel, 2000; Miller, 2008; Macey et al., 2015) as shown in Figure 2.1. The subdivisions are separated by major structural discontinuities and differentiated on the basis of lithostratigraphy, tectonic history and metamorphic grades (Hartnady et al., 1985; Colliston & Schoch, 1996; Cornell et al., 2006; Miller, 2008). However, much of the subdivision determining criteria remains debatable, and multiple interpretations have evolved (Joubert, 1986; Colliston et al., 1989; Colliston and Schoch, 2006; Thomas et al., 1994; Moen and Toogood, 2007; Macey et al., 2017). The study area is located within the Aus Domain.

A number of authors (e.g. Cornell et al., 1992; Becker et al., 2006; Colliston & Schoch, 2013; Bial et al., 2015a; Macey et al., 2015; Indongo, 2017) described the processes which led to the current configuration of tectonic domains, in an attempt to understand the specific geodynamic setting responsible for the regional Mesoproterozoic upper amphibolite to granulite signature. Their various interpretations of the regional tectonic settings encompass: 1) a continental collision model (e.g Blignault et al., 1983; Jacobs et al., 1993; Thomas et al., 1994; Eglington, 2006), 2) a continental back-arc setting (Waters, 1986; Bial et al., 2015a, 2016), and 3) magmatic under- or intra-plating accompanied by compressional tectonics (e.g Robb et al., 1999; Diener et al., 2013) under medium- to low pressure and high temperature granulite facies metamorphism. Recent work by Colliston and Schoch, (2013) and Colliston et al. (2015) presented evidence for extended compressional tectonics and proposed a collision of crustal fragments model.

2.2.Local Geology

2.2.1. Aus Domain

The Aus Domain is dominated by voluminous and extensive Mesoproterozoic (1220-1050 Ma) high-grade, upper amphibolite to granulite facies, aluminous paragneisses and granitoids rocks (Blignault et al., 1983; Colliston & Schoch, 2006; Cornell and Pettersson, 2007; Macey et al., 2015). The Kakamas and Aus Domains have similar rock types and metamorphic grades, but differ in the age of tectonism and metamorphism (Diener et al., 2013). The high-grade gneisses and granitoids of the Kakamas and Aus Domains are believed to be derived from the pre-existing older crust of the Paleoproterozoic Richtersveld Magmatic Arc and early Mesoproterozoic Areachab Arcs (Joubert, 1986; Macey et al., 2015). The latter were completely reworked through high-grade metamorphism and intense plutonism during the mid-Mesoproterozoic and subsequently thrusted into imbricated sheets over the Richtersveld Magmatic Arc during the mid- to late-Mesoproterozoic D2 (see chapter 2.3) of the Namaqua Orogeny (Reid, 1997; Nordin, 2009; Samskog, 2009; Macey et al., 2015). The thrust zone is characterized by the Lower Fish River-Onseepkaans Thrust along which the high-grade rocks of the Kakamas and Aus Domains were thrusted over the medium- to low-grade rocks of the Richtersveld Magmatic Arc (Blignault et al., 1983; Colliston and Schoch, 2013, 2000; Macey et al., 2015; Miller, 2012, 2008; Moen and Toogood, 2007).

A study by Jackson (1976) within the Aus Domain identified a high-grade metamorphic supracrustal assemblage, the Garub Group (Miller, 2008), and two suites of intrusive igneous rocks. The Garub Group contains the oldest rocks in the Aus area and comprises metapelitic and metapsammitic gneisses, with subordinate quartzite, mafic granulite, marble, calc-silicate and ironstone, which have been metamorphosed under amphibolite to granulite facies conditions and locally experienced anatexis (Jackson, 1976). Intrusive rocks comprise both pre-tectonic and syn- to post-tectonic orthogneisses. The pre-tectonic intrusive orthogneisses are strongly deformed, demonstrate linear fabrics and contain xenoliths of the Garub Group as proof of their plutonic origin. A garnet-bearing tonalitic to granodioritic augen gneiss referred to as Tsirub gneiss represents the oldest igneous suite and pre-tectonic intrusive in this area, having been emplaced shortly before the peak granulite facies metamorphism (Jackson, 1976; Diener et al., 2013). Widespread syn-tectonic magmatism led to the emplacement of the schlieren-rich, leucocratic sheeted Kubub granite gneiss and the coarse-grained, K-feldspar megacrystic Aus leucogranite gneiss (Jackson, 1976). U–Pb zircon dating of pre-, syn- and post-tectonic granitoid intrusions indicates that granitoid plutonism occurred at ca. 1120–1085 Ma, whereas metamorphic overgrowths on these zircons constrains metamorphism to have occurred between ca. 1065 to 1045 Ma (Diener et al, 2013). A granite dyke believed to be post-tectonic intruded after the domain cooled to subsolidus temperatures and records an age of 1004 ±6 Ma (Diener et al, 2013).

2.3.Deformation history

The Namaqua Sector rocks record a complex structural and metamorphic history. Various deformation episodes have been reported by a number of previous workers (e.g. Beukes, 1973; Jackson, 1976; Toogood, 1976; Blignault, 1977; Blignault et al., 1983; Hartnady et al., 1985; Joubert, 1986; Moen and Toogood, 2007; Diener et al., 2013). In the study area, five phases of deformation (D1–D5) were identified associated with high-grade metamorphism (Jackson, 1976). The first two phases are defined by foliations and lineations developed in the Garub Group and Tsirub Gneiss, the third by foliations developed in the syn-tectonic Kubub and Aus gneisses. The D1 fabrics are thought to have developed in the Paleoproterozoic during the Orange River Orogeny between ca. 1900-1850 Ma (Blignault, 1977; Blignault et al., 1983). The second episode of deformation (D2) occurred during the Namaqua Orogeny at 1200-1000 Ma (Blignault et al., 1983; Raith & Harley, 1998; Miller, 2008). The D2 Namaqua Orogeny is the most pervasive in the study area and believed to be responsible for the prominent planar and linear ductile fabrics associated with changes in metamorphic grade within the rocks of Gordonia and Richtersveld Richtersveld Magmatic Arc (Colliston & Schoch, 2000; Macey et al., 2015; Miller, 2008). The third episode of deformation (D3) is suggested to have occurred during the late stages of Namaqua tectonism and formed kilometre-scale F3, upright to inclined, shallowly- plunging open folds as a result of compressional ductile deformation (Macey et al., 2011).

The D4 deformation phase is associated with the development of sub-parallel dextral shear zones between 1050 and 960 Ma (Colliston & Schoch, 2013, 2002, 2000; Joubert, 1986; Lambert, 2013; Macey et al., 2015; Moen & Toogood, 2007; Toogood, 1976; Angombe, 2016; Indongo; 2017), which include the Eureka Shear Zone, Marshall Rocks-Pofadder Shear Zone and Sperlingsputs Shear Zones (refer to table 2.1 for a summary). Within the Aus Domain, only the Marshall Rocks-Pofadder Shear Zone is recorded. The D5 event is characterized by post-Namaqua north-south trending faults-cross cutting D1, D2, D3 and D4 fabrics.

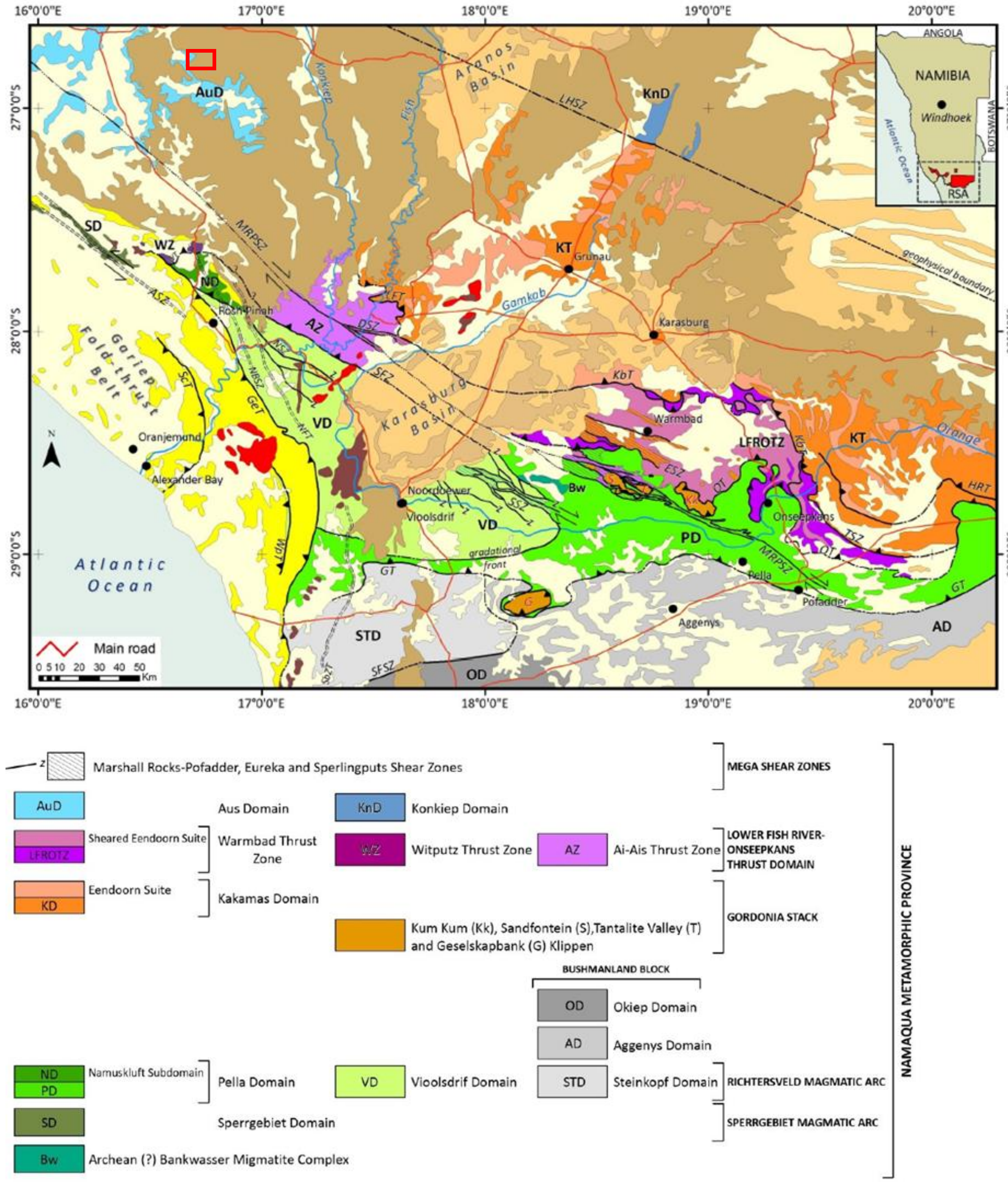

Figure 2. 1: Tectonic architecture of the Namaqua sector of the NNMP (after Macey et al. 2014, 2015, 2016) Domains boundaries of Namaqua sector: D2 Namaqua shear zones and thrusts: Lord Hill Shear Zone (LHSZ), Kêrelbad Thrust (KbT), Hartebees Rivier Thrust (HRT), Tafelkop Shear Zone (TSZ), Onseepkans Thrust (OT), Lower-Fish River Thrust (LFT), Groothoek Thrust (GT), Southern Namaqua Front/thrust (SF), Witputz Thrust (WT), Skelmfontein Shear Zone (SFSZ); D4 Namaqua shear zones: Marshall Rocks-Pofadder Shear Zone (MRPSZ), Sperlingsputs Shear Zones (SSZ), Eureka Shear Zone (ESZ), Dreikopf Shear Zone (DSZ); D5 Pan African thrusts, shear zones and faults: Gemsbokvlei Thrust (GeT); Wildeperdrand Thrust (WpT); Schakalsberg Thrust (ScT); Nuab River Shear Zone (NSZ); Namusberge Shear Zone (NBSZ); Nama-Foreland Thrust (NFT); Aurus Shear Zone (ASZ). Red box= study area.

Table 2. 1: Summary of the deformation sequences and timing of major structural events (after Macey et al., 2015) taken from Angombe (2016).

NEOPROTEROZOIC TO CRETACEOUS	POST-NAMAQUA BRITTLE DEFORMATION	D_5		Development of brittle structures (faults, joints and quartz veins) cross-cutting D_1,D_2,D_3 and D_4 fabrics	POST-NAMAQUA
EARLY NEOPROTEROZOIC	(MARSHALL ROCKS-POFADDER, EUREKA & SOUTHERN NAMAQUA	D_4	Development of crustal-scale shear zones associated with brittle-ductile deformation at amphibolite- greenschist facies grade	Development of three brittle-ductile, dextral, NW-SE trending shear zones; the Eureka Shear Zone, Marshall Rocks-Pofadder Shear Zone and Sperlingsputs Shear Zone. Shear zones overprint pre-existing structures and reactivate older thrust boundaries	POST-TERRANE JUXTAPOSING
MESOPROTEROZOIC	NAMAQUA OROGENY (~1200-1000 Ma)	D_3	Mega-scale folding	Development regional scale open fold (F_3), domes and basin structures	
		D_2	Two main phases of thrusting & terrane juxtaposition	2) Thrusting of the granulite facies Kakamas Domain of the Gordonia Subprovince on top of the amphibolite facies Pella Domain of the Richtersveld Subprovince along the Lower Fish River Onseepkans Thrust Zone (LOFRTZ).	SYN-TERRANE JUXTAPOSING
			Regional high grade ductile deformation	1) Development of regional ductile LS-tectonite fabrics of higher metamorphic (amphibolite and granulite facies) grade in rocks of the Pella and Kakamas domains	
PALEOPROTEROZOIC	ORANGE RIVER OROGENY (~1900 - 1850 Ma)	D_1	Greenschist facies deformation	The first deformation recorded in the Namaqua sector, overprinted by D_2 and restricted to the Vioolsdrift Domain (Not observed in the study area.) (western Richtersveld Subprovince).	PRE-TERRANE JUXTAPOSING

2.4. Metamorphism

The Aus Domain is characterized by high temperature low pressure metamorphic event (Diener et al., 2013). The study area predominantly consists of a variety of pre- and syn-tectonic gneisses and minor supracrustal rocks. These rocks have been metamorphosed and migmatised with cordierite coronas having grown around garnets at peak metamorphic conditions of 5.5 kbar and 825 °C (Figure 2.2; Jackson, 1976; Diener, 2013); various clockwise and anti-clockwise P-T paths have been proposed (Waters, 1989; Diener et al., 2013). The anti-clockwise P-T path has been interpreted to be due to the replacement of cordierite by garnet and sillimanite ± biotite subsequent to the development of the peak assemblage (Waters, 1989; Robb et al., 1999). However, Diener et al (2013) inferred the replacement of prograde garnet by cordierite to represent minor decompression subsequent to peak conditions. The replacement of cordierite by fibrolitic sillimanite is ascribed to retrograde cooling and thus suggests a clockwise P-T loop, attributing this event to magmatic under- or intraplating. Recent work by Bial et al (2015a) reported a similar isobaric cooling in the Kakamas Domain, south east of Aus Domain (Figure 2.2).

The D2 events (D2a and D2b; Table 2.1) correlate with the two discrete metamorphic events (M2a and M2b) at ca. < 1.2 and 1.06 Ga as illustrated in Figure 2.2 (Raith and Harley, 1998). Additionally, Raith and Harley (1998) suggest that M2a occurred concurrent with the principal regional tectonogenesis at < 1200 Ma, whereas M2b is characterised by retrograde assemblages developed along late D2 shear zones at slightly lower temperatures. These findings are in agreement with Clifford et al. (2004) who postulate that granitoid magmatism occurred concurrent with regional D2 deformation at 1180 - 1200 Ma and resulted in peak P-T conditions. The high temperature conditions resulted in melting of semi-pelitic and pelitic Garub Group rocks to produce migmatites; melting also caused the production of large masses of homogeneous granitoids during the culmination of regional migmatisation accompanying amphibolite facies metamorphism (Jackson, 1976).

Zircon overgrowths aged 1060-1030 Ma are interpreted to correspond to peak metamorphism. The development of the peak assemblage in the NNMP probably post-dated the principal D2 period of deformation, but was synchronous with the development of D3 open folds (Robb et al., 1999; Figure 2.2), assigning this event to magmatic under or intraplating.

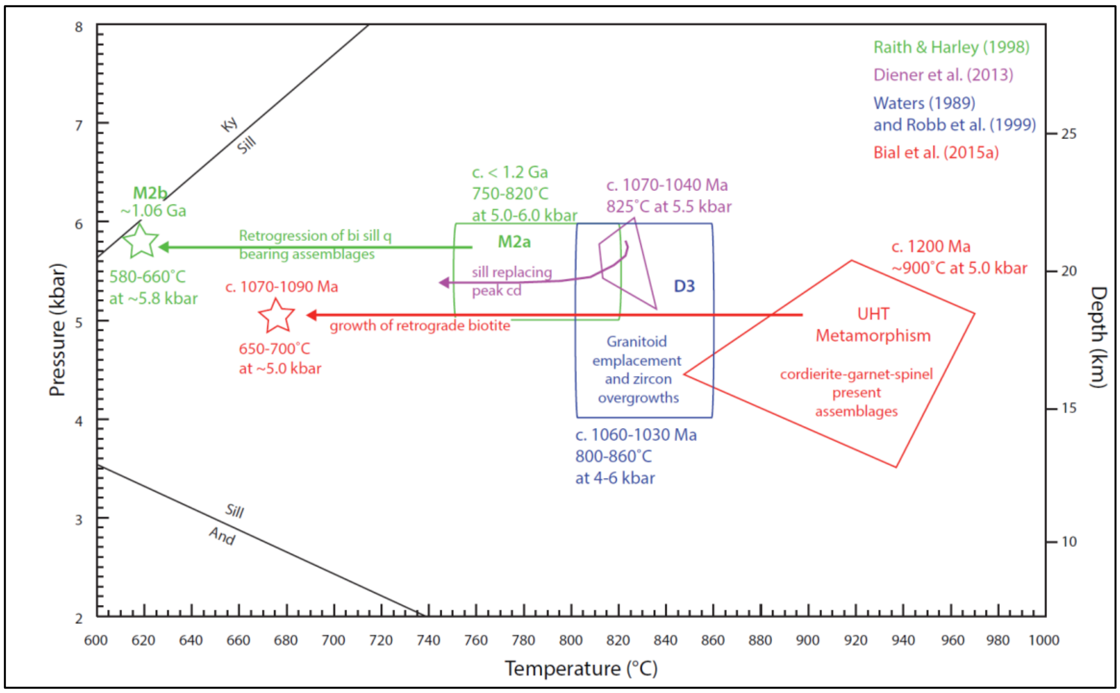

Figure 2. 2: Metamorphic P-T constraints in the Namaqua sector from previous studies. Arrows indicate early retrograde trajectories deduced by the respective workers. Note the early, minor decompression stipulated by Diener et al. (2013). The timing of P-T constraints is indicated as per the relevant studies. UHT = ultra-high temperature (after Sebetlela, 2017).

2.5. Economic Significance of NNMP

Mineralization events within the NNMP are reported to have occurred throughout the tectonic evolution of the belt, from pre-Kibaran (Eburnian) times, through the early volcano-sedimentary stage to collision (orogenic) and post-collisional magmatism (Cornell et al., 1992). With reference to the Namaqua Sector, the arc-related ~2000 Ma Haib Cu-Mo porphyries within the Richtersveld Magmatic Arc are correlated to an Orange River Orogeny, before the Namaqua basement was established (Barr and Reid, 1993). During the early rifting stage of the Kibaran cycle (1600 – 1300 Ma), the Cu-Pb-Zn SEDEX deposits located in the Natal sector formed on this older crust in a stable shelf environment. The volcanogenic-exhalative sulphide deposits (Aggeneys and Gamsberg deposits) were originated as a result of arc magmatism at ~1300 Ma (Theart et al., 1989; Schade et al., 1989). Crustal thickening during the collisional and post–collisional phase of the orogeny at ~ 1200 to 1100 Ma led to the generation of syn- to late tectonic granitic magmas, which gave rise to widespread orthogneisses, pegmatites (feldspar, muscovite, beryl and tantalite-columbite bearing) and epithermal vein deposits (Bowles, 1988). Additionally, crustal thickening at the margin of the Namaqua Belt resulted in anorthositic magmatism, which is associated with Cu and Cu-Ni mineralization, such as the O'kiep Copper Deposit.

In the Aus area, the copper showings reported are associated with supracrustal and intrusive rocks (Schneider and Seeger, 1992). Some 16 km southeast of Aus, extensive malachite-staining is associated with a highly ferruginous zone in amphibolite. Rock chip sampling over the mineralised area yielded sporadic best values of 0.4% copper (Schneider and Seeger, 1992). Gossans in copper-stained graphitic schist are traceable for several kilometres near the boundary between the farms Kubub 15 and Heinrichsfelde 10, about 12 km southwest of Aus (Seeger, 1978).

Hydrothermal systems usually form in specific tectonic settings e.g porphyry systems mostly occur in magmatic arc settings (Sillitoe, 1972; Tosdal and Richards, 2001; Kwelwa et al., 2018). At a regional scale, hydrothermal deposits show close proximity to regional faults system or shear zones, which serve as pathways for transporting ore-forming fluids from deep-seated sources to shallow depositing spots (Sillito, 2003; Zeng et al., 2018). At a deposit scale, hydrothermal replacement disseminations, breccias and veins, which are related to subsidiary fracture zones of regional structures, serve as favorable sites for focusing and depositing the ore-bearing fluids and are interpreted to be responsible for localization of orebodies (Zeng et al., 2018).

CHAPTER 3: RESEARCH METHODOLOGY

This study was carried out into four main phases.

3.1.Phase 1: Literature survey and remote sensing datasets

Existing geological maps, remote sensing data, geophysical imagery was used to produce pre-field basemaps. The use of Sentinel, ASTER and high resolution airborne magnetic imagery aided in the discrimination of mineral alteration zones, rock types and prominent structural features (Figure 3.1). ASTER and Sentinel data were processed using ENVI software. Other software like Google Earth and ArcGIS were used to compile, geo-referenced and export various maps and figures. All the remote sensing data set was acquired from the digital library of Geological Survey of Namibia.

3.2.Phase 2: Field mapping and data collection

Field work was carried out over a period of 26 days, spread over 2 field visits between May and June 2019. Access to the outcrop was by foot and 4WD vehicle. In the field, locality readings were recorded with a Garmin GPS and structural measurements were recorded using Breithaupt compass set at a magnetic declination of 16° west. At the completion fieldwork, structural and location data was plotted in the ArcGis and Google Earth software and using a number of satellite images (Figure 3.1).

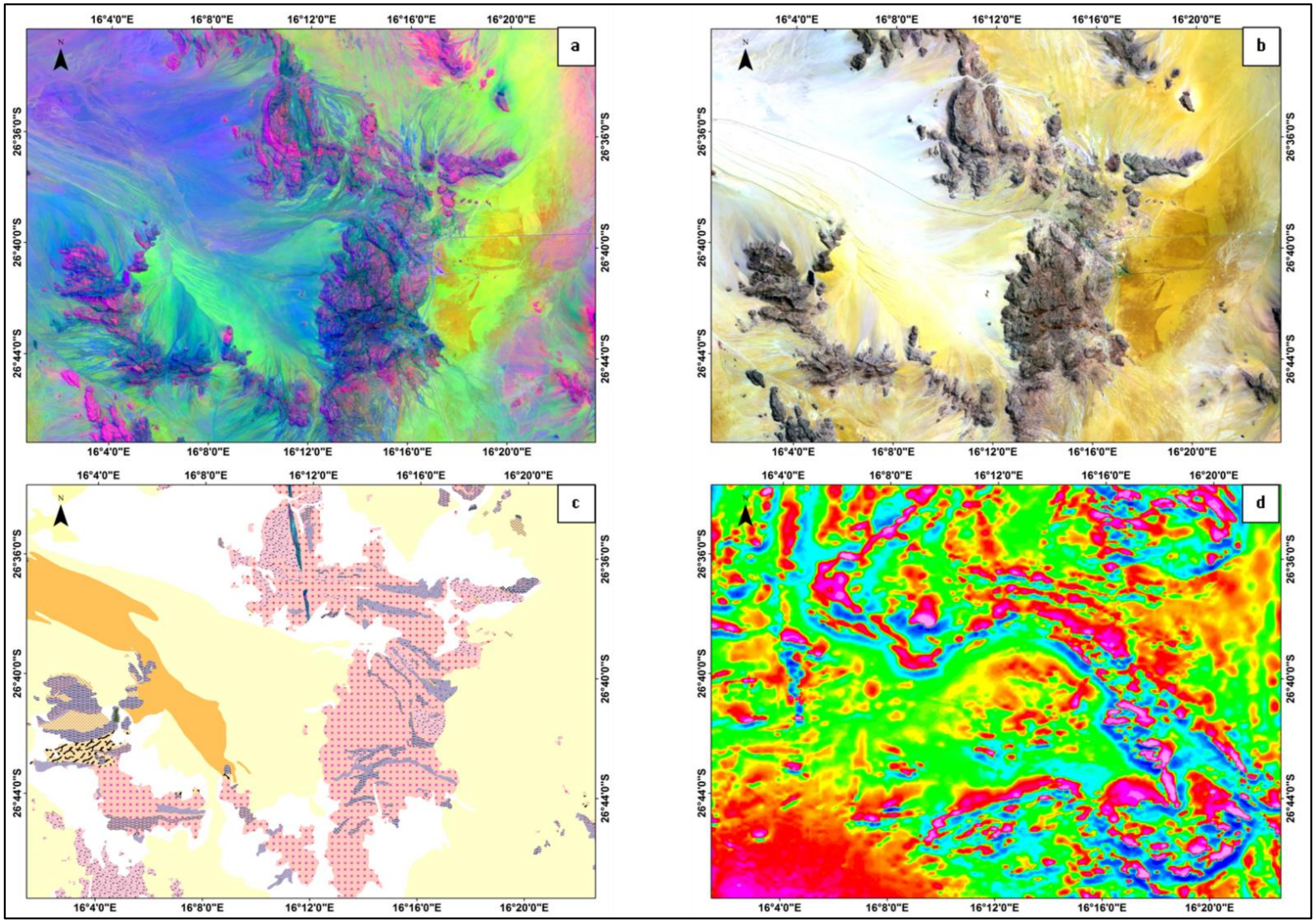

Figure 3. 1: Various Images and maps used in the study. A) Sentinel (RGB 12/11, 4/2, 4/11) band combination, B) Aster (RGB 321), C) Existing 250 000 scale geological map (after Jackson, 1975) and D) Magnetic (First Derivative) image. All data sourced from GSN database.

3.3.Phase 3: Analytical methods and research phase

3.3.1. Petrographic sections

Twelve samples were submitted for normal thin sections. The rock samples where cut to produce petrographic sections at the Geological Survey of Namibia Laboratories in Windhoek. Thin sections were examined using transmitted light petrographic microscope. Photomicrographs of the rocks were taken using a camera mounted on the microscope.

3.3.2. Geochemistry

A total of eighteen samples were submitted for geochemical analysis at the University of Stellenbosch laboratories, South Africa. Five of these samples were prepared at the Geological Survey of Namibia Laboratories by the author. The samples were crushed with a jaw crusher into less than 2 cm chips. These chips were milled at <75 μ powder fraction. About 1 g volume of each sample was sealed in a bag and submitted for major and trace element analysis to the University of Stellenbosch laboratories, South Africa, together with the rest of the samples. Major elements were analyzed using the X-ray Fluorescence (XRF) technique and trace elements by Inductively Coupled Plasma Mass Spectrometry (ICP-MS).

For major element analysis, the milled sample (<75 μ fraction) was roasted at 1000 °C for at least 3 hours to oxidise Fe^{2+} and S and determine the loss on ignition (L.O.I.). Glass disks were prepared by fusing 1.5 g of the roasted sample and 9 g flux consisting of 66.67% Li_2B4O7, 32.83% $LiBO_2$ and 0.50% LiI at 950 °C. For trace element analysis 12 g milled sample and 3 g Hoechst wax were mixed and pressed into a powder briquette by a hydraulic press with an applied pressure of 25 tonnes per square meter.

The glass disks and wax pellets were analysed by a PANalytical Axios X-ray fluorescence spectrometer equipped with a 4 kW Rh tube.

ICP-MS trace element and rare earth element (REE) analyses were carried out using a Perkin-Elmer ELAN 6000. A three-step HNO_3 acid digestion method following that of Le Roex et al. (2001) was used to obtain solutions. Approximately 50 mg of sample were weighed out into Teflon containers (Savilex beakers) and 4 ml of a 3:1 HF/HNO_3 was added. The container was then placed on a hot plate for 48 hours for digestion. Once the samples were dry another 2 ml of concentrated nitric acid (HNO_3) was added and the mixture reheated on a hot plate till dry. The latter procedure was repeated once more. Once the sample was dry, a final addition of 5% nitric acid was added and the container was moved to a centrifuge tube and placed into an ultrasonic bath for dissolution. After dissolution, the sample was ready for use in the ICP-MS spectrometer. Errors were better than 3% and detection limits within the lower ppb range. Results are shown in Appendix F.

3.3.3. U-Pb Geochronology

Two rock samples (CM19098 and CM19099) weighing about 2 kg each were collected for zircon dating. These samples were prepared at the Geological Survey of Namibia by the author. The rocks were crushed with a hammer into <20 mm rock chips. The <20 mm chips were milled with a manual swing mill for 30 seconds. The milled fraction was sieved to obtain <250 μm powder and the residue was re-milled to achieve the desired fraction. The <250 μm powder was washed with tap water and panned in order to separate heavy and light minerals. The heavy minerals were then transferred to a clean A3 paper and dried for 72 hours. The heavy minerals were run through a magnetic separator (Frantz instrument model LB-1) to separate the magnetic and non-magnetic minerals. The non-magnetic minerals were put into the heavy-liquid separator, bromoform, to further concentrate the heavy minerals such as zircons. The concentrate at the bottom was then washed with acetone and dried. From each sample, about 40 zircon grains were handpicked with a needle under a light microscope, mounted in epoxy and polished. Zircon analysis (U-Pb isotopes) was conducted at the University of Oslo, Norway.

Each zircon was imaged and numbered using a Hitachi S-3400N Scanning Electron Microscope. Backscattered electron (BSE) and cathodoluminescence (CL) images of individual zircons were obtained and examined to identify age domains, metamict zones and cracks. U-Pb dating was done using a Nu Plasma HR multicollector inductively coupled plasma mass spectrometer (ICP-MS). The 91500 zircon was used as a standard and mounted in the same epoxy puck as the sample zircons. Common Pb corrections are based on the measured ^{204}Pb signal assuming the present-day model Pb composition of Stacey and Kramers (1975). Details of the analytical procedure followed are given in Cornell et al. (2015). The calculation of Concordia ages and plotting of Concordia diagrams, histograms and probability density plots were done with the EXCEL program ISOPLOT- v4.15 of Ludwig (2012). All age errors are given in the text at the 2σ uncertainty level. Analytical result tables are attached as Appendix G.

3.4.Phase 4: Geological map and report compilation

A geological map of the study area at scale 1:50 000 was produced using a combination of imagery as shown in figure 3.1, field data and the results of petrographical, geochronological and geochemical analysis. Compilation was done manually using polyester overlays on Google Earth imagery and other ortho-rectified images as base materials (Figure 3.2). The georeferenced field data were used together with Google Earth imagery for continuous analysis during compilation. The drawing was scanned, vectorized and georeferenced, the latter using ArcGIS software. The final map is shown in figure 4.11.

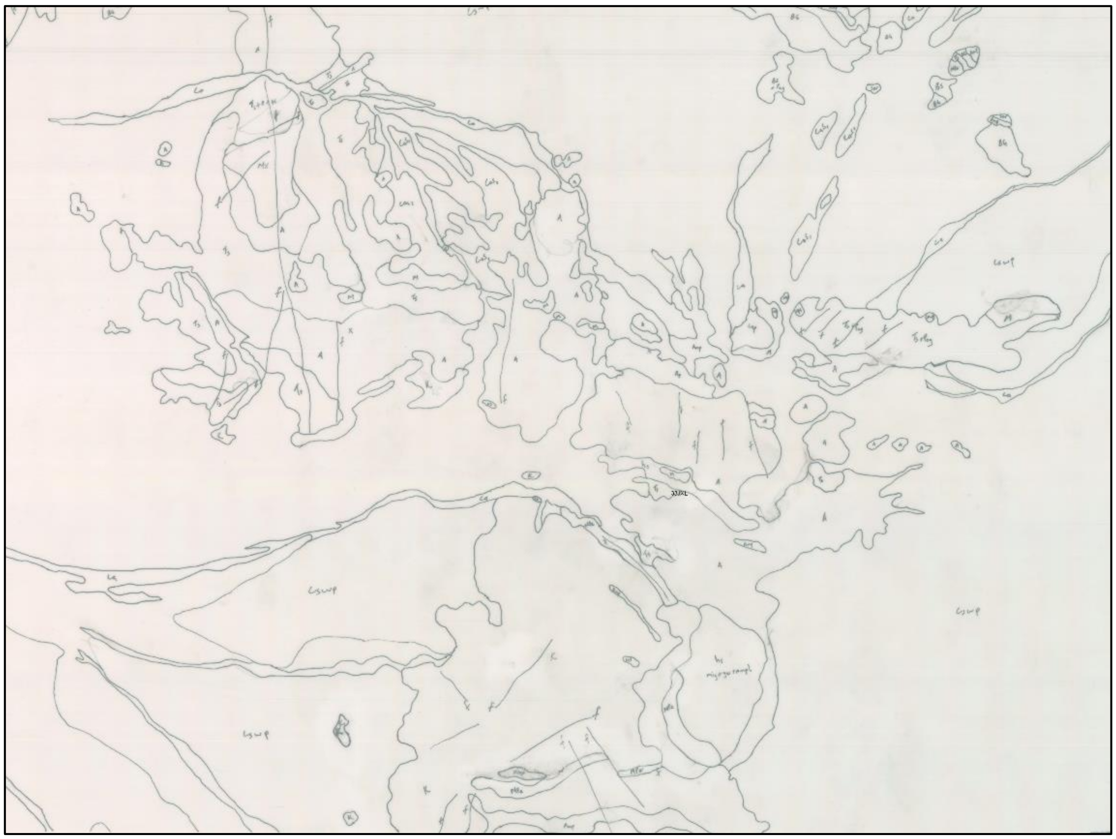

Figure 3.2: 1: 50 000 hand drawn geological map (2616CA and 2616CB) map sheets for Aus area.

CHAPTER 4: RESULTS

4.1. Introduction

This chapter presents the author's findings based on the field and analytical observations carried out within the study area. Field mapping and petrographic descriptions, geochemical and geochronology studies were used to help achieve the objectives of this study. Various lithologies were observed and mapped out. These includes the Garub Group also known as supracrustal rocks which comprise of marble, calc silicates, metapelites, garnet biotite gneiss, amphibolite, mafic granulites, pink quartz-feldpar rock and serpentinite. The Garub Group is intruded by the Tsirub augen gneiss, Aus granite gneiss, Kubub granite gneiss, warmbad granite and pegmatites. The occurrence of mafic granulites and warmbad granite found in the study area are too small to be represented on a map of 1:50 000 scale while pegmatite intrusions are represented as dykes on the map and only in the northern part of the map it is represented as a polygon. In the south west corner of the map are the Namib sand dunes of Sossus Formation which form the youngest geological units, together with undifferentiated surficial sediments and alluvium. The geological map is presented in Figure 4.12.

4.2. Lithologies and Petrographic description of rock units in the Aus Domain

4.2.1. Garub Group

4.2.1.1 Marble and calc-silicates (MGBm)

Marble and calc-silicates are distributed predominantly in the central part of the study area, where they form sporadic outcrops. The marbles usually form lenses (Figure 4.1 a), but are easy to recognize since they often are associated with a strong weathering surface (Figure 4.1 b). In outcrop, the marbles are light-brown to grey in color (Figure 4.1 b); and partly well banded. They are commonly interbedded with calc-silicates, amphibolites, quartzite and minor pelites (Figure 4.1 c). Calc-silicate crops out alternately as dark green and white weathering compositional bands that persist laterally for up to 10 m (Figure 4.1 d). The dark bands are characterized by carbonate rich minerals and the light bands are composed of minerals rich in silica.   The association of both marbles and calc-silicate is intruded by various granites present in the study area (Figure 4.1e). All the carbonate-bearing rocks are represented by a map colour blue on the geological map in Figure 4.12, because they are always in association.

In thin section, the marbles are coarse-grained and chiefly composed of 90% calcite with a granoblastic texture. Calcite grains contain simple twinning and lamellar twins on some grains (Figure 4.1e). The shapes of the grains are irregular and their boundaries display fluid inclusions. Calc-silicate is composed of wollastonite (50%), diopside (30%), quartz (10%) and calcite (10%, Figure 4.1f). Wollastonite is coarse grained and associated with fine-grained irregular diopside. Diopside share rims with wollastonite, quartz and calcite. Quartz and calcite occur close to each other and appear smaller in size with relative to diopside and wollastonite. Quartz is recrystallized and calcite occurs as minor anhedral remnant laths associated with diopside. The peak metamorphic assemblage for calc-silicate is Wollastonite + diopside + quartz. Calcite is present as a retrograde mineral together with epidote.

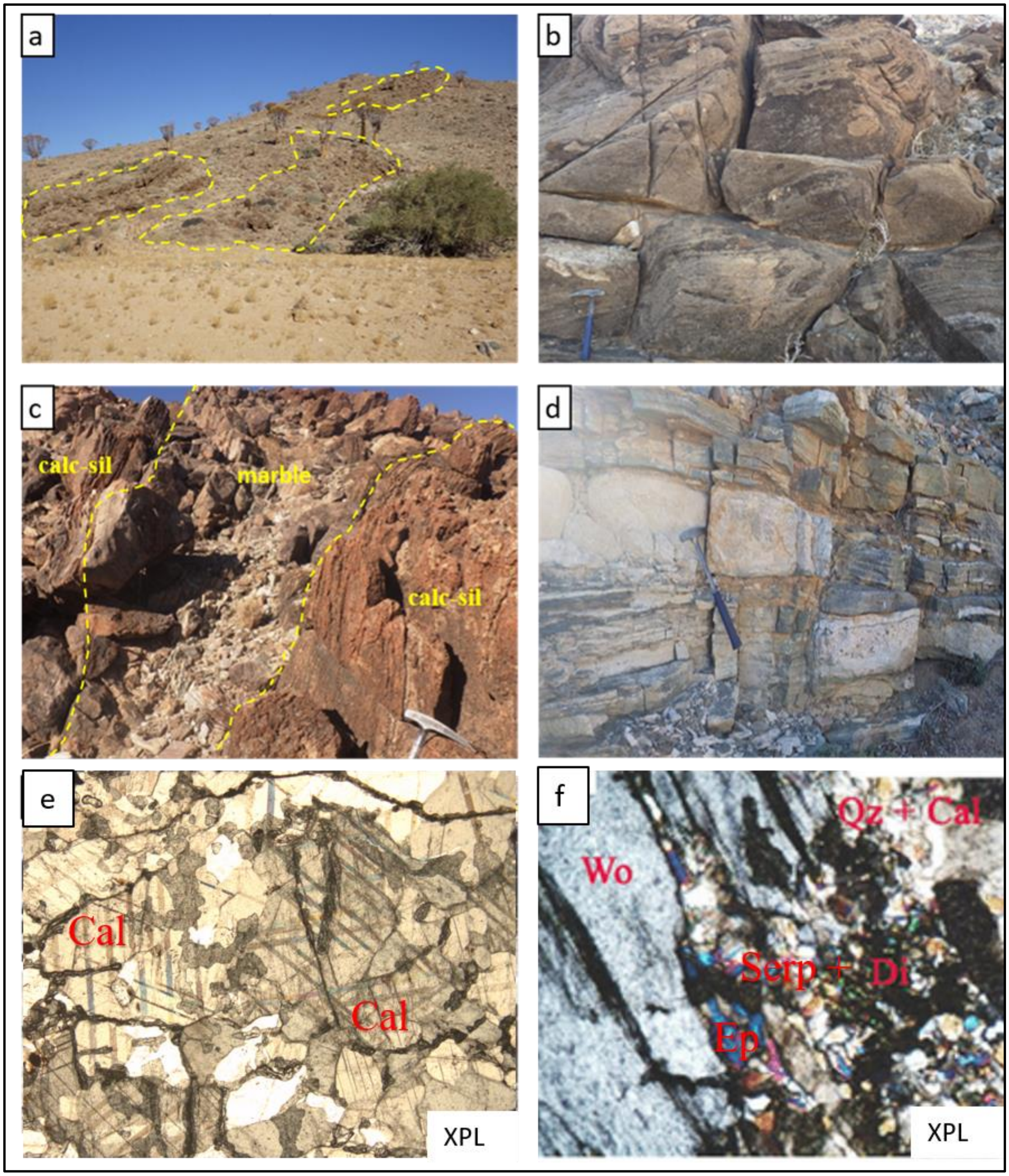

Figure 4. 1: a) lenses of marble (outlined in yellow) intruded by Aus gneiss (Waypoint CM19106); b) light brown to grey weathering marble (Waypoint CM19010); c) intercalation of calc-silicates with marble (CM19198); d) calc-silicates with light grey to greenish weathering surface (CM19108); e) Photomicrograph (FOV = 4.5mm) of marble and e) Photomicrograph (FOV = 4.5 mm) of calc-silicate. Cal: calcite, Qz; quartz, Di: diopside, Ep: epidote, Wo: wollastonite, FOV= field of view, XPL: Cross polarised light.

4.2.1.2. Aluminous gneiss/metapelites (MGBal)

Metapelites crop out mostly in the southern part of the study area, but slivers of these rocks also occur in the northern part. These rocks are easily recognisable in the field because of their dark red-brown weathering colour (Figure 4.2a). However, when the rock is fresh it has a distinctive dark grey colour (Figure 4.2b). Typically, the metapelites have compositional banding of different mineral assemblage of about 0.5 cm – 3 cm thickness defined by alternating leucocratic and melanocratic layers (Figure 4.2a and b). On the scale of the map, two laterally continuous and distinctive metapelitic units are recognised.

The metapelites are strongly deformed and the foliation is mostly defined by the preferred orientation of biotite which commonly occurs as platy clusters (Figure 4.2d). These rocks are intruded by most of the intrusive rocks in the study area (Figure 4.2e).

In thin section, the aluminous gneiss is typically medium to coarse grained and composed of garnet (25%), cordierite (20%), K-feldspar (20%), plagioclase (10%), sillimanite (10), hornblende (5%), biotite (5%) and quartz (5%) (Figure 4.2f). Cordierite from the metapelites is anhedral and fractured, while garnets form spheroidal porphyroblasts up to 3 mm in diameter and easily distinguished in hand specimen (Figure 4.2c). Garnet and cordierite are often altered and replaced by biotite, while plagioclase is sericitised. Similarly, garnet is partially replaced by cordierite. Sillimanite is fine- and coarse grained anhedral crystals with a random, planar orientation. Biotite is strongly pleochroic from brown to very deep red and occurs as anhedral and subhedral flakes. K-feldspar is more abundant than plagioclase, and its relative proportion to plagioclase increases significantly in leucosomes. Quartz grains are partially or completely recrystallized, with a transition from subgrain boundary to neoblast development.

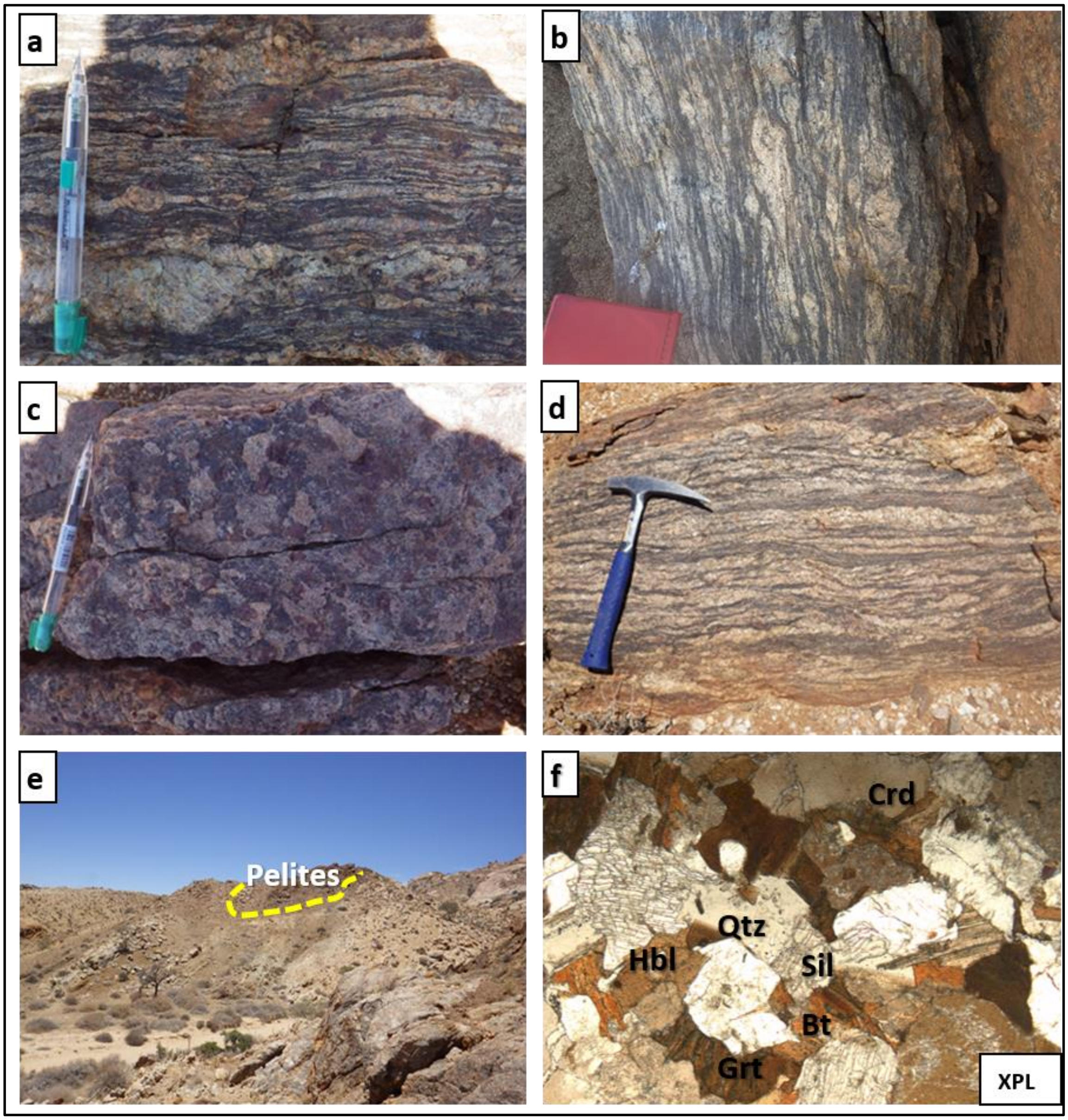

Figure 4. 2: a) Banded Metapelite with garnet, biotite and k-feldspar (Waypoint CM19127); b) compositional bands within the Metapelites (CM19117); c) porphyroblastic garnets in the Metapelites (CM19127); d) platy clusters of biotite with a preferred orientation (CM19127); e) Panorama of Kubub gneiss invading the Metapelites (CM19127) and f) Photomicrograph (FOV = 4.5mm) showing highly altered garnet (Grt) and cordierite (Crd) which is replaced by biobite (Bt). Sillimanite (Sil) occurs as fibres between hornblende (Hbl), quartz (Qtz) and biotite (Bt). FOV= Field of view. XPL= Cross polarised light.

The peak metamorphic assemblage in the metapelites is garnet + cordierite + sillimanite + hornblende + K-feldspar + plagioclase + biotite + quartz, which shows upper amphibolite facies.

4.2.1.3. Garnet Biotite Gneiss (MGBbg)

The mesocratic garnet biotite gneiss is found in the north and southern part of the study area, but the most significant outcrops occur in the northern section (Figure 4.3a). This rock displays gray or brownish gray weathering. Layering in these gneisses is conspicuous with a display of leucocratic and melanocratic layers with a migmatitic appearance (Figure 4.3b), and a marked preferred orientation of biotite. Intercalations with other supracrustal units are concordant with this layering. The foliation within the garnet biotite gneiss is mostly parallel with adjacent units (Figure 4.3c). The garnet biotite gneiss is in sharp contact with marble (Figure 4.3d), locally it is intruded by plutonic rocks within the study area (Figure 4.3d).

In the thin section, garnet biotite gneiss is medium to coarse grained chiefly comprised of plagioclase (35%), quartz (30%), biotite (10%), garnet (10%) and accessories of hornblende (3%) with a granular texture (Figure 4.3f). The twins in the plagioclase are not well defined and contain tiny inclusions of anhedral quartz. Quartz forms anhedral grains that show ubiquitous strain shadows. This implies that the garnet biotite gneiss has undergone deformation. Strongly pleochroic biotite laths ranging from pale yellow to reddish brown occur as subhedral crystals with ragged terminations. They have a distinct preferred orientation that is parallel to compositional banding.

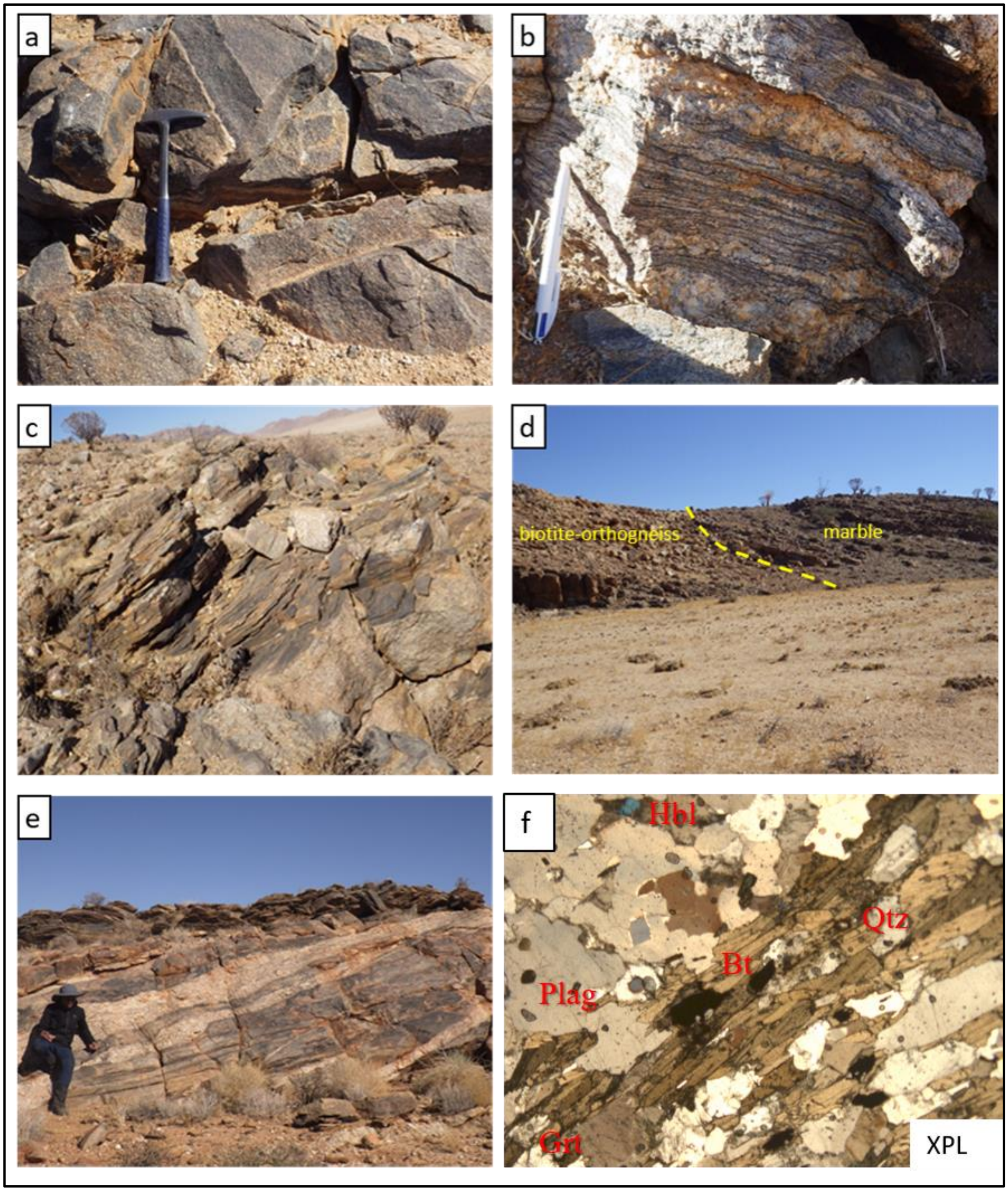

Figure 4. 3: a) medium-grained garnet biotite gneiss; b) migmatitic texture of garnet biotite gneiss (Waypoint CM19103); c) strongly deformed garnet biotite gneiss (CM19100); d) sharp contact between garnet biotite gneiss and marble (CM19101); e) pegmatite invading the gneisses (CM19035) and f) Photomicrograph (FOV = 4.5mm) of garnet biotite gneiss. Hbl: hornblende, Plag: plagioclase, Grt: garnet, Bt: biotite, Qtz: quartz, FOV= Field of view. XPL= Cross polarised light.

Olive green hornblende is anhedral and occurs next to biotite. The black opaque mineral is zircon which occurs within the biotite grains. The peak metamorphic assemblage is made up of garnet + hornblende + plagioclase + biotite + quartz. Late chlorite is present as a retrograde mineral together with sericite that replaces plagioclase grains.

4.2.1.4. Garnet Amphibolites (MGBa)

The garnet amphibolites crop out mostly in the central part of the study area, particularly north of Aus. However, thin but significant units are present throughout the area (Figure 4.4a). The garnet amphibolites are melanocratic in colour which exhibit a very weakly developed fabric almost in the entire study area (Figure 4.4b). These units are commonly associated with metasedimentary rocks, mostly in the form of repeated intercalations with marble, calc-silicates and metapelites (Figure 4.4c). The garnet amphibolites are intruded by the granite gneisses found in the study area (Figure 4.4d and e).

In the thin section, the garnet amphibolite is a, fine to medium-grained rock with an inequigranular texture, which comprises plagioclase (40%) and hornblende (35%) as major minerals, whilst biotite (10) and garnet (15%) occur in minor amounts (Figure 4.4f). Plagioclase is the most abundant mineral, medium grained with subhedral grains with twin lamellae texture. The grain boundaries between adjacent plagioglase are curved, while those against other crystals are scalloped. The plagioclase grains are partially or wholly altered to sericite. Hornblende is fine to coarse grained, pleochroic beige to pale brown. Flaky biotite is fine grained with tan brown to colourless pleochroism with a random distribution. The peak mineral assemblage is garnet + hornblende + plagioclase + biotite.

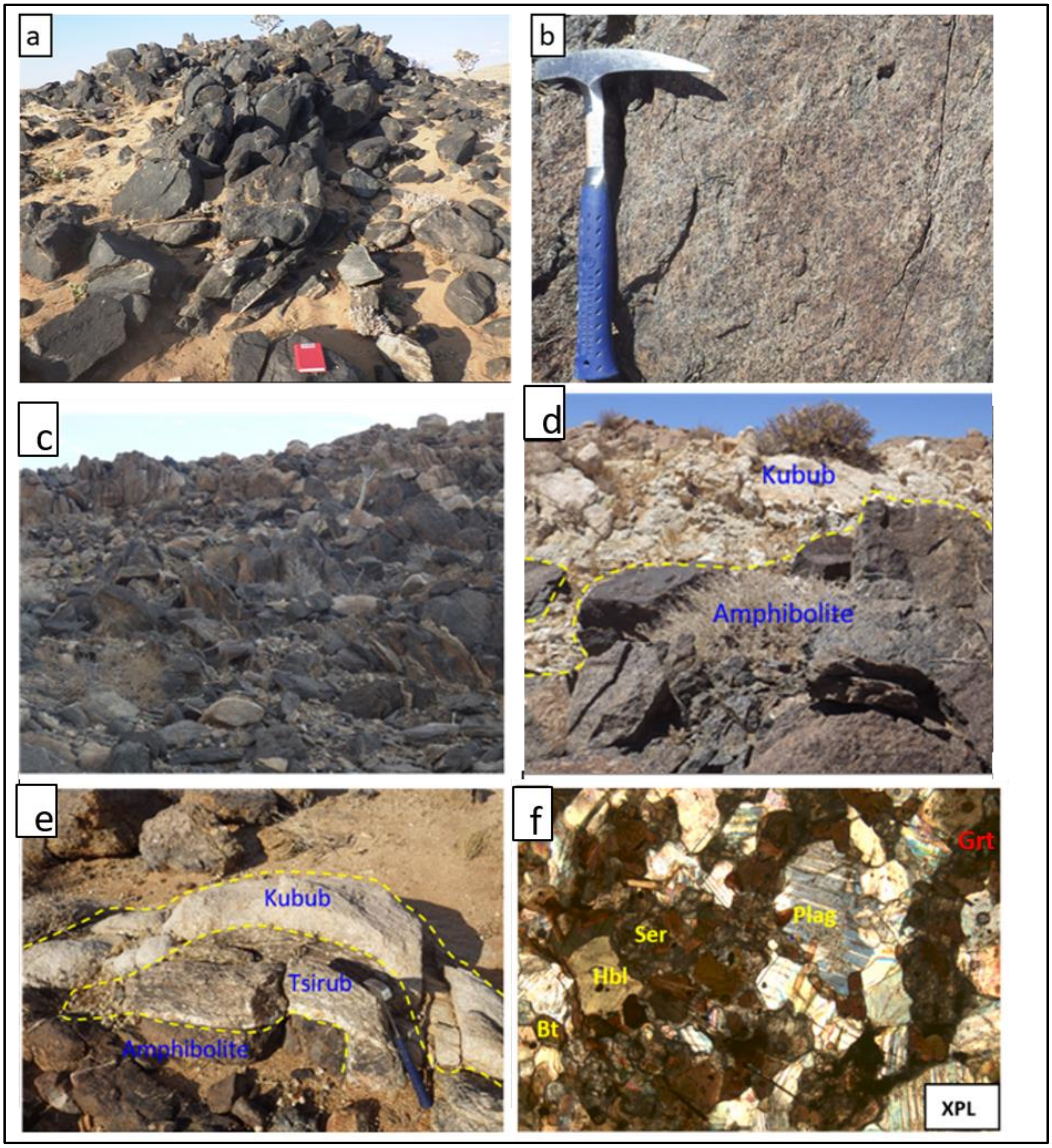

Figure 4. 4: a) Garnet amphibolite at an outcrop scale (Waypoint CM19083); b) melanocratic medium-grained garnet amphibolite (CM19112); c)heterogeneous sequence of garnet amphibolites with metapelites, calc-silicate and pegmatite (Waypoint CM19112) d) garnet amphibolite intruded by Kubub granite gneiss and e) Tsirub augen gneiss and Kubub granite gneiss intruding the garnet amphibolites (CM19014). e) Photomicrograph (FOV = 4.5mm) of amphibolite chiefly composed of plagioclase (Plag) and hornblende (Hbl). Bt: biotite, Ser: sericite, Grt: garnet, FOV= Field of view. XPL= Cross polarised light.

4.2.1.5. Mafic granulite (too small to map at 1: 50 000)

This rock crops out mostly as interlayered units with the dominant garnet biotite gneiss in the north-eastern part of the study area (Figure 4.5a). Occurrences of this rock type are too small to be represented on a map of 1: 50 000 scale, but as their granulitic mineralogy reflects an important phase of mafic intrusion prior to Namaqua metamorphism, it will be described here. The outcrop is homogenous and subrounded, in accordance with an igneous origin, but no intrusive contacts with other Garub rocks are exposed.

The mafic granulite is a massive melanocratic fine- to medium-grained rock that consists of orthopyroxene, plagioclase, hornblende, diopside, with accessories of biotite and quartz (Figure 4.5b). The mineral assemblage displays granulite facies. At parts, the mafic granulite exhibits compositional bands, while mineral foliations and lineations are weakly developed (Figure 4.5c). Individual compositional bands are generally equigranular.

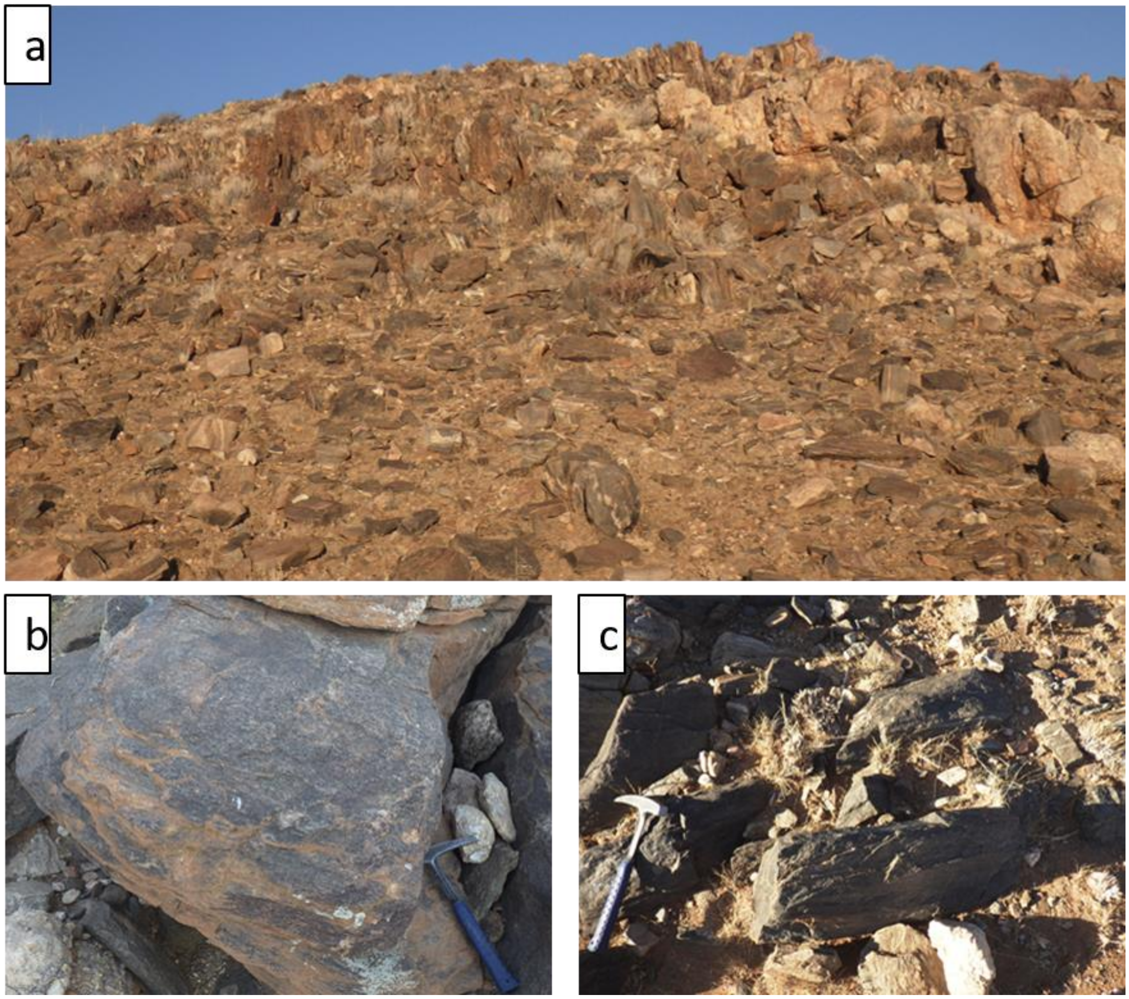

Figure 4. 5: a) outcrop of granulite intruded by pegmatites (Waypoint CM19014); b) melanocratic mafic granulite (CM19014) and c) deformed mafic granulite with bands (Waypoint CM19014).

4.2.1.6. K-feldspar plagioclase epidote rock (MGBqf)

The homogenous pale pink K-feldspar plagioclase epidote rock crops out mostly in the centre of the study area, just north of Aus (Figure 4.6a, b). The K-feldspar plagioclase epidote rock is generally interlayered with garnet amphibolites and marbles, hence included in the Garub Group. Although occurring in the high-grade domain around Aus, their mineralogy is not diagnostic of the grade; they are closely associated with epidote schists (Figure 4.6c). A set of epidote-bearing veins occur as a late hydrothermal event that affected the rock units in the area. In most outcrops, the K-feldspar plagioclase epidote rock exhibits a weakly developed fabric and is highly fractured (Figure 4.6d). Layering and compositional banding are essentially absent. K-feldspar plagioclase epidote rock is exposed as widespread mappable unit and highly metasomatized. In places, pegmatitic fractions of this rock have intruded the surrounding rocks; the mineral interaction is either part of the syntectonic migmatization or part of the largely post-tectonic phase of intrusion of the K-feldspar rich pink pegmatites.

In the thin section, the K-feldspar plagioclase epidote rock is medium to coarse-grained composed of quartz (40%), K-feldspar (25%), plagioclase (15%), epidote (10%) and minor amounts of garnet (3%), chlorite (3%)and biotite (4%; Figures 4.6e). The distinctive pale pink colour is due to the presence of pink microcline, which is highly altered to sericite. Quartz crystals show variations in size from fine to medium grained and subhedral grains. Biotite is subhedral with pleochroism of tint brown to colourless with a random distribution. The mineral assemblage of K-feldspar plagioclase epidote rock is garnet + K-feldspar + plagioclase + quartz + biotite + epidote + chlorite. The presence of chlorite represents retrograde metamorphism at a lower greenschist facies.

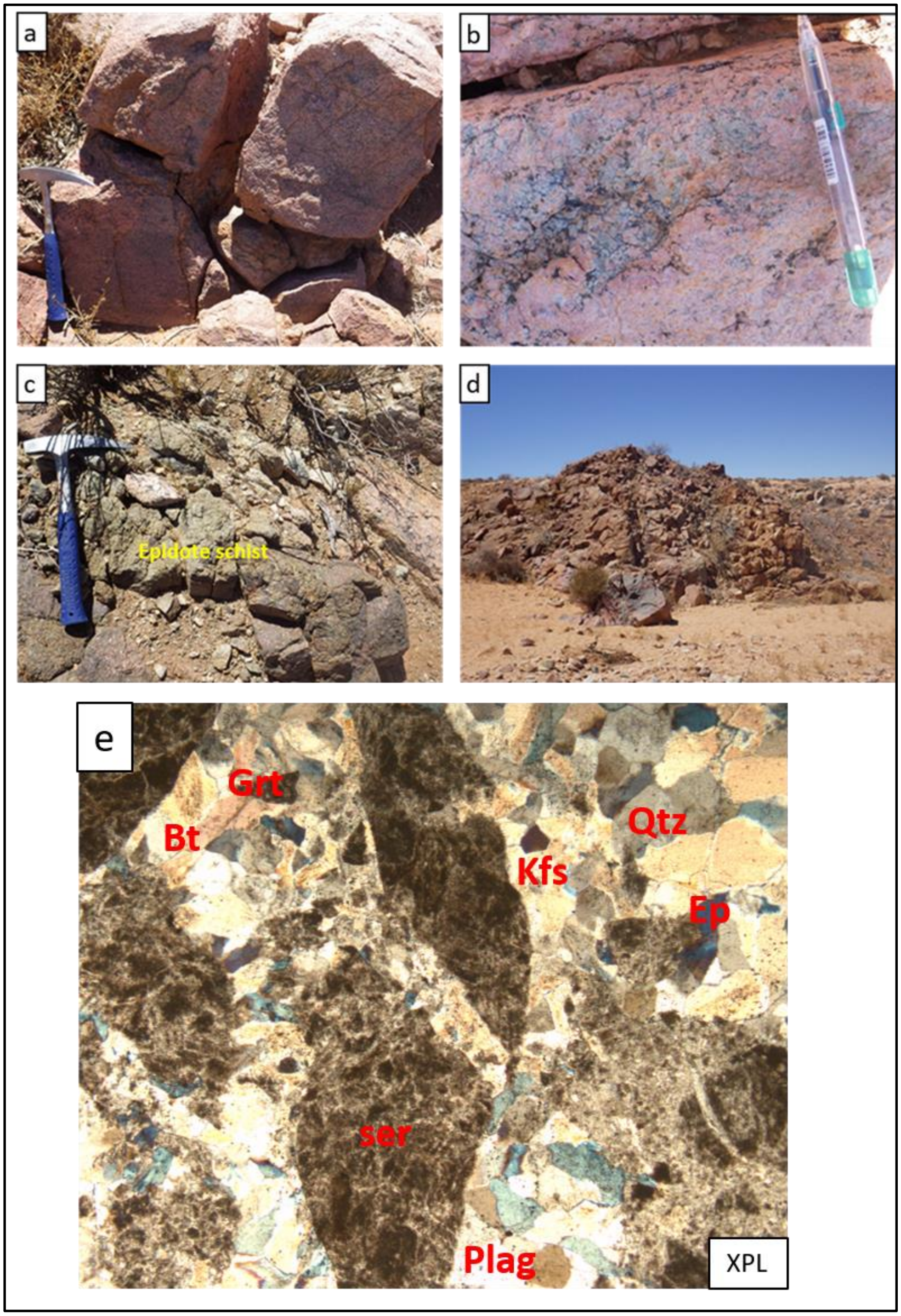

Figure 4. 6: a) Leucocratic pale pink medium-grained K-feldspar plagioclase epidote rock (Waypoint CM19131); b) close-up of the K-feldspar plagioclase epidote rock (CM19137); c) epidote schists and epidotised veins with K-feldspar plagioclase epidote rock , d) highly fractured pink quartz feldspar outcrop (Waypoint CM19131) and e) Photomicrograph (FOV = 4.5mm) of a K-feldspar plagioclase epidote rock highly sericitised.Bt: biotite, Grt: garnet, Kfs: K-feldspar, Qtz: quartz, Ep: epidote, Ser: sericite, Plag: plagioclase, FOV= Field of view. XPL= Cross polarised light.

4.2.1.7. Serpentinite (MseNQ)

This rock type is very rare in the study area, but occurs as a thin but significant unit north of Aus (Figure 4.7a). This is a NW-trending ovoid body of red-brown to black, biotite-bearing serpentinite 1000 m by 400 m in size. The melanocratic coarse grained serpentinite occurs as a thin unit consist mostly of biotite (Figure 4.7b) and is associated with garnet biotite gneiss (Figures 4.7c and d). No concentrations of chromite, magnetite or sulphides were found.

Most of the serpentinites in the area show no penetrative linear or planar fabric; which shows that they have reacted incompetently during deformation. The unit has a strongly foliated margin with a lineation parallel to the lineation in the enclosing garnet biotite quartz gneiss; however, this foliation does not persist inwards. The serpentinite is flanked on three sides by Garub metasedimentary rocks and garnet biotite quartz gneiss; the strike of the layered rocks is roughly parallel to the contact with the enclosed body, which occupies the core of a large early isoclinal fold and has somehow controlled the pattern of deformation around it.

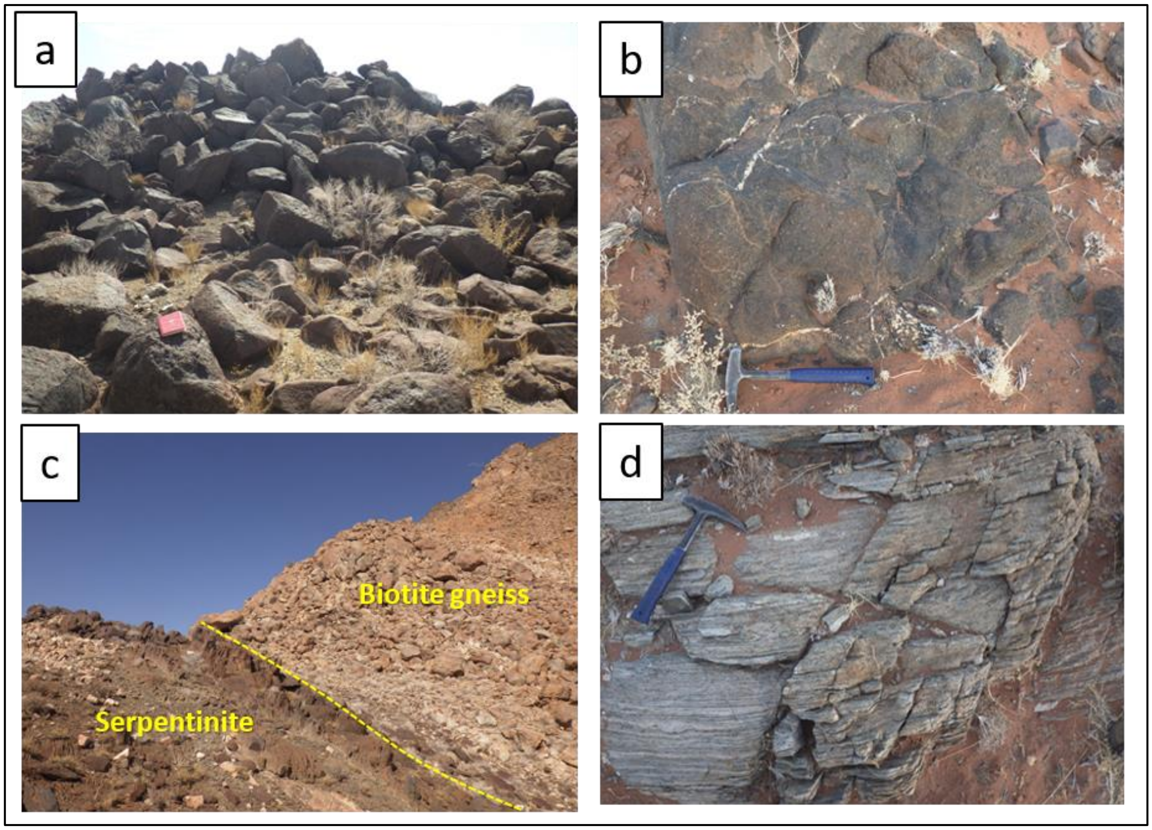

Figure 4. 7: a) outcrop of serpentinite rock unit (Waypoint CM19005); b) melanocratic coarse-grained serpentinite (CM19005); c) garnet biotite gneiss in contact with serpentinite (Waypoint CM19005) and d) close-up of garnet biotite gneiss (Waypoint CM19005).

4.2.2. Intrusive rocks

4.2.2.1. Garnet Biotite Augen Gneiss/Tsirub Augen Gneiss (MgTr)

This rock crops out mostly in the north-west part of the study area and it is well exposed (Figure 4.7a). The unit is poorly exposed in the southern part of the study area. Garnet biotite augen gneiss is also called Tsirub augen gneiss after the farm in Aus where it is best exposed. Tsirub augen gneiss is a melanocratic homogeneous megacrystic with a granodioritic composition and augen texture (Figure 4.8b). The augen consists of deformed, tabular plagioclase phenocrysts with pressure shadows and tails of quartz aggregates (Figure 4.8c). The shape of augen is controlled by the degree of deformation, which results in a progressive flattening and elongation of the augen, or by the degree of in situ partial melting which results in augen tails. The Tsirub augen gneiss is characterized by a strong planar fabric defined by biotite and the long axes of the augen (Figure 4.8d). At parts, the augens are greatly elongated which results to a banded appearance. High strain localities show sheared augens within the rock and the shear indicators demonstrate dextral shearing (Figure 5.8c).

Tsirub augen gneiss intrudes the Garub rocks, and xenoliths of the latter occur in the gneiss (Figure 4.8d). At parts, Tsirub augen gneisses are overlain by Garub Group, as in the northern part of the study area (Figure 4.8e) which may imply the existence of a thrust; but in many other places the Tsirub augen gneiss intrudes the Garub Group. Contacts between the Tsirub augen gneiss and Garub group rocks are concordant and parallel to the layering in the Garub rocks and the foliation in the gneiss.

In the thin section, Tsirub augen gneiss is medium grained composed of quartz (35%), plagioclase (25%), hornblende (15%), garnets (15%) and biotite (10%) with equigranular texture (Figure 4.8f). Quartz is recrystallized with sutured grain boundaries. Two types of garnets are found, one comprising anhedral porphyroblasts with inclusions and embayed margins, the other consisting of smaller euhedral crystals with smooth margins and no inclusions. These textures imply that there are different generations of garnets present, and two metamorphic events are recorded in this rock; one superimposed the other. In the matrix, plagioclase forms equant polygonal grains closely associated with biotite, and the plagioclase crystals are altered to sericite. The mineral assemblage of Tsirub augen gneiss is garnet + K-feldspar + plagioclase + hornblende + biotite + quartz.

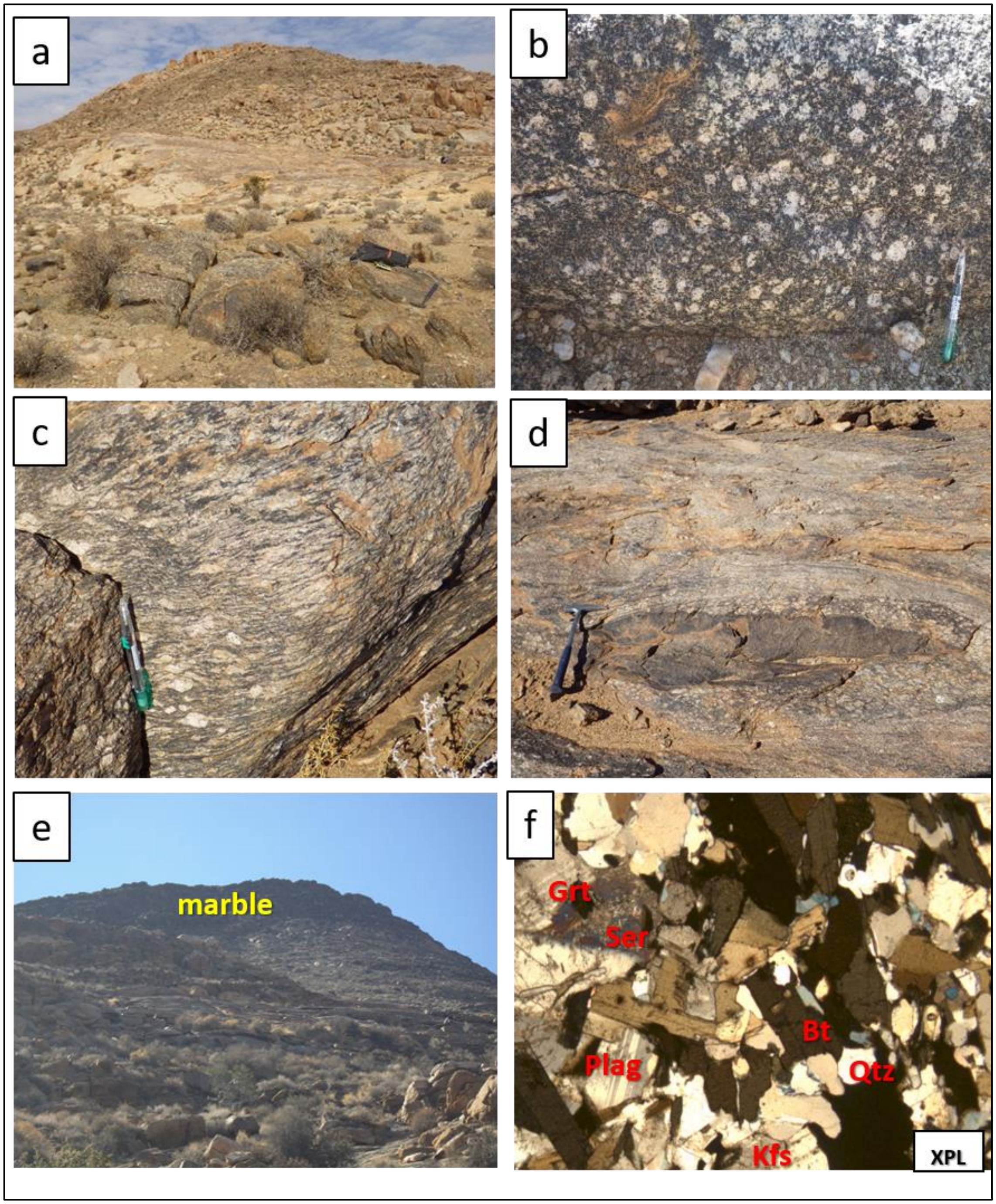

Figure 4. 8: a) Panorama of well exposed hill outcrop of Tsirub augen gneiss (Waypoint CM19003); b) homogeneous coarse grained, megacrystic tonalitic to granodioritic gneiss (C19004); c) outcrop with large plagioclase phenocrysts forming augen-gneiss texture; d) xenolith of Garup rock within Tsirub augen gneiss (Waypoint CM19099); e) Tsirub augen gneiss overlain by marble (Waypoint CM19027) and f) Photomicrograph (FOV = 4.5mm) exhibiting the equigranular texture; plagioclase (Plg) being altered to sericite (Ser), quartz (Qtz) occur as small sub-hedral grains. Grnt; garnet, Bt: biotite, Kfs: K-feldspar, FOV= Field of view. XPL= Cross polarised light.

4.2.2.2. Megacystic K-feldspar- Biotite-Garnet Granite Gneiss/ Aus Granite Gneiss (MgAs)

The generally well exposed leucocratic megacystic K-feldspar- biotite-garnet granite gneiss also known as Aus granite gneiss, crops out in the entire study area, and forms mostly domed inselbergs north of Aus (Figure 4.9a). It is the dominant rock type within the Aus townlands, after which it has been named.

The unit is strongly deformed and exhibits a magmatic foliation defined by the orientation of the feldspar laths (Figure 4.9b). However, in other outcrops metamorphic foliation is prominent as defined by the preferred orientation of biotite.

The Aus granite gneiss contains numerous inclusions of older rocks in the hills north of Aus; contacts are sharp but not chilled (Figure 4.9c). In the northwestern part of Aus Townlands, xenoliths of Tsirub augen gneiss are observed within Aus granite gneiss (Figure 4.9d and e). Locally, the fabric in the Tsirub augen gneiss is refoliated into parallelism with the contact to the Aus granite gneiss. Aus granite gneiss has gradational contacts to the Garub units and Kubub granite gneiss.

In the thin section, Aus granite gneiss is coarse-grained comprised of K-feldspar (40%), quartz (30%), Plagioclase (20%), garnet (20%) and biotite (10%) with inequigranular texture (Figure 4.9f). The size of the K-feldspar crystals varies from 3 cm to 5 cm in length and twinned, while plagioclase is intensively altered to sericite. Quartz is anhedral and occurs as inclusions within the K-feldspar. Garnet occurs as coarse, subhedral with a porphyroblast texture. The grains are partially rimmed by subhedral quartz intergrowths associated with microcline.

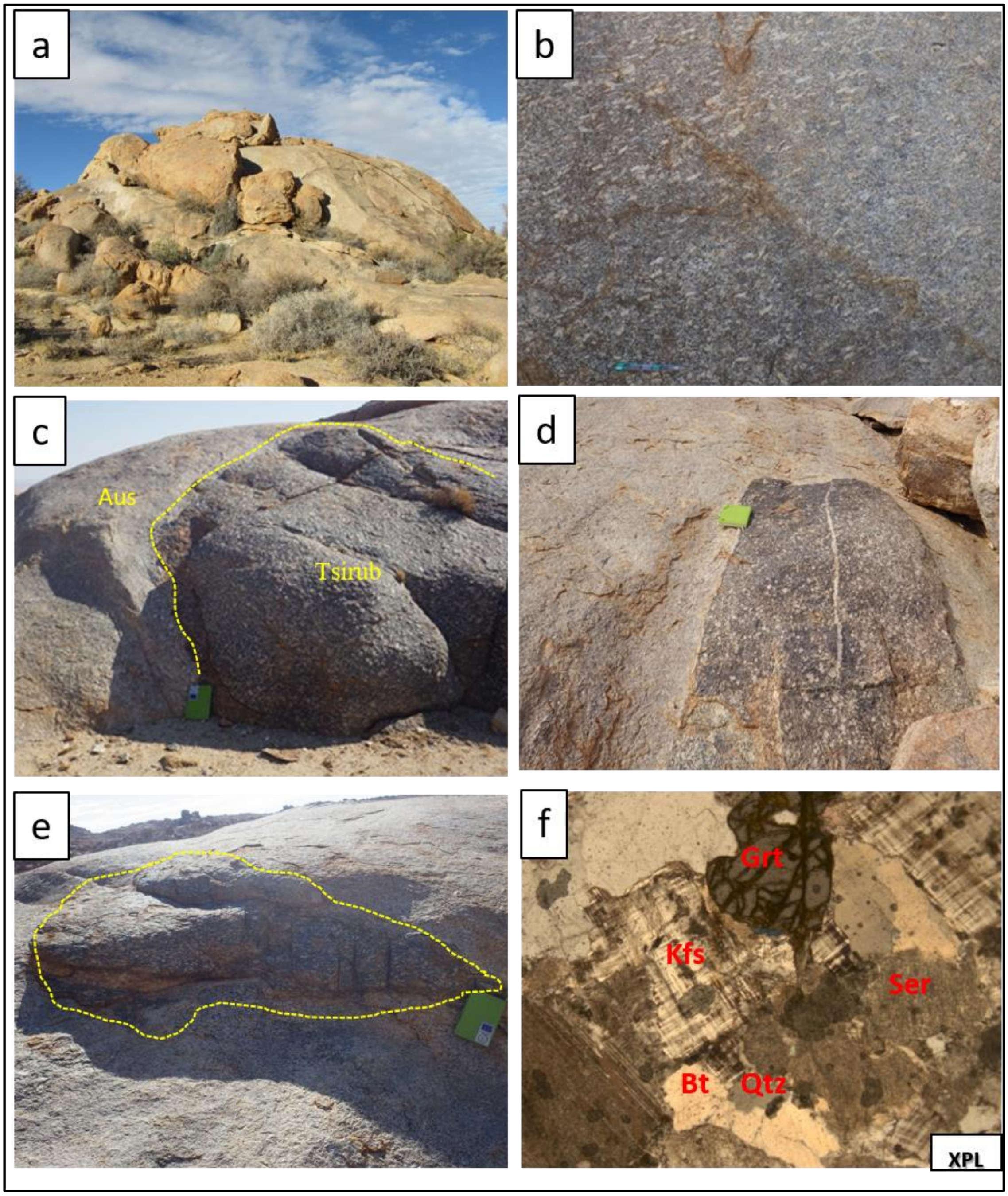

Figure 4. 9: a) Domed inselberg of Aus granite gneiss; b) coarse-grained megacrystic Aus granite gneiss; c) d), e) contact relationship between Aus granite gneiss and Tsirub augen gneiss (Tsirub xenoliths within Aus granite gneiss) (Waypoints CM19019, CM19030 and CM19019 respectively) and f) Photomicrograph (FOV = 4.5mm) exhibiting medium to coarse grained composition dominated by K-feldspar (Kfs) with plagioclase altered to sericite (Ser); Bt: biotite, Grt: garnet, FOV= Field of view. XPL= Cross polarised light.

The megacrysts are largely randomly oriented while biotite defines a weak foliation. The megacrysts are partially recrystallised with sutured subgrain boundaries. K-feldspar is partially sericitized and biotite is altered to chlorite. The overall mineral assemblage for this rock is garnet + K-feldspar + plagioclase ± hornblende + quartz + biotite. Chlorite is a retrograde mineral.

4.2.2.3. Quartzo-Feldspathic Gneiss/Kubub Granite Gneiss (MgKu)

This quartzo-feldspathic gneiss also known as Kubub granite gneiss crops out mostly in the southern parts of the study area, where it is well exposed (Figure 4.10a). The rock was termed the Kubub granite gneiss after the mountains south of Aus in the western part of farm Kubub 15, where it is best exposed. The Kubub granite gneiss is homogenous on a regional scale, but at outcrop scale, it exhibits leucocratic pegmatitic and gneissic heterogeneous rock units (Figure 4.10b). It is characterized by two varieties: the gneissic variety predominates in the Aus area whereas the pegmatitic variety is more ubiquitous in the eastern part of Farm Kubub. The two varieties are intimately related with one another and contacts between the two are gradational. The gneissic variety exhibits an orange-brown colour when weathered, but appears to be pale grey to grey when fresh (Figure 4.10c). Biotite occurs as an accessory mineral, and where it is concentrated as schlieren, a strong foliation is present (Figure 4.10d). In most outcrops, the gneissic type is generally deformed and in parts strongly fractured (Figure 4.10e and f). The pegmatitic type is generally not deformed, and in most cases can be confused with other pegmatites occurring in the study area (Figure 4.10g). The Kubub granite gneiss intrudes the Garub rocks and the Tsirub augen gneiss (Figure 4.10h).

In the thin sections, the two varieties are: i) medium- to coarse-grained rock that consists of quartz (40-45%), K-feldspar (30-40%), garnet (5-10%) and biotite (10 to 15%; Figure 4.10i) with a gneissic texture and ii) a leucocratic (locally whitish), very coarse-grained pegmatitic rock made up mostly of quartz (40%) and feldspar (40%), with minor garnet (10%; Figure 4.10j). The pegmatitic type will be discussed thoroughly in chapter 4.2.2.5. The following photomicrograph description is only applicable to the Kubub granite gneiss with a gneissic texture. Microcline is abundant and forms large, deformed phenocrysts, probably enlarged by blastesis as they contain small rounded and hexagonal grains of quartz. The appearance of the garnets is generally patchy, but they are porphyroblastic at parts. Garnet is colourless in thin section and both garnet and biotite are chloritized in places. The overall mineral assemblage is garnet + K-feldspar + quartz + biotite.

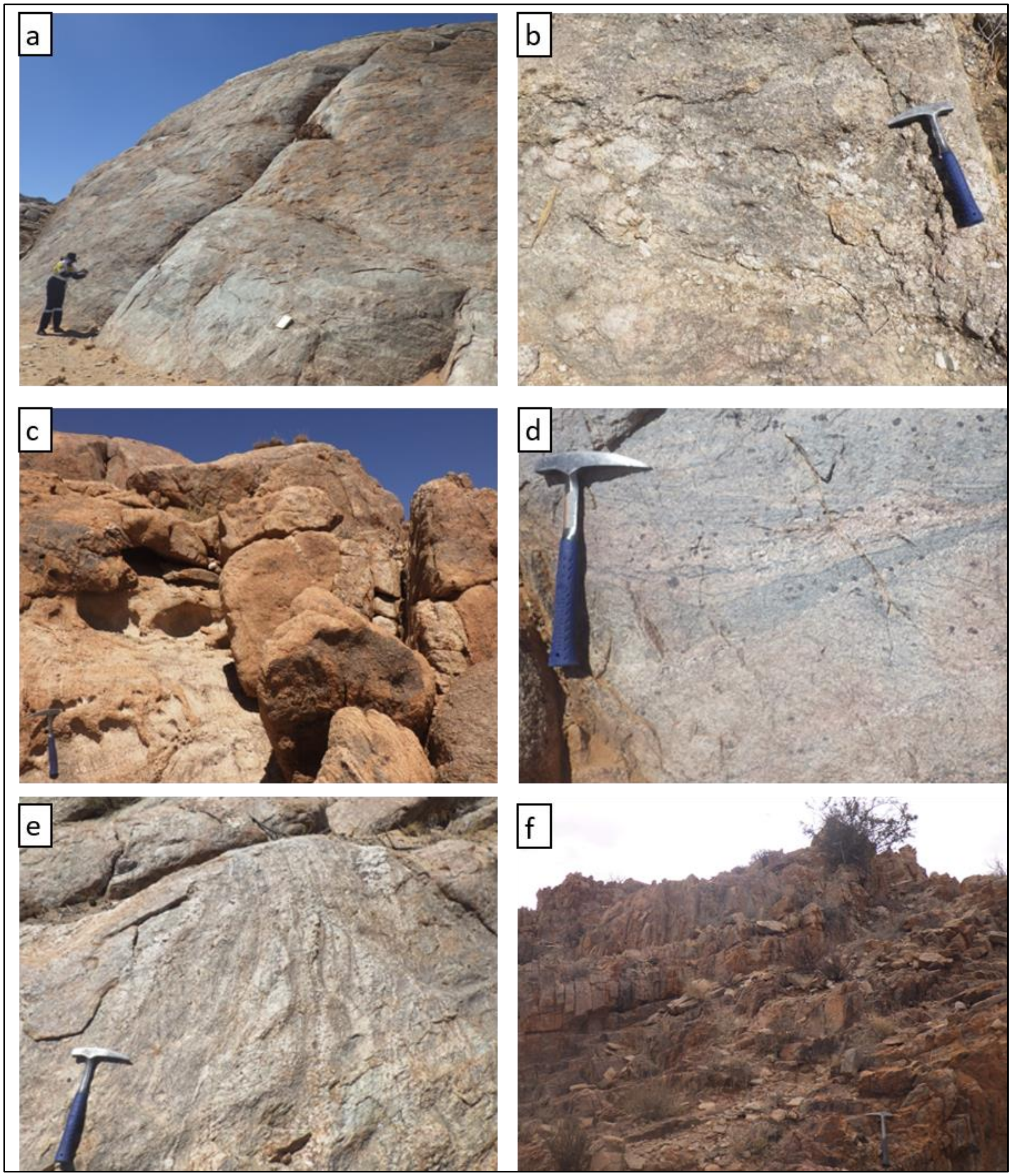
a
b
c
d
e
f

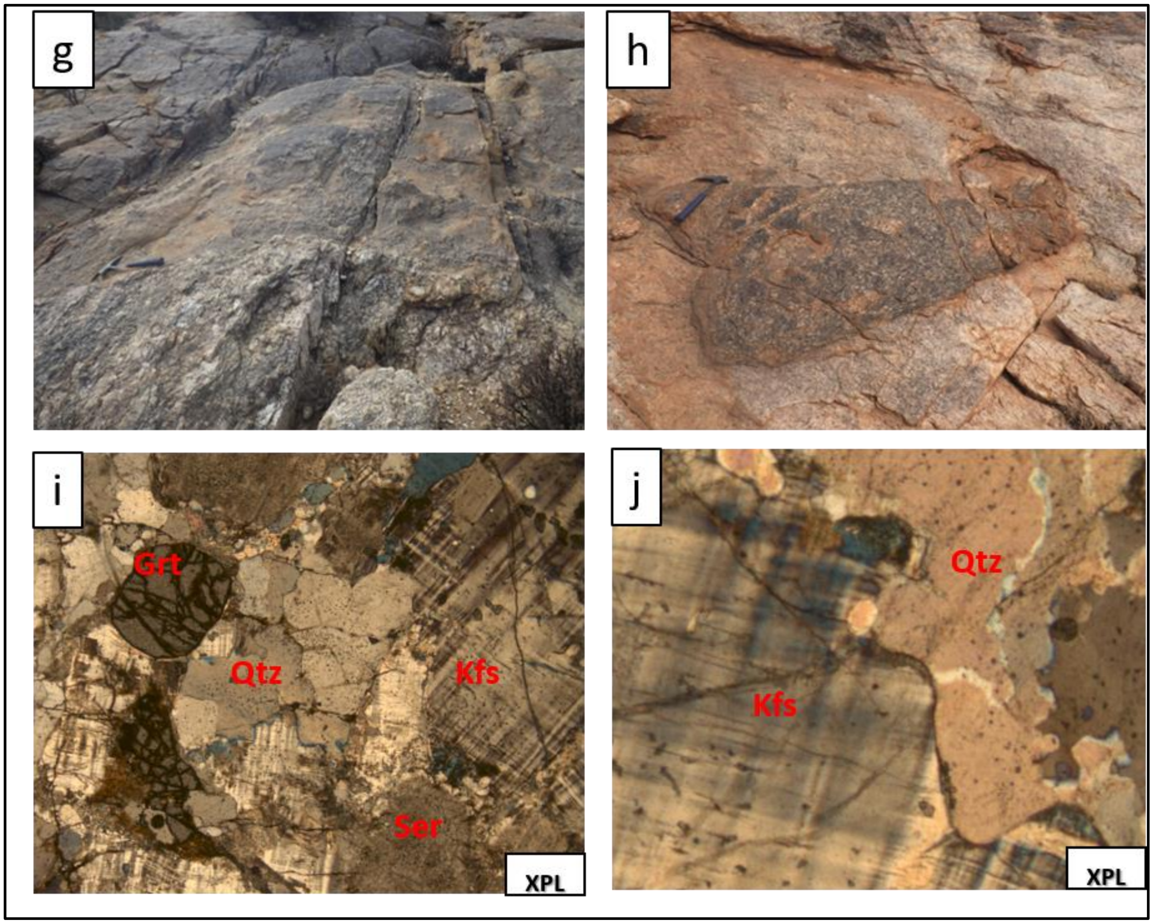

Figure 4. 10: a) Medium to coarse-grained Kubub granite gneiss (Waypoint CM19111); b) very coarse-grained pegmatitic rock; c) orange brown weathering in the gneiss (Waypoint CM19129); d) patchy garnets and schlieren texture (Waypoint CM19111); e) migmatitic texture within Kubub granite gneiss; f) highly fractured gneiss (Waypoint CM19129); g) pegmatite intruding Garub rocks, Tsirub, Aus); h) xenolith of garnet biotite gneiss within Kubub granite gneiss, i) Photomicrograph (FOV = 4.5mm) exhibiting coarse grained Kubub type 1 and j) Photomicrograph (FOV = 4.5mm) of a very coarse grained Kubub type 2. Grnt: garnet, Qtz: quartz, Kfs: K-feldspar, ser: sericite, FOV= Field of view, XPL= Cross polarised light.

4.2.2.4. Warmbad Granite (too small to map at 1: 50 000)

This rock intrudes mostly the Kubub granite gneiss in the southern part of the study area (Figure 4.11a). Occurrences of this rock type are too small to be represented on a map of 1: 50 000 scale. It is a weakly foliated, pinkish-brown weathering, medium-grained equigranular granite.

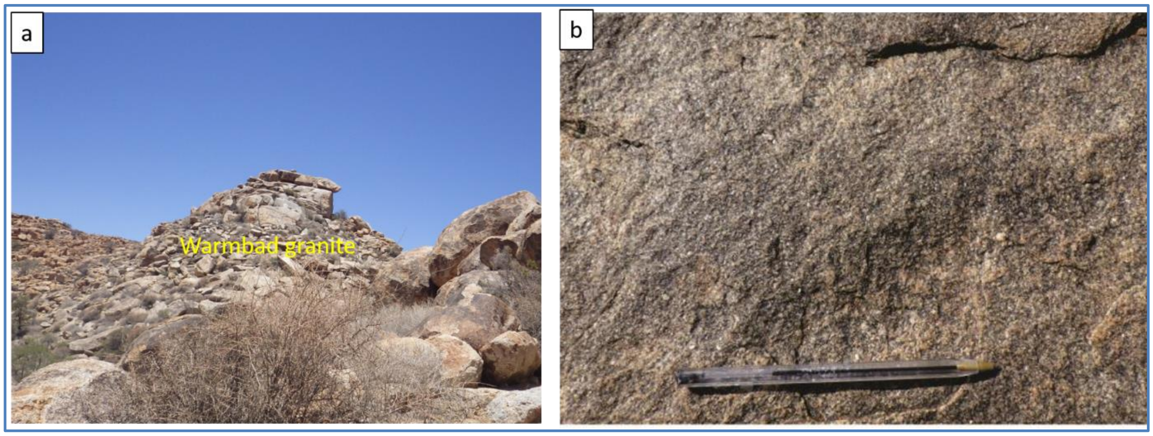

Figure 4. 11: a) A small outcrop of warmbad granite b) weakly-foliated leucocratic Warmbad granite.

4.2.2.5. Pegmatites (Mpe)

Pegmatite sills and dykes extensively intruded rocks in the southern part of the study area and in the central area of the map. However, there is a thick unit in the upper northern part of the geological map that was mapped out as a polygon because it is laterally continuous and 5 to 100 m wide. In the field, pegmatites occur as concordant sheets within the foliation of the adjacent rocks and as discordant units cross-cutting older rocks. The pegmatites are typically very coarse grained (>20 mm grain size) and composed of K-feldspar, plagioclase, quartz, biotite, muscovite and minor tourmaline. No foliation or other structure could be recognized within these rocks.

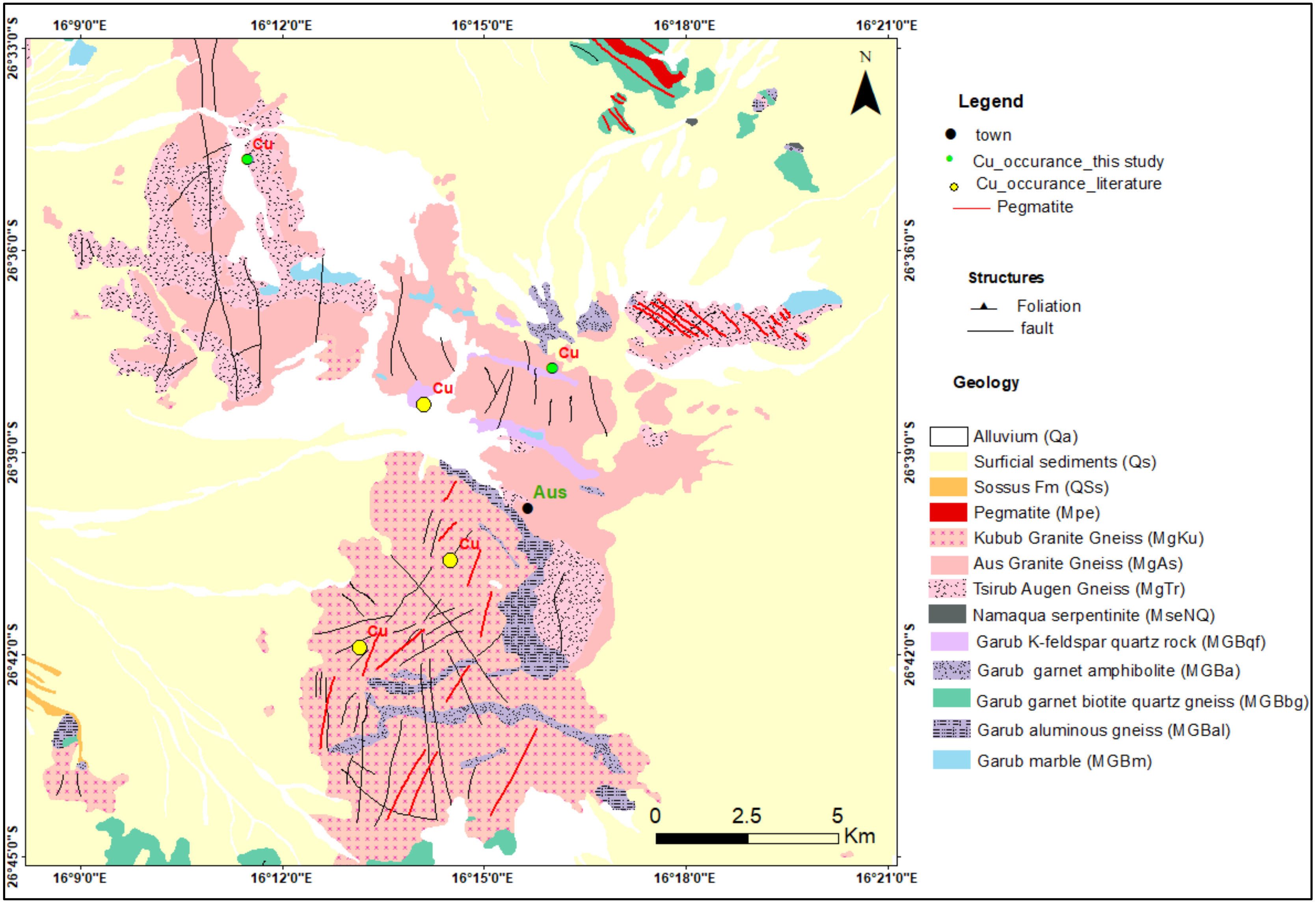

Figure 4. 12: Geological Map of the study area showing localities of copper occurrences.

4.3. Structural framework of the Aus Domain from satellite and field mapping

This section gives a description of the nature and geometry of the major deformation fabrics and structures observed, and their relationship to the copper mineralization found in the study area. The lineaments were mapped out using sentinel and were used as an aid in the field to locate them (Figure 4.12).

In the study area, foliation is commonly parallel to the contacts of the surrounding rock units. The foliations in the northern part of the study area are dominantly striking NE-SW, whereas central and southern of the area the foliation strikes NW-SE (Figure 4.13). Foliation within most of the rock units in the study area is defined by the preferred orientation of biotite flakes while in the Aus granite gneiss is characterized by the alignment of K-feldspar megacrysts. The lineations are well developed at places and are defined by the preferred mineral alignment such as sillimanite and cordierite in metapelitic rocks, aligned biotite and hornblende in mafic granulites and preferred orientation of tabular megacrysts of K-feldspar and garnet trains in the granite gneisses.

The folds are mainly found in migmatized Garub garnet biotite gneiss and aluminous gneiss. The style of these folds is variable. Rock units at the bottom of the sequence have rounded hinge zones, while the upper sequence have sharply curved hinge zones. Small scale Parasitic folds are present commonly in the north of Aus. Dextral shearing of augens in the Tsirub augen gneiss is evidence for a shear zone system in the study area in addition to the east-west trending shear zones. Fault structures are prominent in the area striking in two major directions N-S and NW-SE (Figure 4.14). Structural measurements are presented in APPENDIX B. Geometrical observations of the major structures are presented with the aid of lower-hemisphere, equal area stereonets in Figure 4.13 and 4.14.

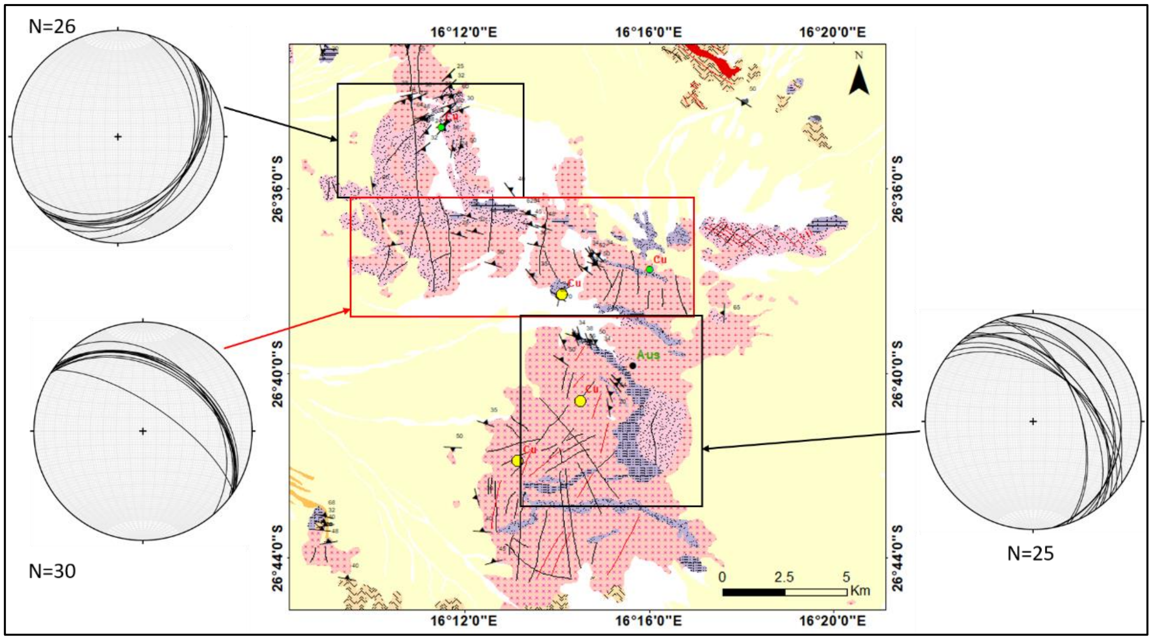

Figure 4. 13: Geological map of the study area (legend as of Figure 4.11), showing geometries of D2 fabric.

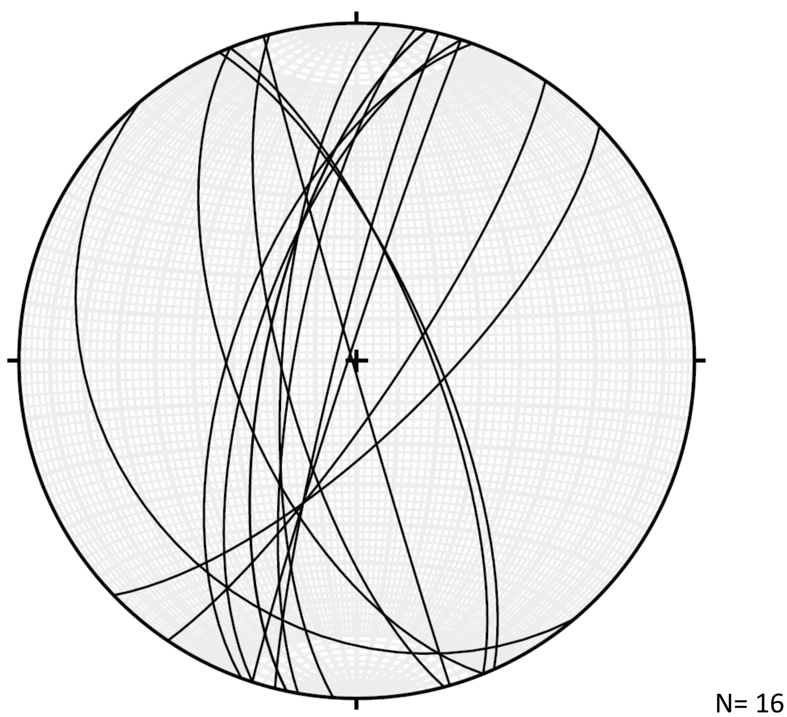

Figure 4. 14:Dominant geometries of D4 fabric.

4.4. Mineralization

Malachite is the main mineral observed on the surface. It is distributed over a strike interval of about 10 m and occurs within a thickness of up to 1.5 m. Three main forms of occurrences are distinguished: i) at the contact between Garub Group and intrusives (Figure 4.14) ii) quartz vein related (Figure 4.15) and iii) along fault planes (Figure 4.16). The contacts between Garub Group rocks and the intrusives are parallel to foliation, whereas the quartz vein related and fault planes occurrences are within the structures trending N-S direction.

Figure 4. 15: Malachite at the contact between Garub group (Amphibolite) and Tsirub augen gneiss.

Figure 4. 16: Malachite associated with quartz vein.

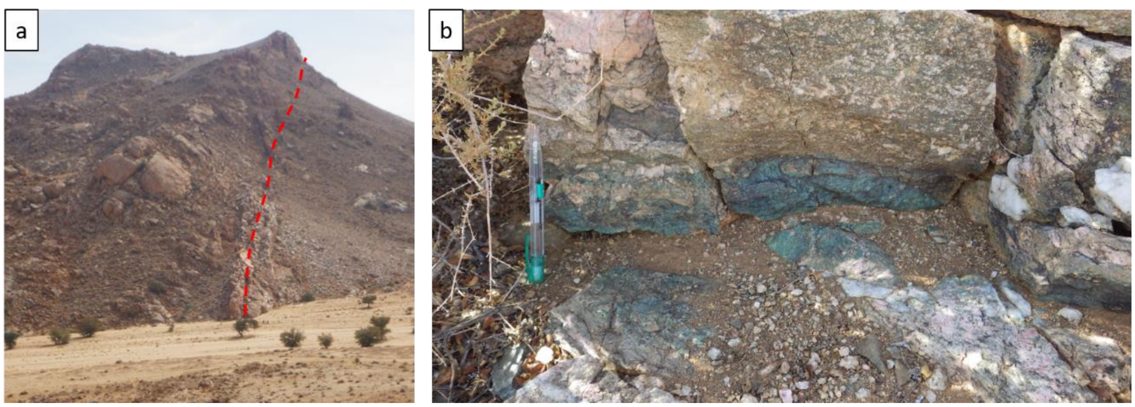

Figure 4. 17: a) Fault trending N-S (in red) b) Malachite associated with fault plane.

No malachite occurrence was observed within the pink feldspar rock, however this rock is intensively altered, fractured and associated with quartz veins.

4.4. Geochemistry of intrusive rocks in the Aus Domain

A total of eighteen representative samples were analyzed for major and trace elements including rare earth elements. Major elements were analyzed using the X-ray Fluorescence (XRF) technique and trace elements by Inductively Coupled Plasma Mass Spectrometry (ICP-MS). See Chapter 3.3.2 for details. Geochemical analysis was carried out at the University of Stellenbosch laboratories, South Africa. The analyzed samples are exclusively for the intrusive rocks (granitoids) found around the study area.

4.4.1. Geochemistry of major elements

Results of major element compositions of the eighteen samples are presented in Appendix F. Samples display trends of decreasing Al_2O_3, CaO, FeO_t, MgO, TiO_2, P_2O_5, MnO, but an increase in K_2O, Na_2O with increasing SiO_2 (Figure 4.18). Some trends are much better defined (e. g. CaO, MgO, Na_2O and P_2O) than others which seem more or less scattered (e.g K_2O and MnO). The positive trend of K_2O and Na_2O could relate to contamination of magma by silicate rocks. Cr_2O_3 is present in very insignificant amount of 0.002 – 0.01 wt.%. Similarly, samples reported very low volatile (LOI) content between 0.15 and 1.58 wt.% which implies low degree of weathering.

The major element data show that granitoids have SiO_2 contents of between 65 and 73 wt.% (mean 70 wt.%), Na_2O + K_2O between 5.5 and 9.1 wt.% (mean 7.3 wt.%) and the SiO_2/Al_2O_3 ratio varies between 3.9 and 6.4. These rocks vary in composition from granodioritic to granite and plot in a sub-alkaline field as defined by Cox et al (1979) (Figure 4.19a) on the total alkali versus silica (TAS) diagram. In the K_2O versus SiO_2 diagram (Figure 4.19b) the granitoids plot in the two fields defined as shoshonitic and high-K calc alkaline. The high content of SiO_2 in all the granitoids show that the rocks have highly fractionated.

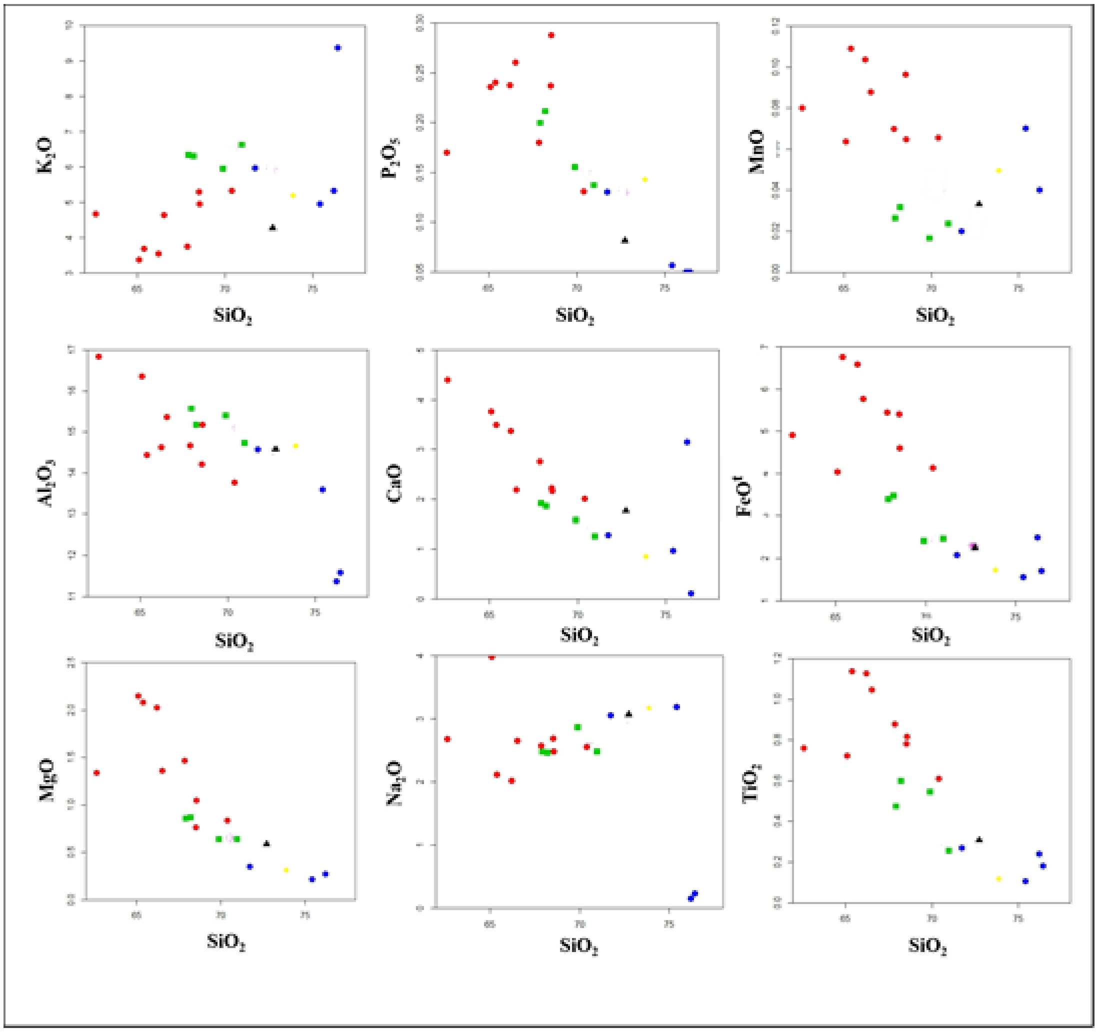

Figure 4. 18: Harker diagrams bivariate major element (in wt.%).

The granodiorite and granites display a linear trend that falls in the calc-alkaline field on the AFM diagram with high values of Na_2O and K_2O and moderate values of FeO_t and MgO. However, four samples of the Tsirub augen gneiss somehow plots at the boundary between the tholeiite and calc-alkaline series (Figure 4.19c). The samples display results of strongly peraluminous with an average Alumina Saturation Index (ASI) of 1.5 with only three samples plotting within the metaluminous field on the A/NK vs A/CNK diagram (Figure 4.19d).

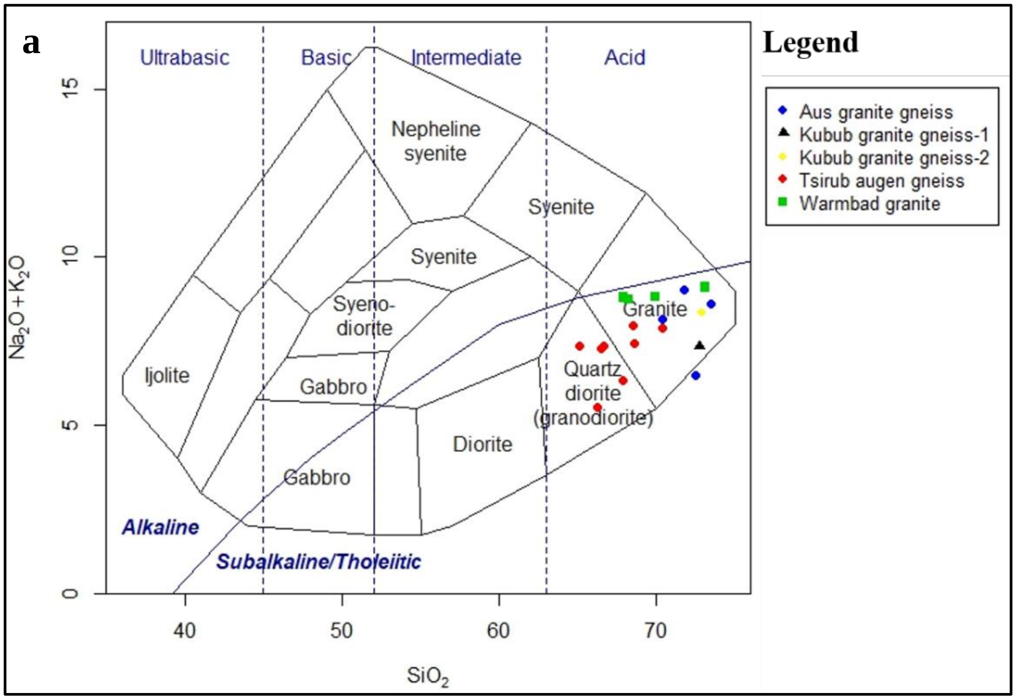

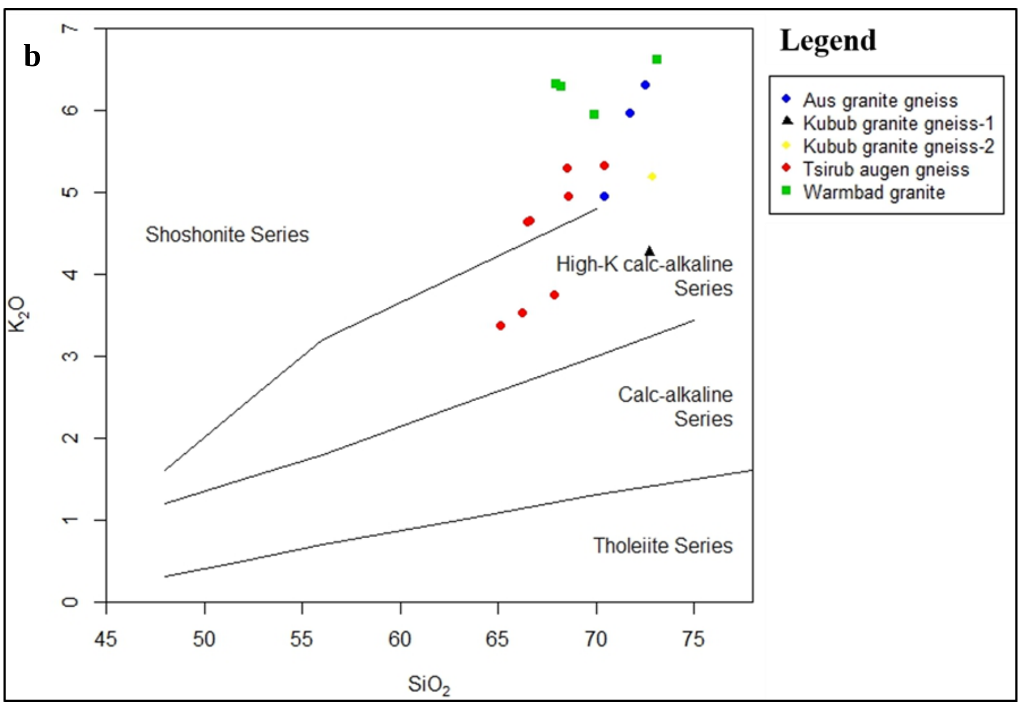

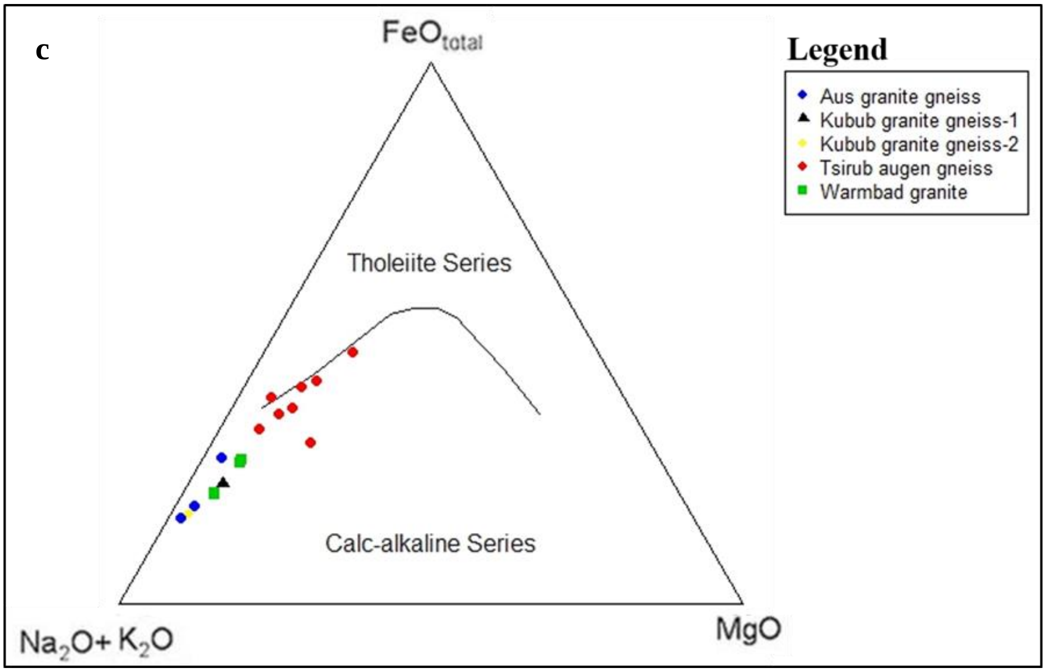

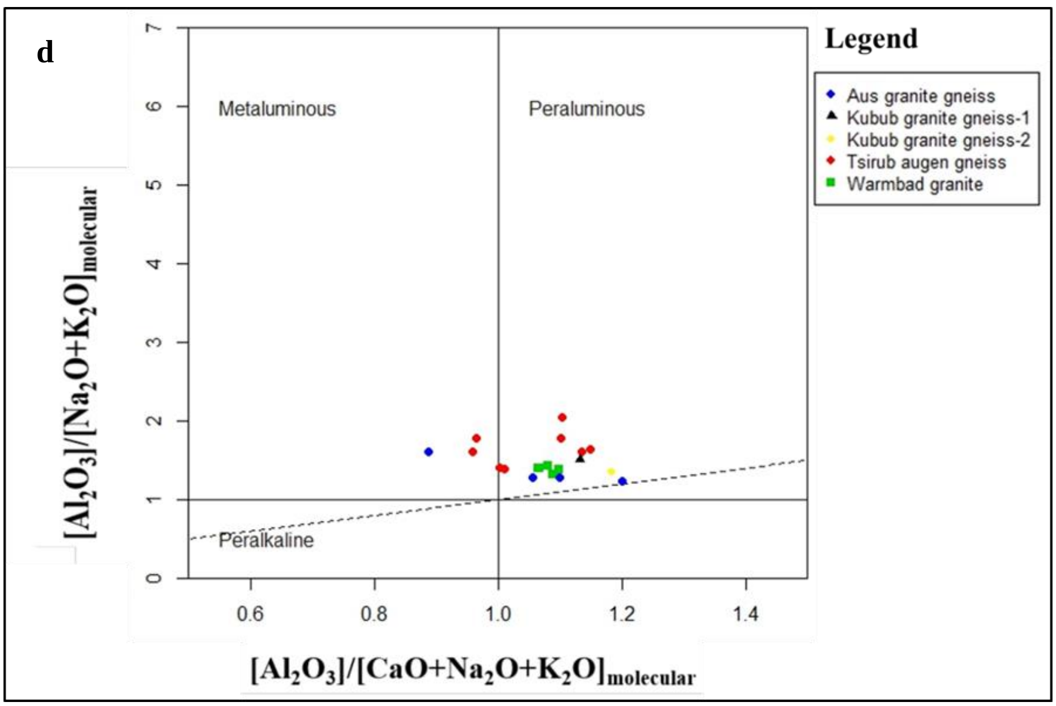

Figure 4. 19: a) TAS plutonic classification by Cox et al. 1979*; b) SiO_2-K_2O plot (Peccerillo and Taylor, 1976); c) AFM diagram (Irvine and Baragar, 1971) and d) Shand (1943) classification.*

4.4.2. Geochemistry of trace elements

Trace element results are presented in Appendix F with analysis showing high concentration values of Rb (up to 353 ppm), Sr (up to 511 ppm), Zr (up to 443 ppm), Ba (up to 1298 ppm), La (up to 216 ppm), Ce (up to 458 ppm), Nd (up to 164 ppm). V and Cu show moderate concentration values of up to 90 and 86 respectively. The rest of the trace elements report concentration values < 50 ppm.

The MORB-normalized spider diagram displays a strong depletion in Sr, P, Ti, Y and Yb and a strong enrichment in K, Rb, Th and Ce, while Ba, Ta, Nb, Hf and Sm are mildly enriched relative to the MORB (values from Pearce, 1983, Figure 4.20). The Aus and Kubub granite gneisses are the most depleted in Sr, P and Ti.

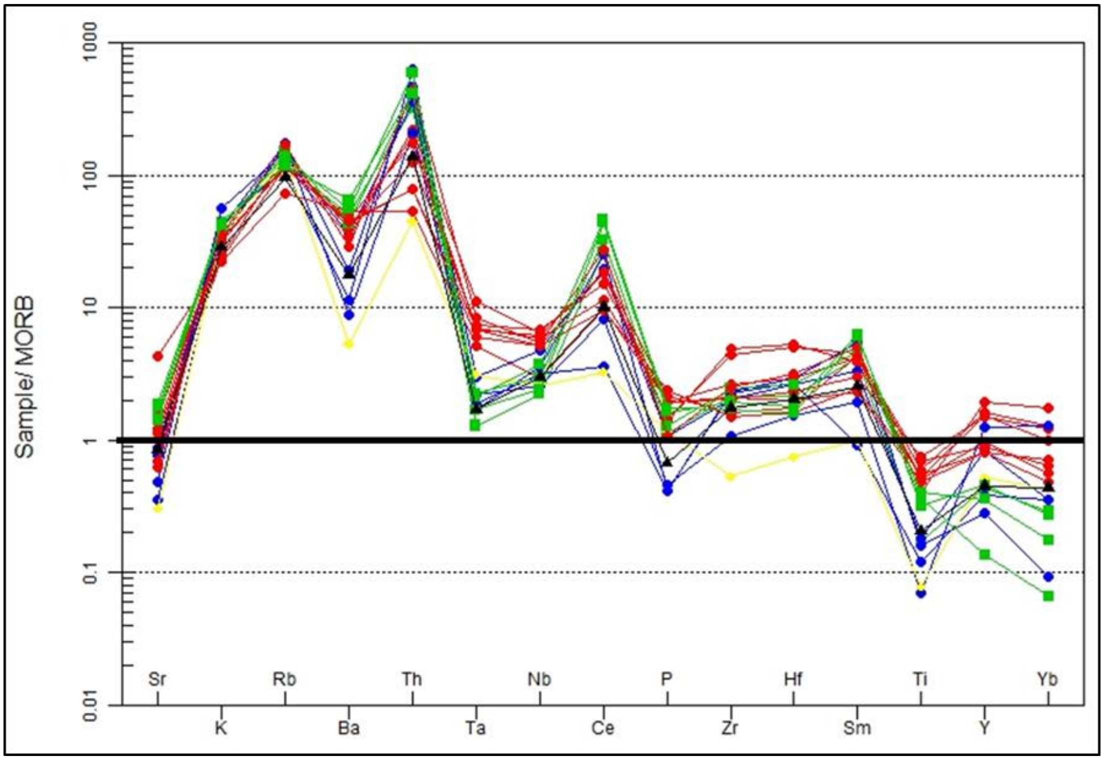

Figure 4. 20: MORB-normalised spider diagram following Pearce (1983). Symbols as for Figure 4.19.

4.4.3. Geochemistry of REE

The REE diagram exhibits enrichment of the LREE relative to the HREE with a sharp negative Eu anomaly related to plagioclase fractionation. The slope of the LREE is distinctively steeper than for the HREE, which is generally shallowly sloping. All samples are enriched in REE with relative to the Condrite (normalized values from Nakamura, 1974), expect one that is strongly depleted in Lu. A degree of fractionation in the HREE toward Lu is evident (Figure 4.21).

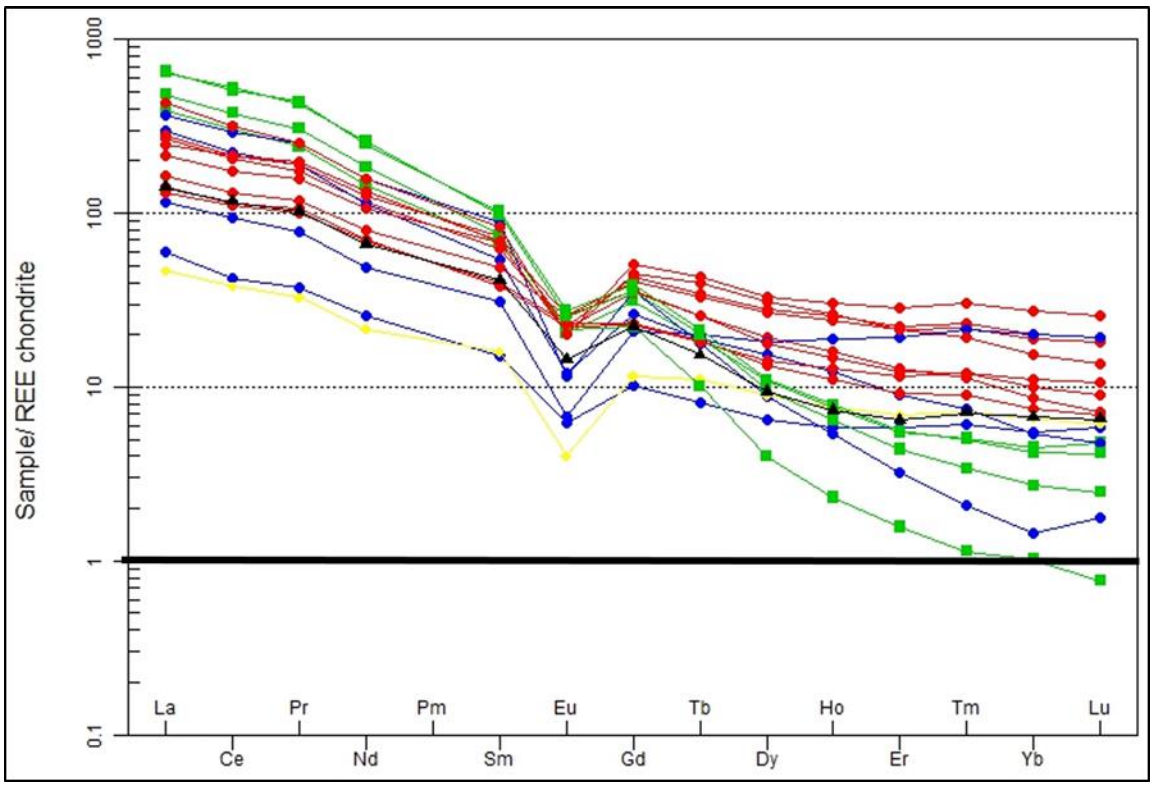

Figure 4. 21: Condrite normalized REE concentration patterns of the granitoids (normalized values from Nakamura, 1974). Symbols as for Figure 4.19.

Typically, granites are classified as either A (anorogenic), I (igneous), or S (sedimentary). Plots of Ga/Al against major element ratios and Zr, Zn, Nb, Ce and Y clearly display A-type granite on the diagram of Whalen (1987) as shown in Figure 4.22. Samples that are classified as granites in Figure 4.19a (e.g Aus granite gneiss, Kubub granite gneiss type 1, 2 and Warmbad granite) plot within the syn-collisional-Granite (syn-COLG) and Volcanic Arc Granites (VAG) whereas samples that are classified as granodiorite in Figure 4.19a (e.g Tsirub augen gneiss) plot Within Plate Granites (WPG) see Figure 4.23.

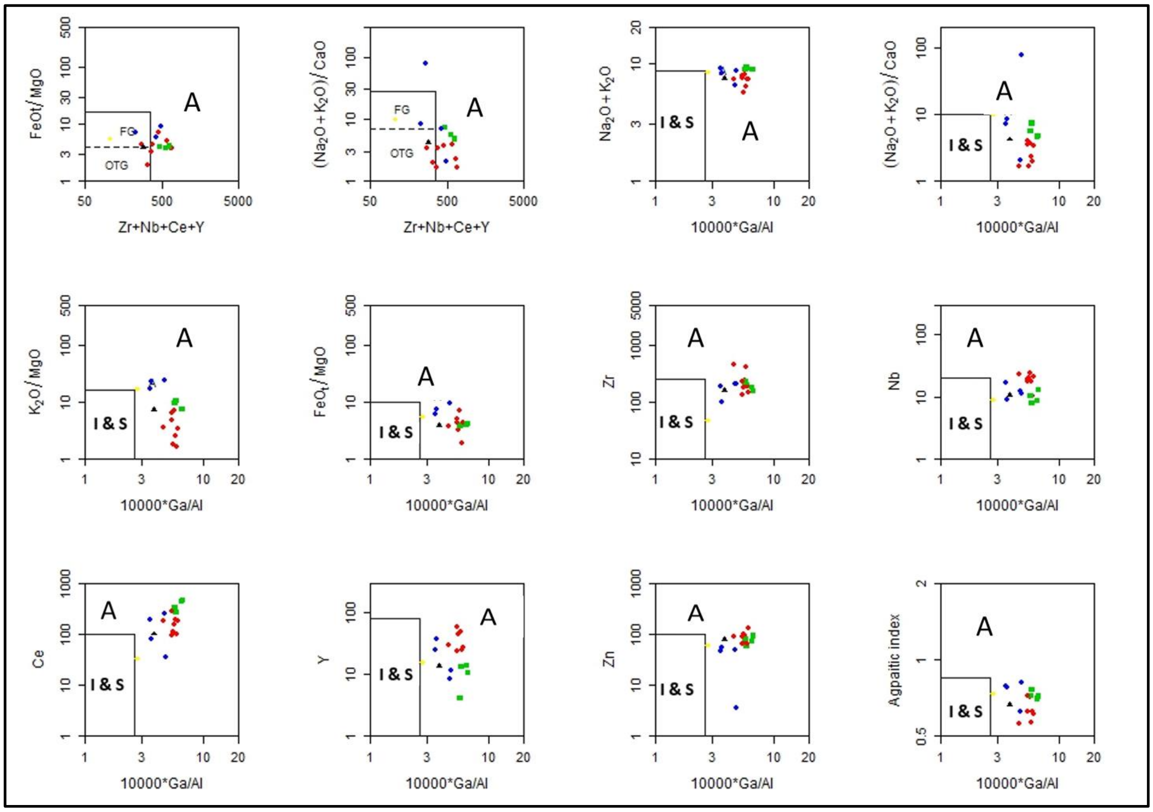

Figure 4. 22: A-S-I-type classification of the granitoids (Whalen et al., 1987). Symbols as for Figure 4.19.

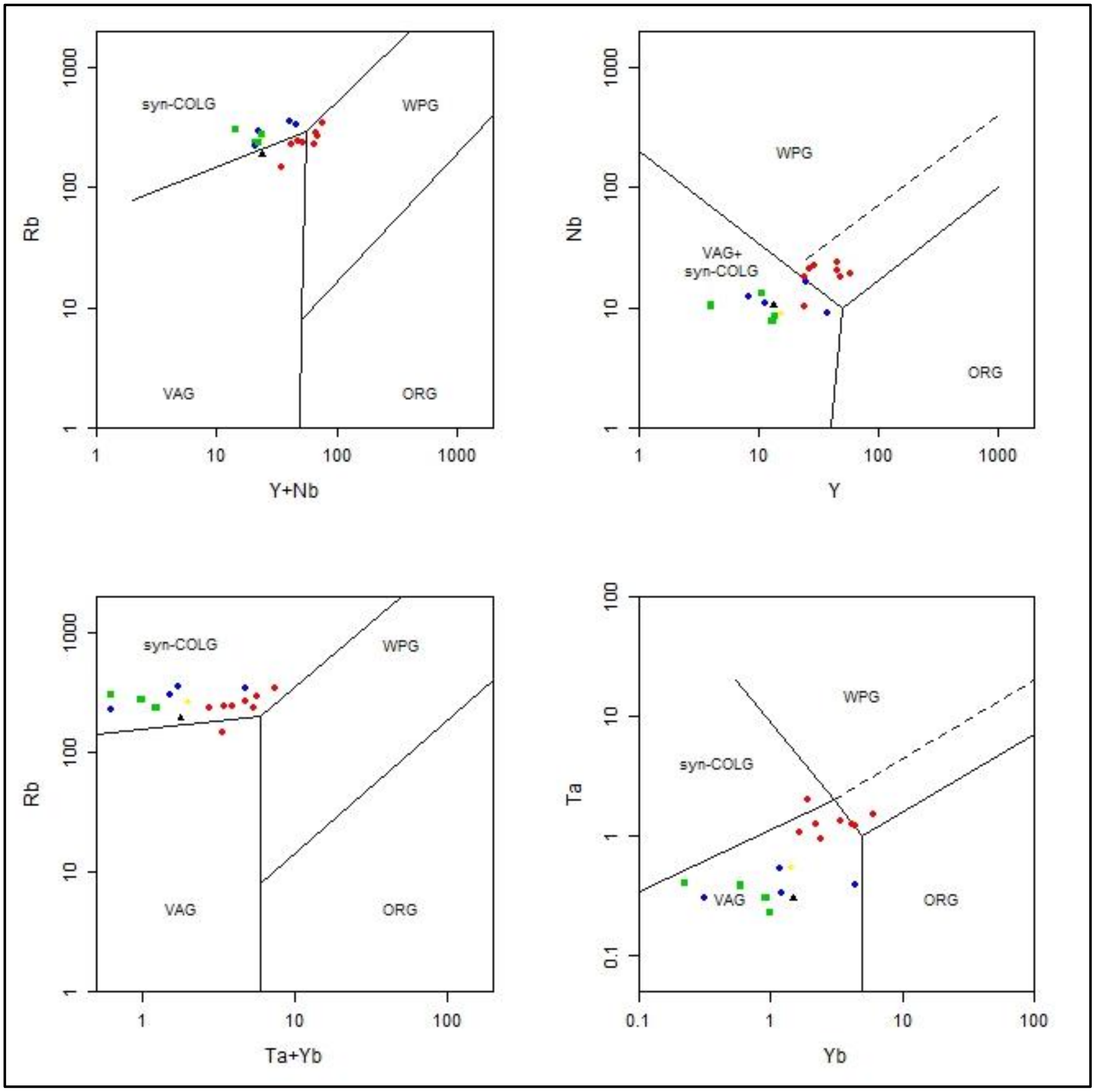

Figure 4. 23: Pearce et al. (1984) tectonic discrimination diagrams for the granitoids. Symbols as for Figure 4.19.

4.5. Geochronology of intrusive rocks in the Aus Domain

The study area is dominated by the Aus, Tsirub and Kubub granite gneisses, and copper mineralization is mostly associated with these gneisses. No age dating was conducted on Tsirub and Aus granite gneisses in the past. Since the mineralization was found to be associated with these rocks, therefore it is important to determine their ages and in turn to establish the stratigraphic sequence and timing of tectonic events within the study area. The U-Pb zircon dating method was used and the data is presented in Appendix G.

4.5.1. CM19098 Aus granite gneiss

Sample CM19098 is a leucocratic coarse grained megacrysts Aus granite gneiss composed of large K-feldspar, quartz, plagioclase, biotite and garnet (Figure 4.24a). This rock is classified as a granite and plots within the calc-alkaline series. The sample contains dominantly subhedral shaped and highly fractured zircons (Figure 4.24b) with a long axis diameter in the range of ~100-250μm (Figure 4.24 b and c). Out of about 40 zircon samples submitted, only seven grains were useful. The Aus granite gneiss consists of zircons which are seen in backscattered electron images to mainly comprise a domain which has faint oscillatory zonation typical of magmatic zircon (Figure 4.24b). The oscillation zonation is caused by different crystal faces taking in different amounts of Th and U from the magma as they grow. Nine analyses were made but only three were useable due to high common Pb in the other grains. The data shows a slight deviation from the Concordia line. Few cathodoluminescence (CL) dark rims suggest metamorphic cores examples 2b1, 2b2, 3c, 4b, 8b1, 8b2, 10c1 and 10c2 (Figure 4.24c). Zircon points that show igneous cores are 2a, 4a1, 4a2, 5a, 9a1 and 9a2 (Figure 2.24c).

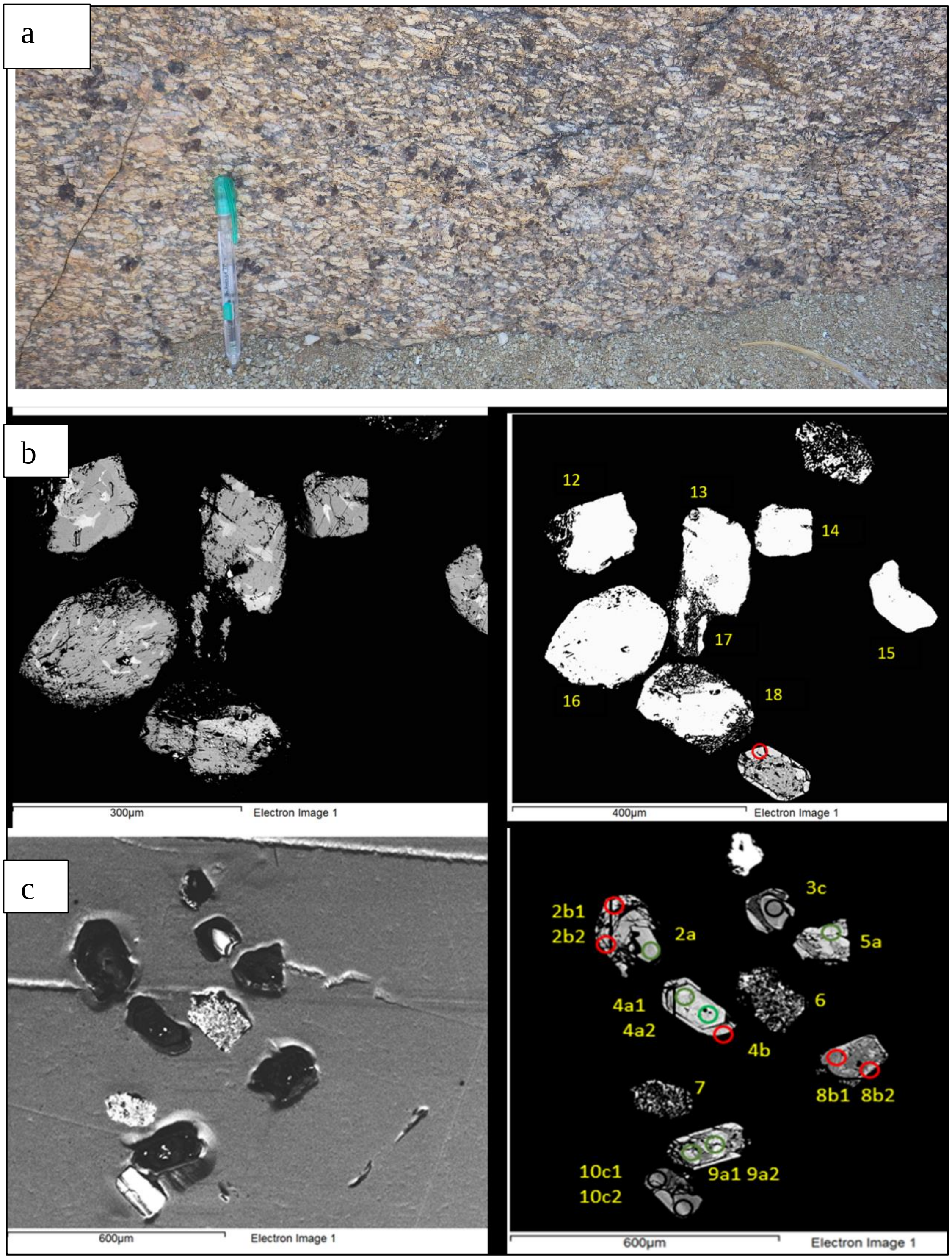

Figure 4. 24: a) Photograph of the rock sampled and b and c) Cathodoluminescence (CL) images of representative zircons from sample CM19098. Black, red and green circles represent spot localities with their corresponding numbers in yellow.

However, results of 2a, 4a2, 9a1 and 9a2 are not used because their ages are highly discordant, which are probably xenocrysts. Only results of two igneous core points (4a1 and 5a) were reliable which give a weighted mean $^{207}Pb/^{206}Pb$ age of **1085 ± 36** Ma (2σ) (Figure 4.25), which represents the age of crystallization of the Aus granite gneiss. This age is still unreliable because the age range is too wide.

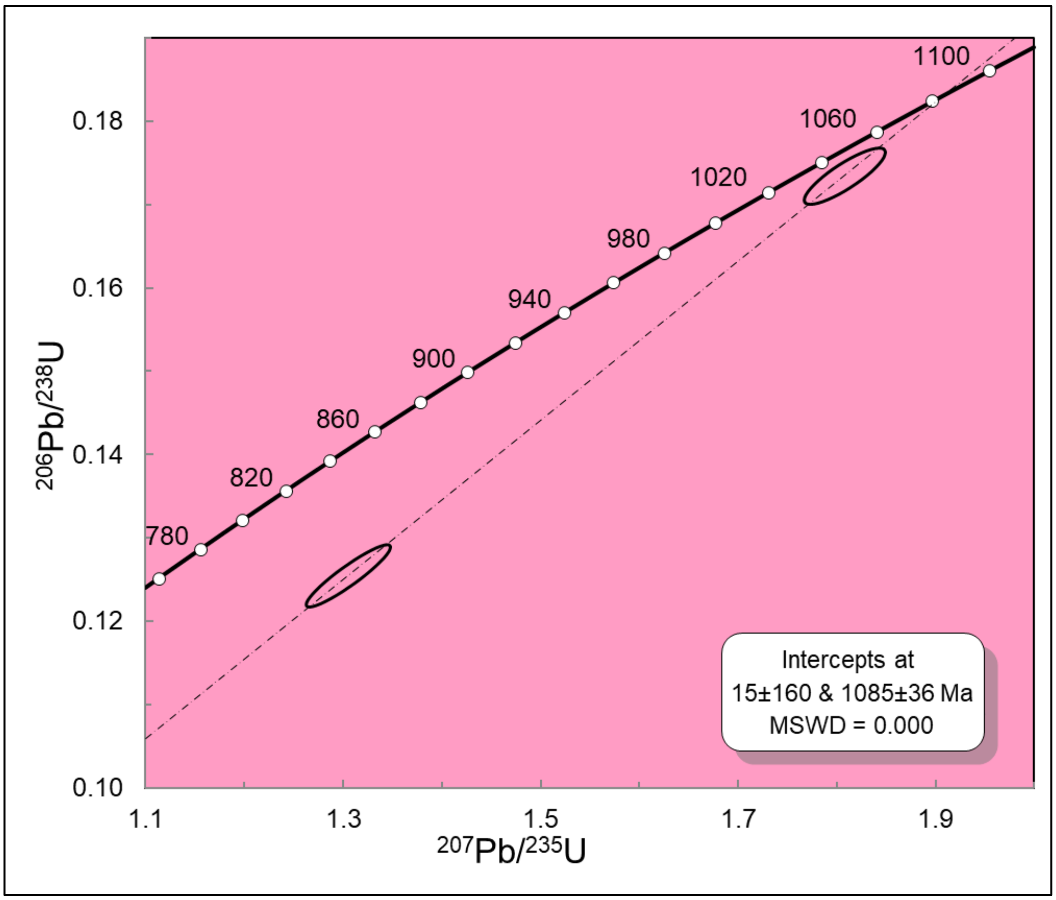

Figure 4. 25: Concordia diagram showing U-Pb data and age calculation for sample CM19098 Concordia age = 1085 ± 36 Ma.

4.5.2. CM19099 Tsirub augen gneiss

Sample CM19098 is a dark-grey, coarse grained, megacrystic granodioritic Tsirub augen gneiss composed of quartz, plagioclase, biotite, hornblende and garnets (Figure 4.26a). This rock is classified as a granodiorite and plots at the boundary between tholeiite and calc-alkaline series.

Out of ca. 40 zircon samples submitted, only 22 zircon grains were useful. The majority of the zircons are subhedral to anhedral with maximum lengths ranging between 60 and 300µm (Figure 4.26b and c). Zircons from this sample have a CL bright main domain (Figure 4.26b and c), and some grains have darker cores. The backscattered electron images show zircons to mainly comprise a main domain with oscillatory zonation and is prismatic in shape, typical for magmatic zircons (e.g 11, 18 and 14). Nineteen good points were analyzed in 8 grains and 4 were excluded due to common Pb. The green circles mark the CL dark rims which suggest metamorphic cores, examples 1b1, 1b2, 2b, 3c, 4c, 5b, 9b1, 9b2, 9c, 10b, 11c, 12b, 14b, 15b, 18b1 and 18b2 (Figure 4.26b and c). Zircon points that show igneous cores are marked with black circles, examples 1a, 2a, 6a, 7a, 12a, 13a, 15a, 18a1, 18a2, 20a and 21a (Figure 4.26b and c). The data is nearly concordant. Core and main magmatic age domains seen in cathodoluminescent images did not show any systematic differences. However, combining the group of igneous core points give a weighted mean $^{207}Pb/^{206}Pb$ age of **1110 ± 7 Ma** (2σ) (Figure 4.27), which is the crystallization age of the Tsirub augen gneiss. Since the results are plotting on the Concordant line, therefore the age obtained is reliable.

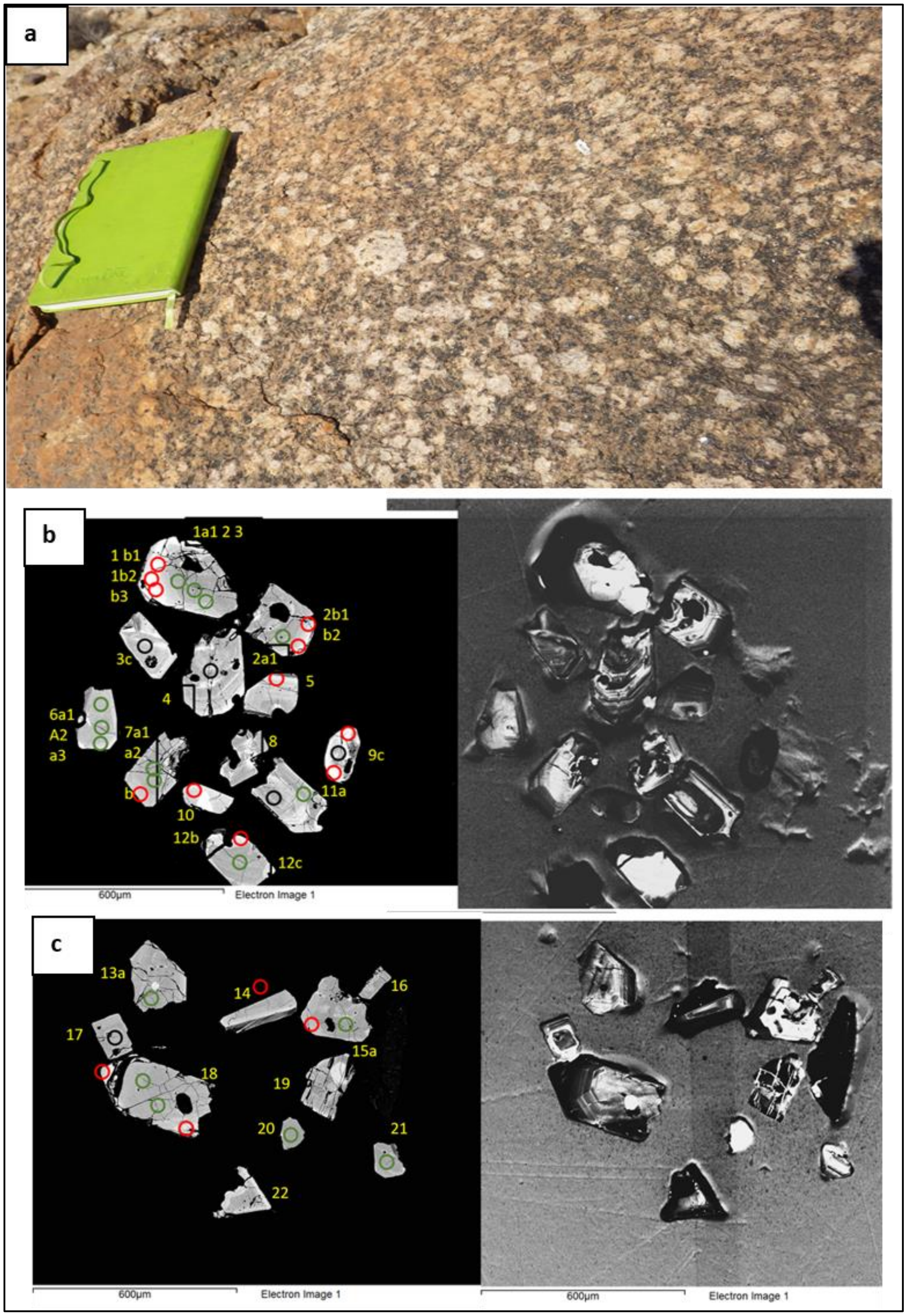

Figure 4. 26: a) Photograph of the rock sampled; b) and c) CL images of representative zircons from sample CM19099. Black, red and green circles represent spot localities with their corresponding numbers in yellow.

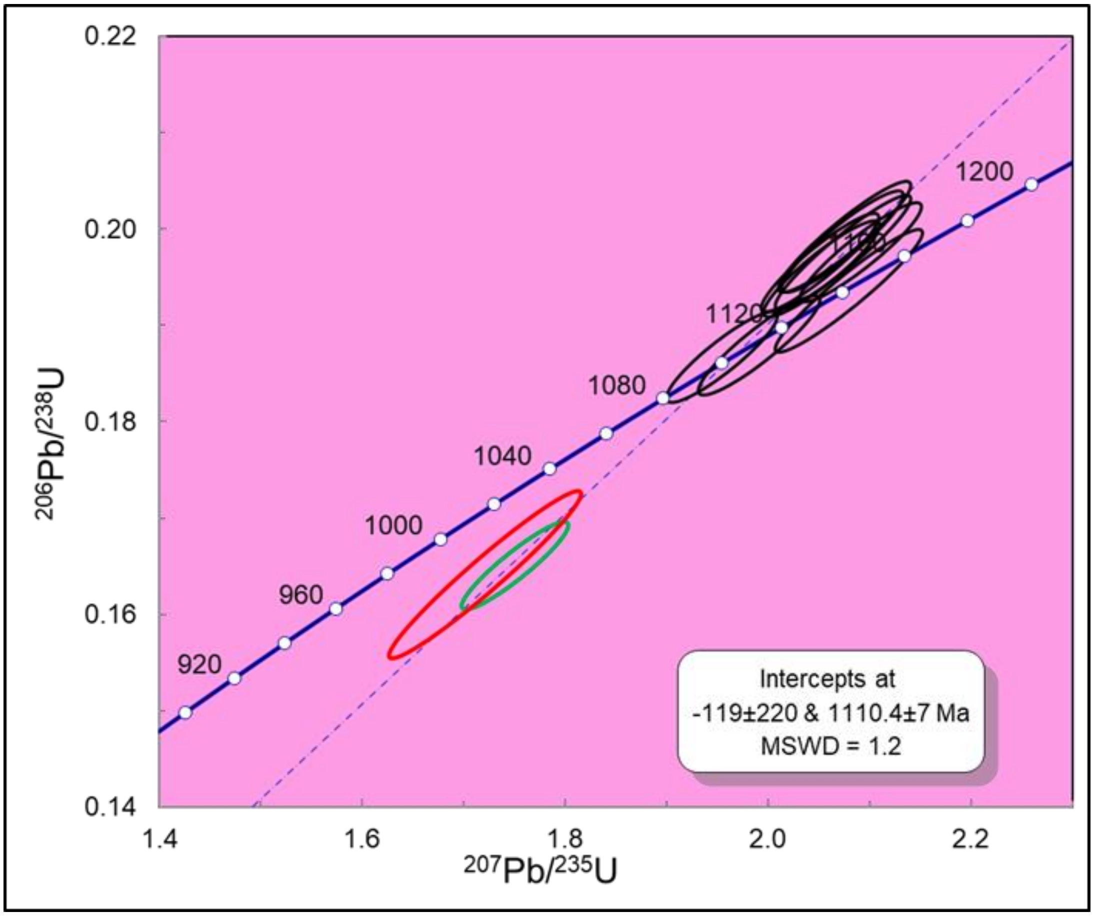

Figure 4. 27:Concordia diagram showing U-Pb data and age calculation for sample CM19098 Concordia age = 1110 ± 7 Ma.

CHAPTER 5: DISCUSSIONS

5.1. The geology of Aus Domain

The study area is characterized by supracrustal rocks of the Garub Group, consisting of marble, calc-silicates, metapelites, amphibolites, garnet biotite quartz gneisses, mafic granulites and serpentinite, which have been intruded by granite gneisses. Jackson (1976) mapped the same rocks in the area, however the biotite schist of Jackson (1976) has been renamed to garnet biotite gneiss in this study as it possesses compositional banding (Figure 4.3). The granitoids crop out as voluminious boulders and pavements, which form a continuous outcrop area on the 1: 50 000 geological map (Figure 4.12), whereas supracrustal rocks form lensoid bodies scattered throughout the granitoid terrain (Figure 4.1a). The presence of Garub Group xenoliths within the Tsirub and Aus granite gneisses suggest that the granite gneisses postdated the deposition of the Garub Group (Figure 4.8). Similarly, the occurrence of Tsirub augen gneiss xenoliths within the Aus granite gneiss (Figure 4.9) demonstrate that the latter is younger than the Tsirub augen gneiss. No evidence of Tsirub augen gneiss cross-cutting the Garub Group has been found and this evidence suggests that the Tsirub augen gneiss is pre-tectonic. Aus granite gneiss is classified as syntectonic intrusive granites on the basis of its porphyroblastic character (Jackson, 1976), while Kubub granite gneiss is classified as post-tectonic granite dyke intruded after the terrain cooled due to the cross-cutting relationship of Tsirub and Aus granite gneisses and its pegmatititc texture (Jackson, 1976; Diener et al., 2013) which is in agreement with this study.

The granite gneisses are variably deformed, with megacystic to porphyroblastic textures. Petrographic observations confirm the compositional and deformational variability observed in the field, for examples highly altered garnet and cordierite replaced by biotite (Figure 4.2 f) and plagioclase altered to sericite (Figure 4.9f) although some igneous minerals such as hornblende are preserved (Figure 4.4f). Quartz is the abundant mineral particularly in the granites which suggest that these rocks have undergone fractionation.

5.2. Structural framework of Aus Domain

Aus Domain is characterized by a polyphase deformation that is dominated by five tectonic episodes namely D1, D2, D3, D4 and D5 (Jackson, 1976). These events are recorded in the present study area. The D1 deformation event is attributed to the formation of the banding seen in the Garub Group, for example within the garnet biotite gneiss and metapelites. The D2 deformation event resultant into penetrative mineral foliations and stretching lineations and D3 is responsible for the folding structures in the area. The foliations in the northern part of the study area are dominantly striking NE-SW, whereas central and southern of the area the foliation strikes NW-SE (Figure 4.13). The dextral shearing of the augens in the Tsirub augen gneiss is attributed to D4 deformation event in addition to the east-west trending shear zones. Fault structures are prominent in the area which are related to D5 deformation event striking in two major directions N-S and NW-SE (Figure 4.14).

5.3. Metamorphic conditions of the Aus Domain

Peak metamorphic conditions in the Domain are constrained at 5.5 kbar and 825 °C (Diener et al., 2013). The presence of sillimanite + cordierite + garnet mineral assemblage in the metapelites indicates upper amphibolite facies (Figure 4.2f). Also, the presence of orthopyroxene + diopside + hornblende + plagioclase + quart in the mafic granulite suggest upper amphibolite to granulite facies metamorphism. The metapelite and mafic granulite assemblages probably originated during the early-Kibaran anatexis at 1351 to 1299 Ma (Bial et al., 2015b) or else during the regional metamorphic event around ~1220 Ma (Bial et al., 2015a, 2015b; Eglington, 2006; Macey et al., 2015). However, most of the petrographic sections observed in this study show breakdown of cordierite and garnet to biotite and of potassium feldspar to sericite (Figures 4.2f and 4.9c), which suggests rehydration associated with retrograde metamorphism under greenschist facies conditions, probably at temperatures below 450 °C (Baltatzis, 1979; Deer et al., 1992). Wollastonite found within the calc-silicate rocks of the Garub Group and the occurrence of mafic granulites in association with calc-silicate indicates that, at least locally, high-grade metamorphic conditions are achieved. At least 3 kb and temperatures in the order of 700-800 °C are required to form wollastonite by the reaction of calcite with quartz where X_{H2O} would be low (Winkler, 1974). This is in support with the peak metamorphic results by Diener et al., 2013.

5.4. Tectonic setting of the Aus Domain

Geochemical analyses reveal that all plutonic rocks are acidic, with compositions ranging from granitic to granodioritic. These granitoids are products of shoshonitic to high-K calc alkaline magmas within a calc-alkaline series, which points to their formation in a magmatic arc environment (Liégeois et al., 1998, Clarke, 2019). They are also strongly peralumious with few granites plotting in the metalumious field reflecting the commonly garnetiferous, pelite xenolith-rich nature of these granites, and plot within the A-type field of the Whalen et al. (1987) discriminatory diagram (Figures 4.22). On Harker diagrams, the granitoids display trends of decreasing Al_2O_3, CaO, FeO_t, MgO, TiO_2, P_2O_5, MnO, Sr, Ba, Ta and Nb, but an increase in K_2O, Na_2O, Th, Ce, Sm, Y, Hf and Rb with increasing SiO_2 (Figure 4.18). These trends suggest the progressive fractional crystallisation of plagioclase, amphibole, monazite, sphene and zircon, but limited fractional crystallisation of K-feldspar and biotite (Macey et al., 2015). The broadly coherent trends of mobile elements such as Rb, Sr and Ba indicate little or no alteration during metamorphism or weathering (Whalen et al., 1987). The higher Al_2O_3 and K_2O and lower Fe contents of the granitoids is probably due to a greater contamination by pelites. Negative Ta, Nb, P and Ti anomalies, with enrichments in Th and LREE, which are typical of arc-derived rocks (Whalen et al., 1987) suggest continental crust involvement.

Based on the tectonic discrimination diagrams (Figure 4.23), three geotectonic settings can be established i. e. syn-collisional-Granite (syn-COLG), Volcanic Arc Granites (VAG;) and Within Plate Granites (WPG). These inconsistent plots of samples may be attributed to hydrothermal alteration and/or sharing of varying degrees of fractionation within multiple flows. This evidence is in support of Colliston and Schoch, (2013) and Colliston et al. (2015), who proposed a collision of crustal fragments model. Additionally, plots of K_2O vs SiO_2 (Figure 4.19b) show a considerable degree of scatter which may be attributed to the effects of crustal contamination in an active continental margin environment (Wilson, 1986). Similarly, the chemistry of high-silica rocks e.g Tsirub augen gneisses indicates crustal participation in their parental melts and within-plate extensional affinities (Whalen et al., 1987).

5.5. Age of magmatism of the Aus Domain

The U-Pb results reported the age of crystallization of the Tsirub and Aus granite gneisses to be 1110 ± 7 Ma and 1085 ± 36 Ma respectively. These ages are similar to the timing of regionally extensive granitoid intrusion in the NNMP (Eglington & Armstrong, 2003; Colliston & Schoch, 2013). Field evidence suggest that Tsirub augen gneiss is older than Aus granite gneiss although geochronology results reported coeval ages taking into account the error of uncertainties.

5.6. Mineralization of the Aus Domain

Presence of malachite is a good surface indicator for copper exploration. The malachite in this study is associated with structures such as lithological contacts parallel to foliation, quartz veins and fault planes. This mineralization is probably originated as a result of heat from the granites present in the area. The K-feldspar plagioclase epidote rock is one of the rocks in the area which is intensively fractured and massively intruded by quartz and pegmatite veins. However, no malachite was found to be associated with this rock. Additionally, geochemistry samples reported very low copper content (1.586-86.430 ppm) and this could be due to unsystematic way of sampling within the mineralised zone.

In comparison with the Okiep Copper District located within the Namaqua sector in South Africa, U/Pb age dating of the copper-bearing Koperberg granite Suite reported age range of 1020-1040 Ma (Clifford et al.1995, 2004) which somehow coincides with the ages reported in this study (1085-1110 Ma).

CHAPTER 6: CONCLUSIONS AND RECOMMENDATIONS

The Garub Group constitutes the oldest rocks in the Aus area and comprises a diverse assembly of layered pretectonic metasedimentary and metavolcanic rocks with subordinate mafic granulite. The Garub Group has been intruded by voluminous felsic granite gneisses which are variably deformed. Granite gneisses form a continuous outcrop area on the 1: 50 000 geological map, whereas Garub Group forms lensoid bodies scattered throughout the granitoid terrain. The granitoids are strongly peralumious and classified as A-type granites which formed as a result of crustal contamination during the continental extensional phase and have been subjected to compressional deformation. Copper mineralization, malachite, occurs in three forms i) at the contact between Garub Group and Tsirub augen gneiss, ii) quartz vein related and iii) along fault planes. The age of crystallization of the Tsirub augen gneiss and Aus granite gneiss is reported to be 1110 ± 7 Ma and 1085 ± 36 Ma respectively, with copper mineralization being related to the granitoid intrusion event.

I would therefore recommend:

1. geochemical analysis of the K-feldspar plagioclase epidote rock (as shown on the geological map) to establish the origin of this rock and determine the mobility of elements as well as the copper content. The geological map will guide where this rock is located.

2. isotope analysis to determine the source of fluids responsible for mineralization.

REFERENCES

Angombe, M.T., 2016. The lithostratigraphy and structural components of the Eureka Shear Zone, southern Namibia. Case study of the Eureka Shear Zone in Namibia. University of Stellenbosch. pp. 121.

Bailie, R., Armstrong, R., Reid, D., 2007a. The Bushmanland Group supracrustal succession, Aggeneys, Bushmanland, South Africa: Provenance, age of deposition and metamorphism. South African Journal of Geology, 110, 59-86.

Bailie, R., Armstrong, R., Reid, D., 2007b. Composition and single zircon U-Pb emplacement and metamorphic ages of the Aggeneys Granite Suite, Bushmanland, South Africa: South African Journal of Geology, 110, 87–110.

Bailie, R., Gutzmer, J., Strauss, H., Stüeken, E., McClung, C., 2010. Sulfur isotope characteristics of metamorphosed Zn–Cu volcanogenic massive sulfides in the Areachap Group, Northern Cape Province, South Africa. Mineralium Deposita, 45, 481–496.

Bailie, R., Rajesh, H.M., Gutzmer, J., 2012. Bimodal volcanism at the western margin of the Kaapvaal Craton in the aftermath of collisional events during the Namaqua- Natal Orogeny: The Koras Group, South Africa. Precambrian Research 200–203, 163–183.

Baltatzis, E., 1979. Distribution of Fe and Mg between garnet and biotite in Scottish Barrovian metamorphic zones. Mineralogical Magazine 43, 155–7.

Barr, J.M., Reid, D.L., 1993. Hydrothermal mineralization at the Haib porphyry copper prospect, southern Namibia. Communication, Geological Survey of Namibia, 8, 23–34.

Becker, T., Schreiber, U., Kampunzu, A.B., Armstrong, R., 2006. Mesoproterozoic rocks of Namibia and their plate tectonic setting. Journal of African Earth Sciences 46, 112–140.

Beetz, W., 1924. On a great trough-valley in the Namib. Geological Society of South Africa. Trans, 27, 1-33.

Beukes, G.J., 1973. Geologiese ondersoek van die gebied suid van Warmbad, Suidwes-Afrika, met spesiale verwysing na die metamorf-magmatiese assosiasies van die Voorkambriese gesteentes. D.Sc. Thesis, University of the Orange Free state, Bloemfontein, p. 333.

Bial, J., Buttner, S., Appel, P., 2016. Timing and conditions of regional metamorphism and crustal shearing in the granulite facies basement of south Namibia: Implications for the crustal evolution of the Namaqualand metamorphic basement in the Mesoproterozoic. Journal of African Earth Sciences, 123, 145-176.

Bial, J., Büttner, S.H., Frei, D., 2015a. Formation and emplacement of two contrasting late-Mesoproterozoic magma types in the central Namaqua Metamorphic Complex (South Africa, Namibia): Evidence from geochemistry and geochronology. Lithos 224-225, 272–294.

Blignault, H.J., 1977. Structural-metamorphic imprint on the part of the Namaqua mobile belt in South West Africa. Bulletin, Precambrian research, University of Cape Town 23, 197.

Blignault, H.J., Van Aswegen, G., Van Der Merwe, S.W., Colliston, W.P., 1983. The Namaqualand geotraverse and environs: part of the Proterozoic Namaqua mobile belt. Geological Society of South Africa, Special Publication 10, 1-29.

Brimhall, G.H., Dilles, J.H., Proffett, J.M., 2006. The role of geologic mapping in mineral exploration: Society of Economic Geologists Special Publication 12, 221−241.

Bowles, M., 1988. Metallogeny of stratabound tungsten mineralization in the Namaqualand Metamorphic Complex, northwest Cape, South Africa – a consanguineous view. S. Afr. J. Geol., 91, 248–258.

Cawthorn R.G., Meyer, F.M., 1993. Petrochemistry of the Okiep Copper District basic intrusive bodies, northwestern Cape Province, South Africa. Economic Geology 88, 590–605.

Clarke, D. 2019. The Origins of Strongly Peraluminous Granitoid Rocks. The Canadian Mineralogist, 57 (4), 529-550.

Clifford, T. N., Barton, E., Stern, R. A., Duchesne, J., 2004. U-Pb zircon calendar for Namaquan (Grenville) crustal events in the granulite-facies terrane of the Okiep Copper District of South Africa. Journal of Petrology, 45(4), 669-691.

Clifford, T.N., Barton, E.S., Retief, E.A., Rex, D.C., Fanning, C.M., 1995. A crustal progenitor for the intrusive anorthosite-charnockite kindred of the cupriferous Koperberg Suite, Okiep district, Namaqualand, South Africa; new isotope data for the country rocks and the intrusives. Journal of Petrology, 16, 154–188.

Colliston, W.P., Schoch, A.E., 2013. Wrench-shearing during the Namaqua Orogenesis-Mesoproterozoic late stage deformation effects during Rodinia assembly. Precambrian Research 232, 44–58.

Cornell, D.H., Hawkesworth, C.J., Van Calsteren, P., Scott, W.D., 1986. Sm–Nd study of Precambrian crustal development in the Prieska-Copperton region, Cape Province. Transactions of the Geological Society of South Africa, 89, 17–28.

Cornell, D.H., Humphreys, H., Theart, H.F.J., Scheepers, D.J., 1992. A collision-related pressure-temperature-time path for Prieska Copper Mine, Namaqua-Natal tectonic Province, South Africa. Precambrian Res., 59, 43–71.

Cornell, D.H., Humphreys, H.C., Theart, H.F.J., Scheepers, D.J., 1992. A collision-related pressure-temperature-time path for Prieska copper mine, Namaqua-Natal tectonic Province: South Africa. Precambrian Research, 59, 43–71.

Cornell, D.H., Kröner, A., Humphreys, H.C., Griffin, G., 1990a. Age of origin of the polymetamorphosed Copperton Formation, Namaqua-Natal Province, by single grain zircon Pb–Pb dating: South African Journal of Geology, 93, 709–714.

Cornell, D.H., Pettersson, Å., 2007a. Ion probe dating of the Achab Gneiss, a young basement to the Central Bushmanland ore district? African Journal of Earth Sciences, 47, 112–116.

Cornell, D.H., Theart, H.F.J., Humphreys, H.C., 1990b. Dating a collision-related metamorphic cycle at Prieska copper mines, South Africa. In: Spry, P.G., Bryndzia, T. (Eds.), Regional Metamorphism of Ore Deposits and Genetic Implications, vol. 11. VSP, Utrecht, pp. 97–116.

Cornell, D.H., Thomas, R.J., Moen, H.F.G., Reid, D.L., Moore, J.M., Gibson, R.L., 2006. The Namaqua-Natal Province, in: In: Johnson, M.R, Anhaeusser, C.R and Thomas, R.J. (Eds.), The Geology of South Africa. Geological Society of South Africa. Johannesburg/Council for Geoscience, Pretoria. pp. 325–343.

Cox, K.G., Bell, J.D., Pankhurst, R.J., 1979. The interpretation of igneous rocks. George, Allen and Unwin, London.

Deer, W.A., Howie, R.A., Zussman, J., 1992. An introduction to the rock forming minerals, second. ed. Pearson Education limited, London.

Diener, J. F., White, R. W., Link, K., Dreyer, T. S., Moodley, A., 2013. Clockwise, low-P metamorphism of the Aus granulite terrain, southern Namibia, during the Mesoproterozoic Namaqua Orogeny. Precambrian Research, 224, 629-652.

Eglington, B.M., 2006. Evolution of the Namaqua-Natal Belt, southern Africa – A geochronological and isotope geochemical review. Journal of African Earth Sciences, 46(1–2), pp. 93-111.

Eglington, B.M., Armstrong, R.A., 2003. Geochronological and isotopic constraints on the Mesoproterozoic Namaqua-Natal Belt: Evidence from deep borehole intersections in South Africa. Precambrian Research 125, 179–189.

Flanagan, D.M., 2018. Copper. In: The USGS Mineral Resources Program. Geological Survey of United states.

Frimmel, H.E. (2000). Formation of late Mesoproterozoic Supercontinent: The South Africa-East Antarctica connection, in: The precambrian Earth: Tempos and events.

Hartnady, C.J.H., Joubert, P. and Stowe, C.W., 1985. Proterozoic crustal evolution in southwestern Africa. Episodes, 8, pp. 236 - 244.

Humphreys, H.C. and Van Bever Donker, J.M., 1987. Aspects of deformation along the namaqua province eastern boundary, kenhardt district, South Africa. Precambrian Research 36, 39–63.

Indongo, J., 2017. The Lithological and Structural Characterisation of the Sperlingputs Shear Zone in Southern Namibia. Master thesis. University of Stellenbosch, pp. 136.

Irvine, T.N. and Baragar, W.A.A. 1971. A guide to chemical classification of the common volcanic rocks. Can. J. Earth Sci., 8, pp. 528-548.

Jackson, M.P.A., 1976. High-grade Metamorphism and Migmatization of the Namaqua Metamorphic Complex Around Aus in the Southern Namib Desert; South West Africa. Ph.D. thesis. University of Cape Town. pp. 299.

Joubert, P., 1986. The Namaqualand Metamorphic Complex - A summary. In: C.R. Anhaeusser and S. Maske (Eds.) Mineral Deposits of South Africa, Vols I & II, Geological Society of South Africa, pp. 1395 - 1420.

Kwelwa, S.D., Dirks, P.H.G.M., Sanislav, I.V., Blenkinsop, T., Kolling, S.L., 2018. Archaean gold mineralization in an extensional setting: The structural history of the Kukuluma and Matandani Deposits, Geita Greenstone Belt, Tanzania. Minerals 8, 171.

Lambert, C.W., 2013. Granitic melt transport and emplacement along transcurrent shear zones: Case study of the Pofadder Shear Zone in South Africa and Namibia. University of Stellenbosch.

Le Roex, A., Späth, A., Zartman, R., 2001. Lithospheric thickness beneath the southern Kenya Rift: Implications from basalt geochemistry. Contributions to Mineralogy and Petrology. 142(1), 89-106.

Liégeois, J.P., Navez, J., Hertogen, J., Black, R., 1998. Contrasting origin of post-collisional high-K calc-alkaline and shoshonitic versus alkaline and peralkaline granitoids. The use of sliding normalization. Lithos. 45. 1-28.

Ludwig, K.R., 2012. Isoplot/Ex rev. 3.75 – A Geochronological Toolkit for Microsoft Excel. Berkeley Geochronology Center Special Publication, No. 5, p.75.

Macey, P.H., Minnaar, H., Miller, J.A., Lambert, C.W., Groenewald, C., Indongo, J., Angombe, M.T., Hendrik, S., Shifotoka, G., Diener, J., le Roux, P., Frei, D., 2015. The Precambrian Geology of the Region South of Warmbad from Haib to Velloorsdrif, Southern Namibia, An Explanation to 1:50 000 Geological Map Sheets 2818AC, 2818AD, 2818CA, 2818CB,2818CC,2818CD,2818DA, 90 2819CA,2819CB, 2819CC, 2819CD and 2819DA.

Macey, P.H., Thomas, R.J., Minnaar, H.M. Gresse, P.G., Lambert, C.W., Groenewald, C.A., Miller, J.A., Indongo, J.L., Angombe, M., Shifotoka, G., Frei, D., Diener, J.F.A., Kisters, A.F.M., Dhansay, T. Smith, H., Doggart, S., Le Roux, P., Hartnady, M.I. and Tinguely, C., 2017. Origin and evolution of the ~1.9 Ga Richtersveld MagmaticArc, SW Africa, Precambrian Research.

Maier, W.D., Andreoli, M.A.G., Groves, D.I., Barnes, S.J., 2013. Petrogenesis of Cu-Ni sulphide ores from Okiep and Kliprand, Namaqualand, South Africa: constraints from chalcophile metal contents. South African Journal of geology, 115, 499-514.

McIver, J.R., McCarthy, T.S., Packham, B.V., 1983. The copper-bearing basic rocks of Namaqualand, South Africa. Mineralium Deposita 18, 135–160.

Miller, R.M., 2008. The geology of Namibia. Handbook, Geological Survey of Namibia, 3 volumes.

Miller, R.M., 2012. Review of Mesoproterozoic magmatism, sedimentation and terrane amalgamation in southwestern Africa. South African Journal of Geology 115, 417–448.

Moen, H.F.G., Toogood, D.J., 2007. Geology of the Onseepkans Area. Pretoria, South Africa: Council for Geoscience.

Moore, J.M., Watkeys, M.K., Reid, D.L., 1990. The regional setting of the Aggeneys/Gamsberg base metal deposits, Namaqualand, South Africa. In: Spry, P.G., Bryndzia, L.T. (Eds.), Regional Metamorphism of Ore Deposits and Genetic Implications: Proceedings of the 28th International Geological Congress. Washington, USA, VSP, Utrecht, Netherlands 85, 77–95.

Nakamura, N., 1974. Determination of REE, Ba, Fe, Mg, Na and K in carbonaceous and ordinary chondrites. Geochimica et Cosmochimica Acta 38, 757–775.

National Planning Commission of Namibia., 2018. Status of the Namibian economy. Namibia, Windhoek.

Nordin, F., 2009. U-Pb dating, Lu-Hf isotopic analysis and geothermobarometry of rocks in the Grünau terrane and Richtersveld sub-province, Namaqua Sector, Southern Africa. Department of Earth Sciences, Geology, University of Gotenburg, Sweden.

Nujoma, S., 2009. Copper – Its geology and economic impact on the development in Namibia, Zambia and the Democratic Republic of the Congo. Master thesis. University of Namibia. pp. 128.

Pearce, J.A., Harris, N.B.W., Tindle, A.G., 1984. Trace element discrimination diagrams for the tectonic interpretation of granitic rocks. Journal of Petrology, 25, 956–983.

Peccerillo, A., Taylor, S.R., 1976. Geochemistry of Eocene calc-alkaline volcanic rocks from the Kastamonu area, northern Turkey. Contrib. Mineral. Petrol. 58, 63–81.

Raith, J., Harley, S., 1998. Low-P/high-T metamorphism in the Okiep Copper District, western Namaqualand, South Africa. Journal of Metamorphic Geology, 16(2), 281-305.

Reid, D.L., 1997. Sm-Nd age and REE geochemistry of Proterozoic arc-related igneous rocks in the Richtersveld Subprovince, Namaqua Mobile Belt, Southern Africa. Journal of African Earth Sciences, 24(4), p. 621 – 633.

Robb, L., Armstrong, R., Waters, D., 1999. The history of granulite-facies metamorphism and crustal growth from single zircon U-Pb geochronology: Namaqualand, South Africa. Journal of Petrology, 40(12), 1747-1770.

Ryan, P.J., Lawrence, A.L., Lipson, R.D., Moore, J.M., Paterson, A., Stedman, D.P., Van Zyl, D., 1986. The Aggeneys base metal sulphide deposits, Namaqualand district. In: C.R. Anhaeusser and S. Maske (Eds.), Mineral Deposits of Southern Africa, vol. II, Special Publication of the Geological Society of South Africa, 1447-1474.

Samskog, P., 2009. U-Pb, Lu-Hf zircon dating and source magma determination of magmatic rocks in the Richtersveld and Kakamas terrane, Namaqua Province, Southern Africa. Department of Earth Sciences, Geology, University of Gothenburg, Sweden.

Schade, J., Cornell, D.H., Theart, H.F.J., 1989. Rare earth element and isotopic evidence for the genesis of the Prieska massive sulfide deposit, South Africa. Econ. Geol., 84, 49–63.

Schneider, G.I.C. and Seeger, K.G., 1992. Copper. In: The Mineral Resources of Namibia. Geological Survey of Namibia.

Schoch, A.E., Conradie, J., 1990. Petrochemical and mineralogical relationships in the Koperberg Suite, Namaqualand. American Mineralogist 75, 27–36.

Sebetlela, T., 2017. Tectonometamorphic evolution of Medium-P granulites of the Namaqua Metamorphic Province at the Richtersveld - Gordonia Subprovince marginal zone, southern Namibia. University of Cape Town.

Shand, S.J., 1943. Eruptive Rocks. Their Genesis, Composition, Classification, and Their Relation to Ore-Deposits with a Chapter on Meteorite. John Wiley & Sons, New York.

Sillito, R.H., 2003. Iron oxide-copper-gold deposits: An Andean view. Miner. Deposita 38, 787–812.

Sillitoe, R.H., 1972. A plate tectonic model for the origin of porphyry copper deposits. Econ. Geol. 67, 184–197.

Stacey, J.S., Kramers, J.D., 1975. Approximation of Terrestrial Lead Isotope Evolution by a 2-Stage Model. Earth and Planetary Science Letters 26(2), 207-221.

Theart, H.F.J., Cornell, D.H., Schade, J., 1989. Geochemistry and metamorphism of the Prieska Zn-Cu deposit, South Africa. Econ. Geol., 84, 34–48.

Thomas, R.J., Agenbacht, A.L.D., Cornell, D.H., Moore, J.M., 1994. The Kibaran of southern Africa: Tectonic evolution and metallogeny. Ore Geology Reviews 9, 131–160.

Toogood, D.J., 1976. Structural and Metamorphic Evolution of a Gneiss Terrain in the Namaqua Belt Near Onseepkans, South West Africa. Bulletin of the Precambrian Research unit, 19, 1–189.

Tosdal, R.M., Richards, J.P., 2001. Magmatic and structural controls on the developments of porphyry Cu ± Mo ± Au deposits. Rev. Econ. Geol. 14, 157–181.

Waters, D., 1986. Metamorphic zonation and thermal history of pelitic gneisses from western Namaqualand, South Africa. South African Journal of Geology, 89(2), 97-102.

Whalen, J.B., Currie, K.L., Chappell, B.W., 1987. A-type granites: geochemical characteristics, discrimination and petrogenesis. Contributions Mineralogical Petrology, 95, 407–419.

Winkler, H.G.F., 1974. Petrogenesis of metamorphic rocks. Springer-Verlag, New York, pp. 325.

Zeng, M., Zhang, D., Zhang, Z., Liu, T., Li, C., Wei, C., 2018. Structural controls on the Lala iron-copper deposit of the Kangdian metallogenic province, Southwestern China: Tectonic and metallogenic implications. Ore Geol. Rev. 97, 35–54.

APPENDICES

Appendix A: Field observation way points

Waypoint number/Sample ID	**Latitude**	**Longitude**	**Rock relationship and outcrop lithologies**	**Rocktype**
CM19001	-26.639953	16.318555	Pegmatite intrusion	Medium grained leucocratic quartzo feldspathic biotite gneiss
CM19002	-26.639082	16.306487	Medium grained leucocratic quartzo feldspathic biotite gneiss intruding within foliation	Aus gneiss
CM19003	-26.645013	16.293756	Tsirub gneiss intruded by Medium grained leucocratic quartzo feldspathic biotite gneiss	Tsirub gneiss
CM19004	-26.558951	16.306541	intruded by sheets of Medium grained leucocratic quartzo feldspathic biotite gneiss, cross cut by equigranular metagranite (GnBh)	hornblend biotite gneiss
CM19005	-26.568117	16.300517	Migmititic unit at the base, epidotised	Serpentinitte
CM19006	-26.622494	16.271918	Pegmatite intrusion	Amphibolite
CM19007	-26.62918	16.266956	Albitisation, metasomatism	Medium grained leucocratic quartzo feldspathic biotite gneiss
CM19008	-26.596065	16.203222		Aus gneiss
CM19009	-26.598199	16.202986		Marble
CM19010	-26.591471	16.201359		Aus gneiss
CM19011	-26.586336	16.202381		Aus gneiss
CM19012	-26.575325	16.200269		Amphibolite
CM19013	-26.571642	16.198685	Aus gneiss and biotite gneiss present	Meta Pelites
CM19014	-26.571182	16.198396	quarzofeldspathic biotite gneiss, Tsirub, biotite gneiss, Meta pelites, calc-silicates, amphibolite. Tsirub xenolith within Aus gneiss, biotite gneiss xenolith within Tsirub	Mixture
CM19015	-26.570132	16.194428		Tsirub gneiss
CM19016	-26.5801	16.15913	Fault zone	Aus gneiss
CM19017	-26.59907	16.16401		Medium grained leucocratic quartzo feldspathic biotite gneiss
CM19018	-26.598254	16.166461	Metasomatism	Aus gneiss
CM19019	-26.604525	16.16444	Contact between Tsirub gneiss and Aus gneiss, Tsirub xenolith within Aus	Tsirub gneiss/Aus gneiss
CM19020	-26.605238	16.16422	High strain zone	Tsirub gneiss
CM19021	-26.611313	16.169862		Tsirub gneiss
CM19022	-26.619778	16.175207	Metasomatism	Tsirub gneiss
CM19023	-26.620402	16.173647		Aus gneiss
CM19024	-26.625677	16.178774	Intruded by medium grained leucocratic quartzo feldspathic biotite gneiss	Tsirub gneiss
CM19025	-26.634121	16.173751		Aus gneiss
CM19026	-26.566174	16.179668	Fault zone	Aus gneiss
CM19027	-26.608841	16.222732	Marble unit at the top	Aus gneiss
CM19028	-26.612882	16.223347	Intruded by medium grained leucocratic quartzo feldspathic biotite gneiss	Tsirub gneiss
CM19029	-26.612833	16.228032	Contact between Tsirub gneiss and Aus gneiss, quartzo feldspathic biotite gneiss in parts with pegmatitic intrusion, marble unit on the north	Tsirub/Aus
CM19030	-26.613771	16.22817	Contact between Tsirub gneiss and Aus gneiss	Tsirub/Aus

CM19031	-26.613316	16.225562	Hydrothermal alteration zone about 3m, quartz vein	Scree
CM19032	-26.620311	16.225656		Aus gneiss
CM19033	-26.625077	16.220377	Largely intruded by pegmatites	Coarse grained leucocratic quartzo feldspathic biotite gneiss
CM19034	-26.631094	16.224292	small quarry, material for road construction?	Granofels
CM19035	-26.568243	16.1776		Aus gneiss
CM19036	-26.567648	16.180242	Fault breccia	Aus gneiss
CM19037	-26.570508	16.18374	intruded by quartzo feldspathic biotite gneiss and cross cut by undeformed leucocratic granite (Warmbad grainite?)	Tsirub gneiss
CM19038	-26.571619	16.183887	intruded by quartzo feldspathic biotite gneiss	Tsirub gneiss
CM19039	-26.573948	16.183902	intruded by a lense of quartzo feldspathic biotite gneiss and small outcrop of calc-silicate present about 5m wide	Tsirub gneiss
CM19040	-26.574101	16.18483		Medium grained leucocratic quartzo feldspathic biotite gneiss
CM19041	-26.574611	16.185406		Meta Pelites
CM19042	-26.579209	16.185886		Biotite gneiss
CM19043	-26.585643	16.184747	intruded by quartzo feldspathic biotite gneiss	Biotite gneiss
CM19044	-26.585901	16.195171	intruded by quartzo feldspathic biotite gneiss	Biotite gneiss
CM19045	-26.584866	16.197969	intruded by Aus gneiss	Biotite gneiss
CM19046	-26.610002	16.200927	intruded by quartzo feldspathic biotite gneiss, marble unit at the top of the northern mountain	Tsirub gneiss
CM19047	-26.615458	16.203127	Tsirub gneiss xenolith	Coarse - Medium grained leucocratic quartzo feldspathic biotite gneiss
CM19048	-26.616708	16.196978		Aus gneiss
CM19049	-26.627401	16.209855		Medium grained leucocratic quartzo feldspathic biotite gneiss
CM19050	-26.997464	16.196223		Medium grained leucocratic quartzo feldspathic biotite gneiss
CM19051	-27.003811	16.196498	amphibolite and biotite gneiss unit present	Medium grained leucocratic quartzo feldspathic biotite gneiss
CM19052	-27.000285	16.189024	Mixture of amphibolite, biotite gneiss and calc-silicates, strongly foliated	Medium grained leucocratic quartzo feldspathic biotite gneiss
CM19053	-26.999687	16.189755	Migmatitic, lenses of biotite gneiss at parts	Medium grained leucocratic quartzo feldspathic biotite gneiss
CM19053	-26.999687	16.189755	Intruded by quartzo-feldspathic biotite gneiss	Biotite gneiss
CM19054	-26.993837	16.192491	migmatitic, strongly deformed	Medium grained leucocratic quartzo feldspathic biotite gneiss
CM19055	-26.990673	16.183225	strongly deformed, migmatitic	Medium grained leucocratic quartzo feldspathic biotite gneiss
CM19056	-27.021356	16.206698	Intruded by undeformed leucocratic equigranular granite	Biotite granite gneiss
CM19057	-27.018715	16.204012		Biotite granite gneiss
CM19058	-26.979176	16.132024		Hornblend biotite gneiss
CM19059	-26.589189	16.236703	Intruded by medium grained leucocratic quartzo feldspathic biotite gneiss	Aus gneiss
CM19060	-26.59162	16.234982		Aus gneiss

CM19061	-26.587654	16.240763		Aus gneiss
CM19062	-26.581877	16.242546	medium grained leucocratic quartzo feldspathic biotite gneiss veins cross-cutting	Aus gneiss
CM19063	-26.572337	16.200269		Medium grained leucocratic quartzo feldspathic biotite gneiss
CM19064	-26.573479	16.200869	Hydrothermal alteration zone about 100m wide, amphibolite intruded by Aus	Amphibolite scree
CM19065	-26.585561	16.204724		Aus gneiss
CM19066	-26.600236	16.215856		Aus gneiss
CM19067	-26.602765	16.229478		Aus gneiss
CM19068	-26.603046	16.237594		Aus gneiss
CM19069	-26.609679	16.24801		Amphibolite
CM19070	-26.572193	16.193925	Remnant of biotite gneiss at parts	Tsirub gneiss
CM19071	-26.574907	16.193175	Tsirub, biotite gneiss, quartzo feldspathic biotite gneiss, calc-silicate, gabroic, Aus gneiss	Heterogeneous package
CM19072	-26.576042	16.192156		Calc-silicate
CM19073	-26.578112	16.192287	Tsirub xenolith	Aus gneiss
CM19074	-26.577525	16.191255	Malachite occurrence, albitisation	Tsirub gneiss
CM19075	-26.574249	16.191475	undeformed unit	warmbad granite?
CM19076	-26.571494	16.19229	Hydrothermal alteration, quartz veins present	Tsirub gneiss
CM19077	-26.713758	16.277316	biotite gneiss xenolith	Medium grained leucocratic quartzo feldspathic biotite gneiss
CM19078	-26.705082	16.258476	Iron alteration about 50m wide	Not mapped
CM19079	-26.56609	16.195271	Aus gneiss intruding in the foliation	Tsirub gneiss
CM19079	-26.56609	16.195271	Aus gneiss intruding in the foliation	Tsirub gneiss
CM19080	-26.566667	16.183333		Tsirub gneiss
CM19081	-26.563151	16.19436		Aus gneiss
CM19082	-26.566583	16.190892	intruded by medium grained leucocratic quartzo feldspathic biotite gneiss, hydrothermal alteration	Aus gneiss
CM19083	-26.564933	16.175739	Biotite gneiss at parts	Aus gneiss
CM19084	-26.555155	16.175474		Aus gneiss
CM19085	-26.559497	16.193949	Strongly fractured	Aus gneiss
CM19086	-26.548564	16.1795		Aus gneiss
CM19087	-26.539342	16.178165	Epidotised	Aus gneiss
CM19088	-26.532799	16.168355		Aus gneiss
CM19089	-26.515215	16.162034	massive floats of Tsirub gneiss, metasomatism	Aus gneiss
CM19090	-26.511411	16.153812	Heterogeneous package comprises of Biotite gneiss, marble, calc-silicate, amphibolite, marble unit at the top (thrust???)	Tsirub gneiss
CM19091	-26.518221	16.145879	Largely intruded by medium grained leucocratic quartzo feldspathic biotite gneiss	Tsirub gneiss
CM19092	-26.526644	16.149293	Largely intruded by medium grained leucocratic quartzo feldspathic biotite gneiss	Tsirub gneiss
CM19092	-26.526644	16.149293	Largely intruded by medium grained leucocratic quartzo feldspathic biotite gneiss	Tsirub gneiss
CM19093	-26.528832	16.153091	Contact between Tsirub and Aus gneiss	Contact
CM19094	-26.547028	16.173438	Strongly fractured and dominated by faulting, metasomatism	Aus gneiss
CM19095	-26.545596	16.16849	Biotite gneiss at parts	Tsirub gneiss

CM19096	-26.536681	16.163498	Aus gneiss at the top	Aus gneiss
CM19097	-26.541637	16.161061		Biotite gneiss/ Aus gneiss
CM19098	-26.642921	16.294096		Aus gneiss
CM19099	-26.644934	16.294025		Tsirub gneiss
CM19100	-26.550301	16.148136	Calc-silicate at the top	Biotite gneiss
CM19101	-26.546489	16.148245	Contact between biotite gneiss and marble	Contact
CM19102	-26.5438	16.15002		Marble
CM19103	-26.540036	16.150337	intruded by medium grained leucocratic quartzo feldspathic biotite gneiss	Tsirub gneiss
CM19104	-26.543873	16.144638	Largely intruded by Aus gneiss	Biotite gneiss
CM19105	-26.540733	16.142495	intruded by Aus gneiss	Marble/calc-silicate
CM19106	-26.539041	16.144906	intruded by Aus gneiss	Marble
CM19107	-26.538546	16.145863	Contact between biotite gneiss and Tsirub gneiss, biotite gneiss xenolith	Contact
CM19108	-26.539157	16.143003	Heterogeneous package comprises of amphibolite, calc-silicate, biotite gneiss intruded by medium grained leucocratic quartzo feldspathic biotite gneiss	Calc-silicate
CM19109	-26.542299	16.140447		Aus gneiss
CM19110	-26.545133	16.137911	Contact between Aus and Tsirub gneiss	Tsirub gneiss
CM19111	-26.693851	16.195538		Medium grained leucocratic quartzo feldspathic biotite gneiss
CM19112	-26.728102	16.150264	Largely intruded by pegmatite, pelites at parts	Amphibolite
CM19113	-26.7234	16.148357	Pelite scree	Medium grained leucocratic quartzo feldspathic biotite gneiss
CM19114	-26.721902	16.148847	Homogeneous equigranular re-crystallised unit, no pegmitite intrusion	Quartz-feldspar biotite gneiss
CM19115	-26.720788	16.149063	Pegmitite intrusion	Medium grained leucocratic quartzo feldspathic biotite gneiss
CM19116	-26.71818	16.14881	Contact between Medium grained leucocratic quartzo feldspathic biotite gneiss and aluminious rock and biotite gneiss at parts	Contact
CM19117	-26.715536	16.146373	Mixture of re-crystallised biotite gneiss and pelites, no pegmatite intrusion	Biotite gneiss/pelites
CM19118	-26.741083	16.157549		Biotite gneiss
CM19119	-26.734955	16.210564		Medium grained leucocratic quartzo feldspathic biotite gneiss
CM19120	-26.723766	16.206306		Medium grained leucocratic quartzo feldspathic biotite gneiss
CM19121	-26.711174	16.204243		Medium grained leucocratic quartzo feldspathic biotite gneiss
CM19122	-26.684574	16.20725		Medium grained leucocratic quartzo feldspathic biotite gneiss
CM19123	-26.65462	16.247898		Medium grained leucocratic quartzo feldspathic biotite gneiss/Aus gneiss
CM19124	-26.655681	16.246875	Contact between Aus gneiss and migmatitic rocks, shear zone???	Contact
CM19125	-26.654884	16.245035	Highly wherathered and fractured	Medium grained leucocratic quartzo feldspathic biotite gneiss

CM19126	-26.65323	16.241381	Highly fractured, iron staining, fault breccia cutting through	Medium grained leucocratic quartzo feldspathic biotite gneiss
CM19126	-26.65323	16.241381	Highly fractured, iron staining, fault breccia cutting through	Medium grained leucocratic quartzo feldspathic biotite gneiss
CM19127	-26.653672	16.240369		Meta-pelites
CM19128	-26.653042	16.23913	Contact between meta-pelites and recyrstallised biotite gneiss	Contact
CM19129	-26.655307	16.235521	Highly fractured	Medium grained leucocratic quartzo feldspathic biotite gneiss
CM19130	-26.662363	16.234864		Meta-pelites
CM19131	-26.639179	16.23381	Epidotised	Pink quartz feldspar rock
CM19131	-26.639179	16.23381	Epidotised	Pink quartz feldspar rock
CM19132	-26.637859	16.233905	Small outcrop, books of biotite	Pink quartz feldspar rock
CM19133	-26.632315	16.240032		Aus gneiss
CM19134	-26.629505	16.243274	Intruded by pegmitite, contact between Aus and pink quartz feldpar rock???	Aus gneiss
CM19135	-26.623468	16.245783	Epidotised, plag altered to k-spar (albitised)	Pink quartz feldspar rock
CM19135	-26.623468	16.245783	Epidotised, plag altered to k-spar (albitised)	Pink quartz feldspar rock
CM19136	-26.623506	16.248216	Contact between Aus gneiss and pink quartz feldpar rock	Contact
CM19137	-26.627398	16.246919		Pink quartz feldspar rock
CM19137	-26.627398	16.246919		Pink quartz feldspar rock
CM19138	-26.649958	16.256293		Aus gneiss
CM19139	-26.66932	16.255986	Recrystallised equigranular biotite gneiss cross-cutting the quartzo feldspathic gneiss	Medium grained leucocratic quartzo feldspathic biotite gneiss
CM19140	-26.670902	16.254534		Medium grained leucocratic quartzo feldspathic biotite gneiss
CM19141	-26.672894	16.253273		Amphibolite
CM19142	-26.674136	16.252507	within the quartzofelspathic gneiss	Amphibolite
CM19143	-26.679452	16.252254		Medium grained leucocratic quartzo feldspathic biotite gneiss

Appendix B: Structural measurements

Field ID	Latitude	Longitude	Structure Type	Azimuth	Dip
CM19001	-26.639953	16.318555			
CM19002	-26.639082	16.306487			
CM19003	-26.645013	16.293756	S2	272	65
CM19004	-26.558951	16.306541			
CM19005	-26.568117	16.300517	S2	212	50
CM19006	-26.622494	16.271918			
CM19007	-26.62918	16.266956			
CM19008	-26.596065	16.203222			
CM19009	-26.598199	16.202986	FP	274	72
CM19010	-26.591471	16.201359			

CM19011	-26.586336	16.202381			
CM19012	-26.575325	16.200269			
CM19013	-26.571642	16.198685	S2	160	30
CM19014	-26.571182	16.198396			
CM19015	-26.570132	16.194428	S2	160	30
CM19016	-26.5801	16.15913			
CM19017	-26.59907	16.16401			
CM19018	-26.598254	16.166461	S2	82	20
CM19019	-26.604525	16.16444			
CM19020	-26.605238	16.16422			
CM19021	-26.611313	16.169862	S2	80	15
CM19022	-26.619778	16.175207			
CM19023	-26.620402	16.173647	S2	350	25
CM19024	-26.625677	16.178774			
CM19025	-26.634121	16.173751			
CM19026	-26.566174	16.179668	S2	168	38
CM19027	-26.608841	16.222732	S2	22	54
CM19027	-26.608841	16.222732	FP	4	62
CM19028	-26.612882	16.223347	S2	18	45
CM19029	-26.612833	16.228032			
CM19030	-26.613771	16.22817	S2	18	48
CM19031	-26.613316	16.225562			
CM19032	-26.620311	16.225656	S2	12	36
CM19033	-26.625077	16.220377			
CM19034	-26.631094	16.224292	S2	50	35
CM19035	-26.568243	16.1776	S2	160	34
CM19036	-26.567648	16.180242	FP	274	72
CM19037	-26.570508	16.18374			
CM19038	-26.571619	16.183887			
CM19039	-26.573948	16.183902	S2	150	64
CM19040	-26.574101	16.18483	S2	168	38
CM19041	-26.574611	16.185406	S2	158	48
CM19042	-26.579209	16.185886	S2	130	24
CM19043	-26.585643	16.184747	S2	142	32
CM19044	-26.585901	16.195171	S2	98	24
CM19045	-26.584866	16.197969	S2	102	50
CM19046	-26.610002	16.200927	S2	18	38
CM19047	-26.615458	16.203127	S2	14	32
CM19048	-26.616708	16.196978	S2	17	28
CM19049	-26.627401	16.209855	S2	18	30
CM19050	-26.997464	16.196223	S2	34	60
CM19051	-27.003811	16.196498	S2	38	42
CM19052	-27.000285	16.189024	S2	35	42

CM19053	-26.999687	16.189755	S2	96	40
CM19053	-26.999687	16.189755	FP	42	320
CM19054	-26.993837	16.192491	S2	48	52
CM19055	-26.990673	16.183225	S2	8	60
CM19056	-27.021356	16.206698	S2	29	68
CM19057	-27.018715	16.204012	S2	22	62
CM19058	-26.979176	16.132024	S2	72	56
CM19059	-26.589189	16.236703			
CM19060	-26.59162	16.234982			
CM19061	-26.587654	16.240763	FP	274	72
CM19062	-26.581877	16.242546			
CM19063	-26.572337	16.200269			
CM19064	-26.573479	16.200869			
CM19065	-26.585561	16.204724			
CM19066	-26.600236	16.215856	S2	54	40
CM19067	-26.602765	16.229478			
CM19068	-26.603046	16.237594			
CM19069	-26.609679	16.24801			
CM19070	-26.572193	16.193925	S2	136	30
CM19071	-26.574907	16.193175	S2	106	30
CM19072	-26.576042	16.192156	S2	150	34
CM19073	-26.578112	16.192287	S2	132	30
CM19074	-26.577525	16.191255			
CM19075	-26.574249	16.191475			
CM19076	-26.571494	16.19229	FP	274	72
CM19077	-26.713758	16.277316			
CM19078	-26.705082	16.258476			
CM19079	-26.56609	16.195271	S2	169	25
CM19079	-26.56609	16.195271	FP	248	60
CM19080	-26.566667	16.183333	S2	156	38
CM19081	-26.563151	16.19436	S2	138	32
CM19082	-26.566583	16.190892	S2	164	35
CM19083	-26.564933	16.175739			
CM19084	-26.555155	16.175474			
CM19085	-26.559497	16.193949	S2	135	25
CM19086	-26.548564	16.1795	FP	288	55
CM19087	-26.539342	16.178165			
CM19088	-26.532799	16.168355	FP	136	72
CM19089	-26.515215	16.162034	FP	102	50
CM19090	-26.511411	16.153812	S2	15	58
CM19091	-26.518221	16.145879	S2	18	30
CM19092	-26.526644	16.149293	S2	18	40
CM19092	-26.526644	16.149293	FP	288	65

CM19093	-26.528832	16.153091	FP	255	72
CM19094	-26.547028	16.173438	FP	204	78
CM19095	-26.545596	16.16849	S2	26	18
CM19096	-26.536681	16.163498			
CM19097	-26.541637	16.161061	S2	8	30
CM19098	-26.642921	16.294096			
CM19099	-26.644934	16.294025			
CM19100	-26.550301	16.148136	S2	78	20
CM19101	-26.546489	16.148245	S2	46	15
CM19102	-26.5438	16.15002			
CM19103	-26.540036	16.150337	S2	50	30
CM19104	-26.543873	16.144638	S2	80	15
CM19105	-26.540733	16.142495	S2	26	20
CM19106	-26.539041	16.144906	S2	62	20
CM19107	-26.538546	16.145863	S2	50	20
CM19108	-26.539157	16.143003	S2	28	28
CM19109	-26.542299	16.140447	S2	32	15
CM19110	-26.545133	16.137911	S2	28	28

Appendix C: Thin sections

Waypoint number/Sample ID	**Latitude**	**Longitude**	**Lithology**	**Comment**
CM19014	-26.571	16.1984	Metapelites	
CM19017	-26.599	16.164	Kubub gneiss	
CM19034	-26.631	16.2243	Calc-silicates	
CM19036	-26.568	16.1802	Aus gneiss	Polished block
CM19064	-26.573	16.2009	Pink quartz feldspar rock	Polished block
CM19069	-26.61	16.248	Amphibolite	
CM19074	-26.578	16.1913	Tsirub gneiss	Polished block
CM19098	-26.643	16.2941	Aus gneiss	
CM19099	-26.645	16.294	Tsirub gneiss	
CM19100	-26.55	16.1481	Garnet biotite quartz	
CM19101	-26.546	16.1482	Marble	
CM19104	-26.544	16.1446	Garnet biotite quartz	

Appendix D: List of samples for geochemistry

Waypoint number/Sample ID	Latitude	Longitude	Lithology
CM19036	-26.568	16.1802	Aus gneiss-Fault zone, fault breccia
CM19064	-26.573	16.2009	metasomatism, Hydrothermal alteration
CM19074	-26.578	16.1913	Tsirub gneiss, plag altered to k-spar (albitisation)
CM19098	-26.643	16.2941	Megacrstic coarse grained Aus gneiss
CM19099	-26.645	16.294	Augen Tsirub gneiss
CM19015	-26.6348	16.2864	Garnet-bearing augen leucogranite gneiss
CM19103	-26.6543	16.2480	Tsirub streaky granod. augen gneiss
CM19131	-26.7000	16.3519	Tsirub streaky granod. augen gneiss
CM19174	-26.7951	15.9973	Feldspar porphyroclastic gt-bearing granodiorite gneiss (Tsirub gneiss)
CM19011	-27.0928	16.3562	Feldspar porphyroclastic granodiorite gneiss (Tsirub gneiss)
CM19004	-26.6273	16.2975	Hornblend mcrysic granodiorite gneiss (Tsirub gneiss)
CM19004	-26.6273	16.2975	Hornblend mcrysic granodiorite gneiss (Tsirub gneiss)
CM19117	-26.8267	16.2447	Feldspar porphyroclastic gt-bearing granodiorite gneiss (Tsirub gneiss)
CM19069	-27.0940	16.2951	Megacrystic equigranular bt granite
CM19126	-26.7584	16.3401	Megacrystic equigranular bt granite
CM19126	-26.7584	16.3401	Megacrystic equigranular bt granite
CM19212	-26.7428	16.1326	Garnet-biotite leucogneiss (type 1 - diatexite augen gn-Kubub gneiss)
CM19105	-26.6508	16.2271	Garnet-biotite leucogneiss (dehydration melt - type 2 -Kubub gneiss)

Appendix E: Geochronology samples

Waypoint number/Sample ID	Latitude	Longitude	Lithology
CM19098	-26.643	16.2941	Aus gneiss
CM19099	-26.645	16.294	Tsirub gneiss

Appendix F: Geochemical results (Major elements in wt%)

Sample ID	SiO2 (%)	TiO2 (%)	Al2O3 (%)	FeO (%)	Fe2O3 (%)	MnO (%)	MgO (%)	CaO (%)	Na2O (%)	K2O (%)	P2O5 (%)	Cr2O3 (%)	LOI (%)	Total (%)
CM19036	76.180	0.240	11.370	1.957	0.325	0.040	0.270	3.150	0.150	5.320	0.050	bdl	0.907	99.959
CM19064	76.410	0.180	11.580	1.339	0.222	bdl	bdl	0.110	0.230	9.370	0.050	bdl	0.341	99.832
CM19074	62.640	0.760	16.840	3.844	0.638	0.080	1.340	4.400	2.680	4.660	0.170	bdl	1.588	99.640
CM19098	71.730	0.270	14.580	1.628	0.270	0.020	0.350	1.280	3.050	5.970	0.130	bdl	0.786	100.065
CM19099	67.860	0.880	14.670	4.267	0.709	0.070	1.470	2.760	2.570	3.750	0.180	bdl	0.596	99.781
EM19015	75.383	0.106	13.597	1.224	0.203	0.070	0.218	0.966	3.187	4.951	0.056	0.009	0.210	100.181
PM19030B	67.073	0.971	14.992	4.301	0.714	0.060	1.246	2.273	2.464	4.969	0.446	0.010	0.330	99.850
PM19088	61.232	0.912	15.996	5.995	0.996	0.134	3.284	4.393	2.976	2.601	0.185	0.015	0.860	99.580
PM19103	68.535	0.783	14.217	4.237	0.703	0.096	0.762	2.215	2.684	5.292	0.237	0.004	0.150	99.915
PM19131	70.379	0.610	13.766	3.236	0.537	0.066	0.834	2.012	2.552	5.328	0.131	0.004	0.400	99.856
PM19174	68.566	0.817	15.176	3.605	0.599	0.065	1.050	2.163	2.478	4.950	0.288	0.012	0.250	100.018
PM19011	65.111	0.724	16.358	3.158	0.524	0.064	2.150	3.765	3.987	3.367	0.236	0.013	0.520	99.976
EM19004	66.214	1.129	14.634	5.157	0.856	0.104	2.026	3.367	2.014	3.534	0.237	0.010	0.530	99.813
EM19004B	65.379	1.138	14.435	5.297	0.879	0.109	2.084	3.498	2.112	3.686	0.240	0.011	0.510	99.377
PM19117	66.509	1.047	15.360	4.514	0.749	0.088	1.359	2.190	2.649	4.644	0.260	0.005	0.520	99.895
CG19037	70.970	0.255	14.726	1.931	0.321	0.024	0.639	1.248	2.477	6.624	0.137	0.004	0.773	100.128
PM19109	69.909	0.545	15.397	1.884	0.313	0.016	0.636	1.577	2.859	5.947	0.155	0.003	1.030	100.271
PM19211	67.934	0.474	15.567	2.656	0.441	0.026	0.856	1.912	2.472	6.329	0.200	0.005	1.120	99.992
PM19190	68.223	0.599	15.169	2.718	0.451	0.032	0.865	1.855	2.457	6.297	0.211	0.005	1.210	100.092
PM19069	70.543	0.264	15.109	1.891	0.314	0.040	0.652	1.511	2.669	6.566	0.151	0.003	0.330	100.043
PM19126	72.676	0.258	14.334	1.782	0.296	0.027	0.398	1.254	2.867	5.948	0.130	0.003	0.380	100.353
PM19126B	72.589	0.257	14.352	1.805	0.300	0.026	0.405	1.264	2.865	5.957	0.132	0.002	0.370	100.324
PM19212	72.719	0.307	14.573	1.759	0.292	0.033	0.587	1.761	3.069	4.265	0.081	0.004	0.590	100.041
PM19105	73.859	0.117	14.665	1.351	0.224	0.050	0.312	0.854	3.171	5.195	0.143	0.004	0.180	100.125

Trace Elements Results (in ppm)

Sample ID	CM19036	CM19064	CM19074	CM19098	CM19099	EM19015	PM19088	PM19103	PM19131	PM19174	PM19011	EM19004	PM19117	CG19037	PM19109	PM19211	PM19190	PM19069	PM19126	PM19212	PM19105
Li	27.2	29.1	45.03	32.2	52.5	27.14	42.12	13.65	51.07	22.58	34.33	44.03	35.09	27.71	22.22	15.48	27.05	11.02	23.12	13.97	16.36
Sc	4.61	3.76	11.11	4.93	11.96	5.199		9.682	5.558		7.776		9.227	2.448			3.014	0.997	2.09	2.706	3.571
V	16.56	24.6	59.7	20.34	70.9	3.527	100.4	37.24	32.41	49.59	70.09	89.93	67.13	22.62	27.98	40	42.5	27.06	12.24	21.1	4.589
Cr	15.2	10.6	82.5	11.5	44.5	6.365	93.75	8.782	18.17	23.08	45.18	57.68	24.73	6.995	6.767	8.582	11.65	9.298	7.059	12.69	7.968
Co	1.39	0.29	7.98	2.74	10.4	0.783	17.6	6.716	5.733	8.892	10.64	15.11	10.61	2.879	3.108	5.035	7.18	3.429	2.186	3.122	1.114
Ni	5.1	5.9	17.8	4.44	19.4	2.327	36.98	4.46	10.23	14.26	32.19	26.74	9.704	4.531	2.566	4.965	4.979	4.83	2.702	5.636	2.891
Cu	22.4	12.09	18.67	14.78	44	1.586	25.98	15.67	7.906	53.07	15.18	63.62	42.86	86.43	6.947	50.69	35.31	23.15	2.439	3.585	4.813
Zn	48.8	3.5	90.1	45.9	72.9	55.44	113.7	94.85	65.96	86.94	64.33	99.61	127.4	57.75	81.42	70.97	91.48	119.5	67.94	78.8	61.81
Ga	28.22	29.49	40.69	27.58	45.21	26.22	36.83	43.24	39.47	44.21	52.17	42.69	49.75	46.11	46.98	54.13	53.92	57.29	30.19	29.49	21.52
Rb	223.3	297.3	238.6	353.4	288.1	336.2	161.3	264.7	344.4	232.1	145.7	233.2	243.7	235.2	302.7	235.2	274.7	181.2	306.4	190.2	267.7
Sr	103.2	58	147	90.8	123.2	42.13	214.3	82.37	74.72	178.5	511.7	133.7	175.5	191.5	205.4	225.6	170.6	223.3	72.55	100.8	36.57
Y	8.4	11.51	29.14	24.73	48.73	37.14	43.23	45.69	58.08	24.03	24.44	45.17	27.04	13.16	4.072	13.67	10.65	13.06	24.49	13.45	15.52
Zr	209.6	203.9	442.8	184.4	399.9	97.01	149.8	239.1	222.7	135	187.7	181.6	145.4	191.1	221.6	174.2	154.6	231.4	188.4	157.5	47.92
Nb	12.45	11.01	22.65	16.55	17.92	9.053	10.75	23.93	19.13	17.86	10.29	20.37	21.32	7.763	10.37	8.497	13.03	4.393	23.29	10.42	9.039
Ba	226	703	688.4	378.4	792.7	175.1	580.5	815.4	574.5	897.1	1074	865.8	936.4	1022	868.1	1298	1103	1255	361.2	351.1	106.1
La	120.3	19.93	88.9	97.6	92.04	38.21	27.36	70.81	142.1	43.26	47.19	54.22	81.63	129.7	158.6	215.9	211.7	124.1	99.12	46.34	15.36
Ce	250.4	36.3	179.3	195.2	187.1	81.17	65.66	149.9	276.3	96.38	98.85	113.5	184.2	264.7	326.5	438.4	457.9	241.6	213.4	100.7	32.76
Pr	28.29	4.2	19.55	21.16	21.07	8.709	8.534	17.46	28.16	11.3	11.85	13.27	21.94	26.98	34.17	48.98	47.82	23.07	23.58	11.46	3.676
Nd	99.7	16.2	72.2	71.7	79.1	30.59	35.7	67.52	98.84	43.58	44.08	50.33	83.97	91.2	116.6	156.9	163.9	74.66	82.99	41.72	13.57
Sm	17.98	3.05	12.69	11.05	14.81	6.317	8.16	13.74	16.74	8.03	7.647	9.886	14.06	13.77	15.16	20.77	19.92	9.864	15.3	8.335	3.232
Eu	0.881	0.481	1.674	0.934	1.702	0.52	1.847	1.56	1.533	1.781	1.731	1.992	1.98	1.571	1.639	2.128	1.949	1.216	0.934	1.11	0.308
Tb	0.838	0.378	1.206	0.889	1.626	0.941	1.254	1.87	2.023	0.861	0.858	1.564	1.211	0.88	0.476	0.998	0.946	0.679	1.361	0.719	0.521
Gd	9.85	2.8	9.62	7.32	11.95	5.755	8.103	12.33	13.92	6.341	6.246	11.17	9.856	8.62	6.085	10.61	9.793	5.763	10.74	6.161	3.183
Dy	3.01	2.21	6.56	5.32	9.65	6.225	8.079	10.7	11.37	4.544	4.853	9.169	6.149	3.686	1.36	3.774	3.276	2.926	6.271	3.236	3.066
Ho	0.377	0.413	1.116	0.853	1.801	1.324	1.604	1.84	2.112	0.782	0.888	1.705	1.039	0.534	0.162	0.554	0.451	0.509	0.939	0.514	0.531
Er	0.719	1.31	2.86	2.03	5	4.305	4.779	4.807	6.404	2.056	2.601	4.796	2.783	1.227	0.352	1.256	0.987	1.496	2.322	1.452	1.55
Tm	0.062	0.184	0.336	0.225	0.691	0.645	0.68	0.576	0.903	0.268	0.359	0.652	0.362	0.153	0.034	0.15	0.102	0.202	0.276	0.213	0.217
Yb	0.316	1.2	1.9	1.19	4.39	4.4	4.508	3.4	5.982	1.642	2.435	4.122	2.189	0.991	0.224	0.925	0.597	1.362	1.687	1.477	1.455
Lu	0.06	0.197	0.244	0.161	0.65	0.65	0.699	0.464	0.873	0.236	0.361	0.611	0.309	0.162	0.026	0.141	0.084	0.207	0.258	0.222	0.209
Hf	7.05	6.55	12.68	6.25	12.02	3.707	4.19	6.962	7.544	3.916	4.791	5.58	4.135	5.178	6.266	4.249	3.802	6.012	6.361	4.901	1.774
Ta	0.307	0.336	1.984	0.54	1.219	0.396	0.707	1.321	1.501	1.087	0.931	1.273	1.237	0.231	0.403	0.304	0.386	0.387	0.671	0.305	0.56
Pb	63.2	30.5	30.59	47.9	28.86	54.93	13.45	25.14	41.73	37.34	20.5	29.8	35.17	46.34	56.7	47.25	50.41	32.91	53.32	40.7	32.27
Th	125.5	72.5	43.55	93.7	40.04	41.91	6.499	24.98	89.26	15.77	10.79	15.93	35.11	64.76	83.17	83.16	117.9	47.93	94.23	27.46	8.992
U	13.79	4.26	11.16	12.23	4.12	39.16	1.173	3.036	6.472	1.806	2.76	2.037	6.457	0.806	2.244	0.736	0.726	1.205	15.02	2.82	3.307

Appendix G: Geochronology results

Sample CM19098

Sample ID	U	206Pb	206Pbc(%)	206/204	207Pb/206Pb*	1SE	207Pb/235U*	1SE	206Pb/238U*	1SE	Rho	Central (%)	Minimum rim (%)	207/206
CM19098-10c2	84	8.8	0	651	0.099	0.001	1.539	0.039	0.113	0.002	0.842	-59.900	-57.700	1601
CM19098-2a	411	50.8	0	5209	0.075	0.001	1.305	0.028	0.125	0.002	0.925	-31.200	-28.100	1081
CM19098-3c	153	25.8	0	9044	0.076	0.001	1.808	0.027	0.173	0.002	0.851	-5.300	-1.500	1084
CM19098-4a1	916	120.3	0	1749	0.080	0.001	1.483	0.023	0.135	0.002	0.857	-33.700	-31.100	1192
CM19098-4a2	725	103	0	2085	0.079	0.001	1.571	0.028	0.145	0.002	0.911	-27.200	-24.500	1167

Sample CM19099

Sample ID	U	206Pb	206Pbc(%)	206/204	207Pb/206Pb*	1SE	207Pb/235U*	1SE	206Pb/238U*	1SE	Rho	Central (%)	Minimum rim (%)	207/206
CM19099-11a	197	26	0	12217	0.077	0.001	1.991	0.040	0.188	0.003	0.913	-0.7	.	1118
CM19099-12b	348	40	0	3568	0.077	0.001	1.751	0.035	0.165	0.003	0.923	-12.9	-9.3	1119
CM19099-12c	79	10.3	0	21667	0.076	0.001	1.954	0.036	0.187	0.003	0.903	1	.	1093
CM19099-1a2	98	16.1	0	4142	0.075	0.000	1.821	0.032	0.175	0.003	0.950	-3.9	-0.9	1079
CM19099-1a3	88	14.8	0	2155	0.082	0.001	2.006	0.039	0.179	0.003	0.946	-15.3	-12.6	1233
CM19099-1b1	960	157	0	3500	0.077	0.000	1.799	0.039	0.169	0.004	0.977	-11.1	-8.8	1123
CM19099-1b2	698	126.4	0	6140	0.078	0.000	2.017	0.042	0.188	0.004	0.974	-3.2	-0.7	1143
CM19099-1b3	1059	184.2	0	5997	0.077	0.000	1.907	0.045	0.179	0.004	0.979	-6.4	-4	1128
CM19099-2a1	125	16.4	0	5081	0.079	0.001	1.956	0.038	0.180	0.003	0.920	-8.7	-5	1163
CM19099-2b1	238	34.1	0	5160	0.078	0.001	2.080	0.048	0.194	0.004	0.946	-0.4	.	1145
CM19099-2b2	307	44.8	0	22910	0.076	0.001	2.074	0.044	0.198	0.004	0.938	6.3	1.1	1099
CM19099-3c	169	23.9	0	9218	0.076	0.001	2.052	0.038	0.197	0.003	0.920	6.9	2.2	1088
CM19099-5b	230	32.8	0	14629	0.077	0.001	2.091	0.039	0.198	0.003	0.920	4.6	.	1115
CM19099-6a1	124	17.8	0	11055	0.076	0.001	2.073	0.040	0.199	0.003	0.919	8.2	3.2	1087
CM19099-6a2	139	20.1	0	9357	0.076	0.001	2.076	0.043	0.199	0.004	0.931	8.8	3.5	1084
CM19099-6a3	123	20.8	0	10217	0.075	0.001	2.381	0.053	0.231	0.005	0.942	29.1	22.5	1061
CM19099-7a1	129	17.1	0	3788	0.079	0.001	2.048	0.039	0.187	0.003	0.917	-7.3	-3.6	1184
CM19099-7a2	98	13.7	0	10592	0.076	0.001	2.053	0.038	0.196	0.003	0.911	5.7	1	1096
CM19099-7b	643	74.6	0	2164	0.076	0.001	1.721	0.062	0.164	0.006	0.967	-11.5	-6.9	1097